Ohmic Contacts to Implanted (0001) 4H-SiC

by

Mingyu Li

A dissertation submitted to the Graduate Faculty of
Auburn University
in partial fulfillment of the
requirements for the Degree of
Doctor of Philosophy

Auburn, Alabama
December 18, 2009

Keywords: 4H-SiC, ion implantation, specific contact resistance,
sheet resistance, Hall effect, Hall concentration, Hall mobility

Copyright 2009 by Mingyu Li

Approved by

John R. Williams, Chair, Walter Professor of Physics
Yu Lin, Professor of Physics
Minseo Park, Associate Professor of Physics
Jianjun Dong, Associate Professor of Physics

Abstract

The fabrication of low resistance ohmic contacts is a key technology issue for the development of SiC power diodes and transistors. In many cases, contacts are made to implanted regions due to the difficulty of doping SiC by diffusion.

In this work, linear transmission line measurements (LTLM) were performed to investigate the relationships between specific contact resistance (r_c) and implanted doping concentration (N_D) for both N- and Al-implanted samples. Carbon caps were used for all samples during the post-implant thermal activation annealing process. The N- and Al-implanted samples were activated at 1550°C/30min/Ar and 1650°C/30min/Ar, respectively. The alloy NiV7% was used for contacts to N-implanted samples with a contact anneal at 1100°C for 1 min at 10^{-7} Torr. The alloy Al70%Ti30% was used for Al-implanted samples with a contact anneal at 1000°C for 1 min at 10^{-7} Torr. The specific contact resistance for a fixed implant concentration was also studied as a function of activation annealing temperature. A second goal of this work has been to determine the activation percentage as a function of the implant concentration for the various activation annealing temperatures. Hall samples were prepared for these measurements.

Results for the implanted samples have been compared to the data reported previously for 4H epitaxial layers. Generally, the data show that the specific contact resistances are higher than predicted theoretically at high implant concentrations. This

result is consistent with a lower activation percentage due to implant damage, which was demonstrated using Hall measurements. Furthermore, data from activation anneals at different temperatures shows that the specific contact resistance for Al-implanted samples is more sensitive to the activation anneal temperature compared to the contact resistance for N-implanted samples.

Acknowledgements

The author would like to express his deepest gratitude to his supervisor, Prof. John R. Williams, for his excellent guidance, continuous support and stimulating suggestions. Without his patience, wisdom and persistence, it would be impossible to achieve the goals of this study.

The author is in debt to Research Assistant Professor Ayayi C. Ahyi for his contributions and valuable discussions during the course of this work. The author would like to thank Mrs. Tamara Isaac-Smith for her patiently writing correction of this dissertation, the initiation and successful completion of this work. The author also would like to thank Mr. Max Cichon for his contribution in building and maintaining the essential equipment needed for the success of this work.

The author is grateful to all the committee members, Dr. Jianjun Dong, Dr. Yu Lin, Dr. Minseo Park and Dr. Wayne Johnson for their support, instruction and evaluation of this work.

Finally, the author would like to express his extremely appreciation to his wife, Xuemei Chen, and his daughter, Christina Li, for their support, patience and encouragement during these years of study.

Table of Contents

Abstract……………………………………………………………………………ii

Acknowledgements…………………………………………………………....iv

List of Tables…………………………………………………………….…ix

List of Figures……………………………………………………………………xii

Chapter 1 Introduction……………………………………………………..1

1.1 Purpose of This Thesis………………………………………………. 1

1.2 Properties of SiC……………………………………………………...3

1.2.1 Polytypism in SiC………………………………………...…...3

1.2.2 Semiconducting Properties of SiC………………………………….6

1.2.3 SiC Substrate Crystal Growth……………………………………….8

1.2.4 Ohmic Contacts to SiC…………………………………………...9

1.2.5 Device and Application……………………………………………10

1.3 Scope of the Thesis……………………………………………….…14

Chapter 2 Metal-semiconductor Contact…………………………………..16

2.1 Schottky Contact……………………………………………………….16

2.2 Ohmic Contact……………………………………………………………22

2.3 Ohmic Contacts to SiC…………………………………………………25

2.3.1 N-type α–SiC……………………………………………...…26

2.3.2 P-type α-SiC……………………………………………...…….27

2.3.3 N-type β–SiC……………………………………………………..………………30

2.3.4 P-type β-SiC…………………………………………………………………………33

Chapter 3 Methodologies……………………………………………………….………34

3.1 Atomic Force Microscope (AFM)……………………………………………...…34

3.2 Collinear Four-point Probe Measurement……………………………….……35

3.3 Van der Pauw Measurement and Hall Effect…. ………………………………37

3.3.1 Sample Preparation…………………………………………………………38

3.3.2 Resistivity Measurements…………………………………………………...39

3.3.3 Hall Measurements…………………………………………………………42

3.3.3.1 Introduction to Hall Effect……………………………………42

3.3.3.2 Calculations………………………………………………...45

3.4 Linear Transmission Line Model ……………..…………………………….....47

3.4.1 The Specific Contact Resistance……………………………………………47

3.4.2 The Linear Transmission Line Model………………………………………48

Chapter 4 Experimental Methods……………………………………………….54

4.1 Standard Procedures for Device Fabrication……………………………………54

4.1.1 The Standard Sample Cleaning Process……………………………………54

4.1.2 Sample Oxidation…………………………………………………………...56

4.1.3 Sample Implantation………………………………………………………..57

4.1.4 Optical Photolithography……………………………………………...61

4.1.5 Metal Sputter Deposition…………………………………...…………64

4.1.6 Sample Activation and Contact Anneal……………………………......67

4.1.7 Reactive Ion Etching (RIE)……………………………………………...…69

4.1.8 Sample Wire Bonding……………………………………………………71

4.2 Device Fabrication and Measurements………………………………………..72

4.2.1 Hall Sample………………………………………………………………72

4.2.2 Ohmic Contact Fabrication for LTLM………………………………...73

4.2.3 TLM Measurement……………………………………………………73

4.2.4 Hall Effect Measurement………………………………………………79

Chapter 5 Results and Discussion………………………………………………81

5.1 AFM Measurements…………………………………………………………...81

5.2 Optimization of Contact Anneal………………………………………………88

5.2.1 NiV7% Contact Annealed at 1000°C…………………………………88

5.2.2 Ni80Cr20 Contact Annealed at 1000°C………………………………91

5.3 Ohmic Contacts to N-implanted Samples……………………………………..94

5.3.1 NiV7% Contact Annealed at 1000°C/2min/vacuum…………………...94

5.3.2 NiV7% Contact Annealed at 1100°C/1min/vacuum…………………...96

5.4 Ohmic Contacts to Al-implanted Samples…………………………………...106

5.5 Effect of Activation Temperatures…………………………………………...114

5.5.1 TLM Results for N Implant Concentration 5×10^{18}cm^{-3}………………115

5.5.2 TLM Results for N Implant Concentration 1×10^{20}cm^{-3}………………120

5.5.3 TLM Results for Al Implant Concentration 5×10^{18}cm^{-3}…………….124

5.5.4 TLM Results for Al Implant Concentration 1×10^{20}cm^{-3}……………..129

5.6 Hall Measurements…………………………………………………………..133

Chapter 6 Summary, Conclusions and Suggestions for Future Work………………....138

References……………………………………………………………………………139

Appendix……………………………………………………………………………..152

List of Tables

1.1 Comparison of important semiconductor properties for high-temperature electronics………………………………………………………………… 7

2.1 Work function of selected metals and their measured and calculated barrier height on n-type 4H-SiC [49]……………………………………………... 19

2.2 Some ohmic contacts on n-type α-SiC. The layers in multi-layered contacts are separated with slashes; layers at the surface to the interface with SiC proceed from right to left. [58]…………………………………………….. 28

2.3 Some ohmic contacts on p-type α-SiC. The layers in multi-layered contacts are separated with slashes; layers at the surface to the interface with SiC proceed from right to left [58]……………………………………………... 31

2.4 Some ohmic contacts on n-type β-SiC. The layers in multi-layered contacts are separated with slashes; layers at the surface to the interface with SiC proceed from right to left [58]……………………………………………... 32

2.5 Some ohmic contacts on p-type β-SiC. The layers in multi-layered contacts are separated with slashes, layers at the surface to the interface with SiC proceed from right to left [58]……………………………………………... 33

4.1 The implanted profile and purpose of 4H-SiC samples……………………….. 61

5.1 Resistance between two NiV7% contacts (200um×200um) separated by 76 um 89

5.2 Summery of TLM and Vander der Pauw results for NiV7% contacts annealed at 1000 ^{o}C /2+1+1+1min/vacuum. "no" means data is unavailable… 91

5.3 TLM results for N implant concentration 1×10^{18} cm^{-3} with Ni80Cr20 contacts annealed at 1000 ^{o}C in vacuum. "no" means data is unavailable....… 92

5.4 Summary of specific contact resistance and sheet resistance measurement for N-implanted (0001) 4H-SiC annealed at 1000°C/2min/vacuum for NiV7% contacts. "no" means data is unavailable……………………………………... 96

5.5 Summary of specific contact resistance and sheet resistance measurement for

N-implanted (0001) 4H-SiC with implant concentration 1×10^{18} cm^{-3}……….. 98

5.6 Summary of specific contact resistance and sheet resistance measurement for N-implanted (0001) 4H-SiC with implant concentration 4×10^{18} cm^{-3}……….. 99

5.7 Summary of specific contact resistance and sheet resistance measurement for N-implanted (0001) 4H-SiC with implant concentration 1×10^{19} cm^{-3}……….. 100

5.8 Summary of specific contact resistance and sheet resistance measurement for N-implanted (0001) 4H-SiC with implant concentration 4×10^{19} cm^{-3}……….. 101

5.9 Summary of specific contact resistance and sheet resistance measurement for N-implanted (0001) 4H-SiC with implant concentration 1×10^{20} cm^{-3}……….. 103

5.10 Summary of specific contact resistance and sheet resistance measurement for N-implanted (0001) 4H-SiC………………………………………………. 105

5.11 Summary of specific contact resistance and sheet resistance measurement for Al-implanted (0001) 4H-SiC with implant concentration 2×10^{18} cm^{-3}…... 108

5.12 Summary of specific contact resistance and sheet resistance measurement for Al-implanted (0001) 4H-SiC with implant concentration $8\times10^{18}cm^{-3}$…... 109

5.13 Summary of specific contact resistance and sheet resistance measurement for Al-implanted (0001) 4H-SiC with implant concentration 2×10^{19} cm^{-3}…... 110

5.14 Summary of specific contact resistance and sheet resistance measurement for Al-implanted (0001) 4H-SiC with implant concentration $8\times10^{19}cm^{-3}$…... 111

5.15 Summary of specific contact resistance and sheet resistance measurement for Al-implanted (0001) 4H-SiC with implant concentration 2×10^{20} cm^{-3}…... 112

5.16 Summary of specific contact resistance and sheet resistance measurement for Al-implanted (0001) 4H-SiC……………………………………………... 113

5.17 Summary of specific contact resistance and sheet resistance measurement for N implant concentration 5×10^{18} cm^{-3} activated at 1350 ^{o}C/30min/Ar…… 116

5.18 Summary of specific contact resistance and sheet resistance measurement for N implant concentration 5×10^{18} cm^{-3} activated at 1450 ^{o}C/30min/Ar……. 117

5.19 Summary of specific contact resistance and sheet resistance measurement for N implant concentration 5×10^{18} cm^{-3} activated at 1550 ^{o}C/30min/Ar ..…. 118

5.20 Summary of specific contact resistance and sheet resistance measurement

for N implant concentration 5×10^{18} cm^{-3} activated at 1650 ^oC/30min/Ar…… 119

5.21 Summary of specific contact resistance and sheet resistance measurement for N implant concentration 1×10^{20} cm^{-3} activated at 1350 ^oC/30min/Ar……….. 121

5.22 Summary of specific contact resistance and sheet resistance measurement for N implant concentration 1×10^{20} cm^{-3} activated at 1450 ^oC/30min/Ar……….. 122

5.23 Summary of specific contact resistance and sheet resistance measurement for N implant concentration 1×10^{20} cm^{-3} activated at 1550 ^oC/30min/Ar……….. 123

5.24 Summary of specific contact resistance and sheet resistance measurement for N implant concentration 1×10^{20} cm^{-3} activated at 1650 ^oC/30min/Ar……….. 124

5.25 Summary of specific contact resistance and sheet resistance measurement for Al implant concentration 5×10^{18} cm^{-3} activated at 1400 ^oC/30min/Ar……….. 125

5.26 Summary of specific contact resistance and sheet resistance measurement for Al implant concentration 5×10^{18} cm^{-3} activated at 1500 ^oC/30min/Ar………. 126

5.27 Summary of specific contact resistance and sheet resistance measurement for Al implant concentration 5×10^{18} cm^{-3} activated at 1600 ^oC/30min/Ar………. 127

5.28 Summary of specific contact resistance and sheet resistance measurement for Al implant concentration 5×10^{18} cm^{-3} activated at 1700 ^oC/30min/Ar………. 128

5.29 Summary of specific contact resistance and sheet resistance measurement for Al implant concentration 1×10^{20} cm^{-3} activated at 1400 ^oC/30min/Ar………. 130

5.30 Summary of specific contact resistance and sheet resistance measurement for Al implant concentration 1×10^{20} cm^{-3} activated at 1500 ^oC/30min/Ar………. 131

5.31 Summary of specific contact resistance and sheet resistance measurement for Al implant concentration 1×10^{20} cm^{-3} activated at 1600 ^oC/30min/Ar………. 132

5.32 Summary of specific contact resistance and sheet resistance measurement for Al implant concentration 1×10^{20} cm^{-3} activated at 1700 ^oC/30min/Ar………. 133

List of Figures

1.1 The tetragonal bonding of a carbon atom with the four nearest silicon neighbors. The distance a and C-SiC are approximately 3.08Å and 1.89Å respectively [17].. 4

1.2 The stacking sequence of double layers of the four most common SiC polytypes [17].. 5

1.3 The Miller indices describing the hexagonal structure. The c-axis refers to the last index, whereas the first three describes the directions of the basal plane [17].. 6

1.4 The basic structure of a MOSFETs.. 10

1.5 The basic structure of Light-emitting Diode.. 12

1.6 npn SiC Bipolar Transistor.. 13

1.7 SiC photodiode device cross section.. 14

2.1 (a) Energy band diagram of a metal adjacent to an n-type semiconductor under thermal equilibrium condition [49]. (b) metal-semiconductor contact in thermal equilibrium[49].. 17

2.2 Energy band diagram of the selected metals and 4H-SiC [50]............................ 18

2.3 Energy band diagram depicting field emission, thermionic field emission, and thermionic emission for an n-type semiconductor [30]........................ 23

3.1 (a) AFM cantilever in the Scanning Electron Microscope; (b) Block Diagram of Atomic Force Microscope [82].. 34

3.2 Four-point measurement of semiconductor sheet resistance [84].................. 37

3.3 Some Van der Pauw sample patterns [86].. 39

3.4 Schematic diagram of measuring $R_{12,34}$ and $R_{23,14}$ [85]............................ 40

3.5 The Hall effect as it is used for the Van der Pauw method [88]. (a) a current flowing through a piece of semiconductor material (b) the electrons flowing due to the current (c) the electrons accumulating at one edge due to the magnetic field (d) the resulting electric field and Hall voltage V_H........................ 44

3.6 The schematic diagram of Hall measurement [86]……………………………. 45

3.7 The block diagrams of TLM pattern: (a) top view and (b) cross-sectional view; (c) R_T versus L plot. [90]…………………………………………….…... 48

3.8 The equivalent resistive network of ohmic contact. [91]……………………... 50

4.1 Oxidation furnace……………………………………………………….. 57

4.2 Pelletron tandem accelerator used for implantation………………………….. 59

4.3 Two examples of the simulated implantation box profiles: (a) the simulated Al implantation box profile for doping concentration $2\times10^{19}cm^{-3}$; (b) the simulated N implantation box profile for doping concentration$1\times10^{19}cm^{-3}$…. 60

4.4 (a) LTLM masks with an enlarged TLM pattern; (b) Hall Effect masks with an enlarged Hall pattern………………………………………………………. 62

4.5 Photoresist Spinner………………………………………………………. 63

4.6 Karl Suss MJB3 UV400 mask aligner equipped with an optical microscope... 64

4.7 (a) Overall sputter-deposition system; (b) Vacuum chamber of Sputter-deposition system; (c) Sample holder disc…………………………………… 65

4.8 (a) Tencor profilometer; (b) Sample holder………………………………….. 67

4.9 (a) Overall view of annealing system; (b) Heating carbon strip with sample clipped on; (c) Carbon box for carbon cap and activation anneal…………… 70

4.10 (a) Overall view of RIE system; (b) Vacuum chamber of RIE system with a cathode inside…………………………………………………………….. 71

4.11 The manual ball-wedge wire bonder……………………………………... 72

4.12 The sequence of events for Hall sample fabrication…………………………. 75

4.13 (a) Top view of Hall sample; (b) Cross-sectional view of Hall sample; (c) Wire-bonded Hall sample…………………………………………………….. 76

4.14 Sequence of ohmic contact fabrication………………………………………….. 77

4.15 (a) LTLM System; (b) Equivalent circuit of TLM measurement…………….. 78

4.16 (a) Overall view of Hall system; (b) Sample holder inserted in cryostat…… 80

5.1 AFM for n type virgin sample with surface roughness 0.39nm………………. 82

5.2 AFM for Al-implanted sample (2×10^{18} cm^{-3}) with surface roughness 0.79nm... 83

5.3 AFM for Al-implanted sample (8×10^{18} cm^{-3}) with surface roughness 0.64nm... 83

5.4 AFM for Al-implanted sample (2×10^{19} cm^{-3}) with surface roughness 0.51nm... 84

5.5 AFM for Al-implanted sample (8×10^{19} cm^{-3}) with surface roughness 0.34nm... 84

5.6 AFM for Al-implanted sample (2×10^{20} cm^{-3}) with surface roughness 0.53nm... 85

5.7 AFM for p type virgin sample with surface roughness 0.73nm………………. 85

5.8 AFM for N-implanted sample (4×10^{18} cm^{-3}) with surface roughness 0.45nm... 86

5.9 AFM for N-implanted sample (1×10^{19} cm^{-3}) with surface roughness 0.44nm... 86

5.10 AFM for N-implanted sample (4×10^{19} cm^{-3}) with surface roughness 0.51nm.. 87

5.11 AFM for N-implanted sample (1×10^{20} cm^{-3}) with surface roughness 0.32nm.. 87

5.12 Resistance as a function of annealing time for NiV7% contacts with a gap 76um……………………………………………………………………….. 89

5.13 TLM data for NiV7% contacts with N implant concentration 1×10^{18} cm^{-3} annealed at 1000^oC /2+1+1+1min/vacuum. Each type of symbol represents the data from one TLM stripe……………………………………………….. 90

5.14 TLM data for NiV7% contacts to N implant concentration 4×10^{18} cm^{-3} annealed at 1000^oC/2+1+1+1min/vacuum. (a) R as a function of interspaces. Each type of symbol represents the data from one TLM stripe. (b) The averaged R values from all TLM stripes with a linear fit…………………….. 90

5.15 TLM data of NiV7% contacts for N implant concentration 1×10^{19} cm^{-3} annealed at 1000^oC/2+1+1+1min/vacuum. (a) R as a function of interspaces. Each type of symbol represents the data from one TLM stripe. (b) The averaged R values from all TLM stripes with a linear fit……………………. 91

5.16 TLM data of Ni80Cr20 contacts for N implant concentration 1×10^{18} cm^{-3} annealed at 1000°C in vacuum. Each type of symbol represents the data from one TLM stripe; (a) annealed at 1000°C/2min/vacuum; (b) annealed at 1000°C/2+2min/vacuum; (c) annealed at 1000°C/2+2+2min/vacuum; (d) The averaged R value of 4 TLM strips with a linear fit, annealed at 1000°C/2min/vacuum………………………………………………………… 93

5.17 TLM data of NiV7% contacts annealed at 1000°C/2min/vacuum for implant concentration (a) 1×10^{18} cm^{-3}, (b) 4×10^{18} cm^{-3}, (c) 1×10^{19} cm^{-3}, (d) 4×10^{19} cm^{-3} and (e) 1×10^{20} cm^{-3}. Each type of symbol represents the data from one TLM stripe……………………………………………………. … 95

5.18 TLM data from one of four prepared samples with implant concentration 1×10^{18} cm^{-3}………………………………………………………………. 97

5.19 TLM results from one of two prepared samples with implant concentration 4×10^{18} cm^{-3}………………………………………………………………. 97

5.20 TLM data from one of two prepared samples with implant concentration 1×10^{19} cm^{-3}…………………………………………………………... 100

5.21 TLM data from one of the two prepared samples with implant concentration 4×10^{19} cm^{-3}…………………………………………………………….. 101

5.22 TLM data from one of the three prepared samples with implant concentration 1×10^{20} cm^{-3}…………………………………………………… 102

5.23 Specific contact resistance vs. implant concentration for N-implanted 4H-SiC……………………………………………………………………..... 106

5.24 TLM data from the sample with Al implant concentration 2×10^{18} cm^{-3}……... 107

5.25 TLM results from the sample with implant concentration 8×10^{18} cm^{-3}……... 108

5.26 TLM data from the sample with implant concentration 2×10^{19} cm^{-3}………... 109

5.27 TLM data from one of the two prepared samples with Al implant concentration 8×10^{19} cm^{-3}…………………………………………………… 110

5.28 TLM data from one of the two prepared samples with implant concentration 2×10^{20} cm^{-3}……………………………………………………………….. 111

5.29 Specific contact resistance vs. implant concentration for N-implanted 4H-SiC……………………………………………………………………..... 113

5.30 Effect of activation temperature on implanted (0001) 4H-SiC……………… 115

5.31 TLM data for N implant concentration $5\times10^{18}cm^{-3}$ activated at 1350^oC/30min/Ar………………………………………………………….. 116

5.32 TLM data for N implant concentration $5\times10^{18}cm^{-3}$ activated at 1450^oC/30min/Ar…………………………………………………………... 117

5.33 TLM data for N implant concentration $5\times10^{18}cm^{-3}$ activated at 1550^oC/30min/Ar…………………………………………………………... 118

5.34 TLM data for N implant concentration $5\times10^{18}cm^{-3}$ activated at 1650^oC/30min/Ar………………………………………………………….. 119

5.35 TLM data for N implant concentration $1\times10^{20}cm^{-3}$ activated at 1350^oC/30min/Ar………………………………………………………….. 120

5.36 TLM data for N implant concentration $1\times10^{20}cm^{-3}$ activated at 1450^oC/30min/Ar………………………………………………………….. 121

5.37 TLM data for N implant concentration $1\times10^{20}cm^{-3}$ activated at 1550^oC/30min/Ar………………………………………………………….. 122

5.38 TLM data for N implant concentration $1\times10^{20}cm^{-3}$ activated at 1650^oC/30min/Ar…………………………………………………………... 123

5.39 TLM data for Al implant concentration $5\times10^{18}cm^{-3}$ activated at 1400^oC/30min/Ar………………………………………………………….. 125

5.40 TLM data for Al implant concentration $5\times10^{18}cm^{-3}$ activated at 1500^oC/30min/Ar………………………………………………………….. 126

5.41 TLM data for Al implant concentration $5\times10^{18}cm^{-3}$ activated at 1600^oC/30min/Ar………………………………………………………….. 127

5.42 TLM data for Al implant concentration $5\times10^{18}cm^{-3}$ activated at 1700^oC/30min/Ar………………………………………………………….. 128

5.43 TLM data for Al implant concentration $1\times10^{20}cm^{-3}$ activated at 1400^oC/30min/Ar………………………………………………………….. 129

5.44 TLM data for Al implant concentration $1\times10^{20}cm^{-3}$ activated at 1500^oC/30min/Ar………………………………………………………….. 130

5.45 TLM data for Al implant concentration $1\times10^{20}cm^{-3}$ activated at 1600^oC/30min/Ar........ 131

5.46 TLM data for Al implant concentration $1\times10^{20}cm^{-3}$ activated at 1700^oC/30min/Ar........ 132

5.47 Hall results for N-implant concentration 1×10^{20} cm^{-3}........ 134

5.48 The activation ratio for N-implantation samples based on Hall carrier concentration measured at RT (semi-insulating material)........ 135

5.49 Hall Mobility as a function of Hall carrier concentration. Circles - data for implanted samples. Squares - data for epitaxial samples [99]. The implanted samples were activated at 1550^oC/30min/Ar. (semi-insulating material)........ 135

5.50 Specific contact resistance for N-implanted (0001) 4H-SiC. The solid circles are the published data for Ni contacts to epitaxial 6H-SiC, and the solid line is a numerical calculation for the epi data. Triangles with error bars are the data for implanted 4H samples plotted as a function of implant concentration, and the squares are the same data plotted as a function of Hall carrier concentration........ 137

6.1 Hall pattern on the new designed Hall mask........ 143

CHAPTER 1

INTRODUCTION

1.1 Purpose of This Thesis

Over the last two decades, wide-band-gap semiconductors such as SiC, GaN, and ZnSe have been intensively studied. This is not only because of the need for electronic devices capable of operation at high power levels, high temperatures and in hostile environments, but also for short-wavelength (blue and UV) optical applications. [1-3]. Electronics based on the existing Si and GaAs semiconductor device technologies can not tolerate greatly elevated temperatures or chemically caustic environments due to the uncontrolled generation of intrinsic carriers and their low resistance to caustic chemicals [4]. However, the wide-band-gap semiconductors SiC and GaN, and perhaps diamond at sometime in the future, with their excellent thermal conductivities, large breakdown fields, and resistance to chemical attack, will be the materials of choice for these applications [5-7].

Among those wide-band-gap materials, SiC is the only compound semiconductor whose native oxide is SiO_2. This places SiC in a unique position to compete with the other materials including silicon for many applications. Much progress has been made in SiC for high temperature and high power devices applications due to the availability of high quality SiC substrates, advances in chemical-vapor-deposition (CVD) growth of

epitaxial structures, and the ability to easily dope the material both n and p-type. The large Si-C bonding energy that makes SiC resistant to chemical attack and radiation damage also ensures its stability at high temperatures. In addition, SiC has a large avalanche breakdown field, excellent thermal conductivity, and a high electron saturation velocity [8]. All these special physical properties make it ideal for high-power operation. Metal-semiconductor (MS) and metal-oxide-semiconductor (MOS) transistors with outstanding high temperature performance have already been demonstrated [9-10]. Blue SiC light-emitting diodes (LEDs) have been available commercially for a number of years [11-14].

Industries such as aerospace, automotive and petroleum have been continuously pushing the development of the cutting-edge technologies which are tolerant of increasingly high temperatures and hostile environments. Wide band gap semiconductor technology could allow bulky aircraft hydraulics and mechanical control systems to be replaced with heat-tolerant *in-situ* control electronics. On-site electronics, actuators, and sensors would reduce complexity and increase reliability [15]. Hydraulic systems, a fire hazard in aircraft, and heat radiators in satellites could then be greatly reduced in size and number yielding considerable weight reductions. In the field of optical devices, shorter wavelength semiconductor lasers can lead to denser optical storage media. Wide band gap emitters and detectors can operate in the green, blue and UV spectral regions.

In order to take the advantages of SiC for these many applications, one of the key technical issues is ohmic contact technology. The main goals of this work are the following:

- Investigate the relationships between contact specific resistance (r_c) and implant concentration (N_D) for both N- and Al-implanted samples.
- Study specific contact resistance (r_c) as a function of activation anneal temperature for a fixed implant concentration (N_D).
- Determine the activation percentage as a function of implant concentration for various activation anneal temperatures.

1.2 Properties of SiC

1.2.1 Polytypism in SiC

As a close-packed material, SiC exists in many polytypes. The SiC polytypes are differentiated by the stacking sequence of the tetrahedrally bonded Si-C bi-layers. The individual bond lengths and local atomic environments are nearly identical, while the overall symmetry of the crystal is determined by the stacking periodicity. All polytypes have a hexagonal frame with a carbon atom situated above the center of a triangle of Si atoms and underneath a Si atom belonging to the next layer Fig. 1.1. The distance, a, between neighboring silicon or carbon atoms is approximately 3.08 Å for all polytypes [16]. The carbon atom is positioned at the center of mass of the tetragonal structure outlined by the four neighboring Si atoms so that the distance from the C atom to each of the Si atoms (marked as C-Si in the Fig. 1.1) is the same. Geometrical considerations give that this distance, C-Si, is $a(3/8)^{1/2}$ i.e. approximately equal to 1.89 Å. The distance between two silicon planes is thus, $a(2/3)^{1/2}$ or approximately 2.52 Å. The height of a unit cell, c, varies between the different polytypes. The ratio c/a therefore differs from

polytype to polytype, but is always close to the ideal for a closed packed structure. This ratio is, for instance, approximately 1.641, 3.271 and 4.908 for the 2H-, 4H- and 6H-SiC polytypes, respectively, whereas the equivalent ideal ratios for these polytypes are $(8/3)^{1/2}$, $2(8/3)^{1/2}$ and $3(8/3)^{1/2}$, respectively. The difference between the polytypes is the stacking order for successive double layers of carbon and silicon atoms.

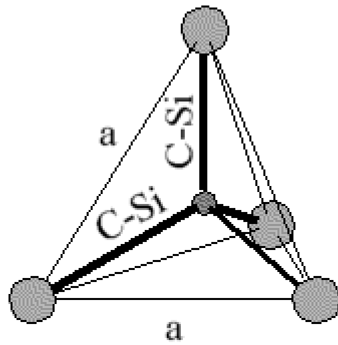

Fig.1.1: The tetragonal bonding of a carbon atom with the four nearest silicon neighbors. The distance a and C-SiC are approximately 3.08Å and 1.89 Å, respectively [17].

More than 200 SiC polytypyes are known to exist. In Fig. 1.2, the stacking sequence is shown for the four most common polytypes, 3C, 2H, 4H and 6H. Generally, the first double layer is called the A position. Then, the next layer will be placed on the B position or the C position according to a closed packed structure. The permutations of these three positions lead to different polytypes when SiC is grown. For instance, the 4H-SiC polytype has a stacking sequence ABACABAC…. The number (4) denotes the periodicity, and the letter (H) indicates that the resulting structure is hexagonal. The 3C-SiC polytype is the only cubic polytype which has a stacking sequence ABCABC… or ACBACB… A common crystalline defect is often seen in 3C-SiC grown on on-axis 6H-

SiC substrates, which is the so-called Double Positioning Boundary (DPB). The defect arises when islands of the two possible stacking sequences ABCABC and ACBACB meet. The growth of 3C-SiC on on-axis 6H-SiC substrates and the evolution and control of the DPB defects had been studied in extensively by Powell *et. al*. [18 - 20].

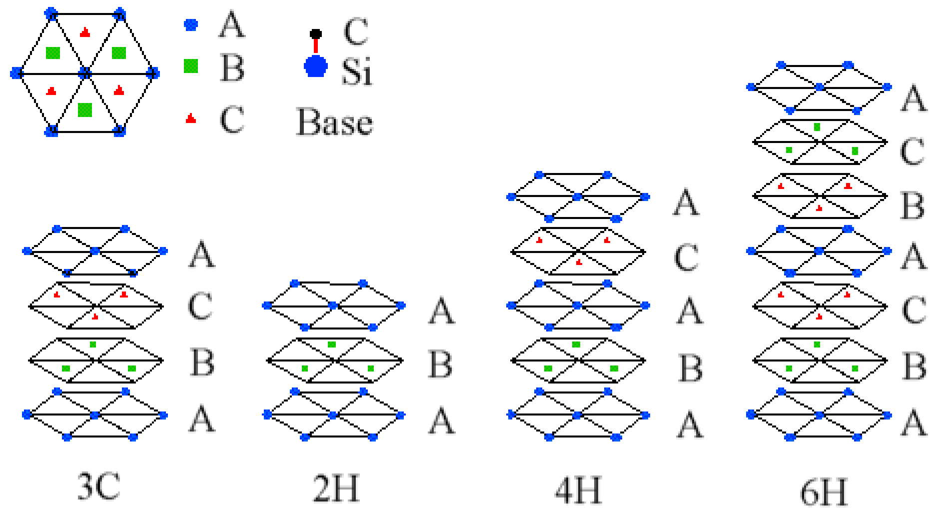

Fig. 1.2: The stacking sequence of double layers of the four most common SiC polytypes [17].

Four hexagonal Miller indices are used to describe the directions in all SiC polytypes except for 3C where the normal cubic notation is used. The first three describes directions in the basal plane. The angle between two adjacent basal plane axis is 120° as shown in Fig. 1.3. By definition, the sum of the first three indices must be zero. In addition, it should be pointed out that one of them is redundant, but is kept for simplicity. The last hexagonal index refers to the c-direction.

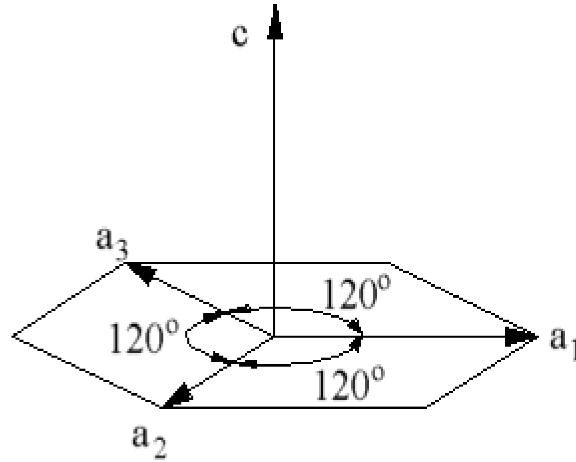

Fig.1.3: The Miller indices describing the hexagonal structure. The c-axis refers to the last index, whereas the first three describes the directions of the basal plane [17].

1.2.2 Semiconducting Properties of SiC

The potential electronic applications of SiC are based on its excellent semiconducting properties. SiC has wide band gap (Eg=2.2-3.3 eV) compared with Si (Eg=1.1eV). Moreover, SiC is the only known compound semiconductor that can be oxidized to form a high quality oxide (SiO_2). N-type epitaxial SiC can be obtained by introducing nitrogen or phosphorous during growth, while P-type epitaxial SiC can be obtained by introducing aluminum or boron. Doping concentrations range from 10^{14} cm^{-3} to greater than 10^{19} cm^{-3} [21]. The selective doping for SiC can not be achieved through thermal diffusion, which is commonly used for Si. This is due to the fairly low diffusion coefficients at temperature below 2000°C for all dopant species. However, it can be achieved by high energy implantation. Compared with nitrogen and phosphorous implantation, the activation percentages for Al and boron are generally much lower.

Table 1.1 shows the relevant material properties of SiC compared with some other semiconductor materials such as GaN, Si and GaAs, *etc*. Most notable are the large

thermal conductivities, breakdown voltages, and saturation velocities of SiC, GaN, and diamond. Maximum operating temperature parameter is calculated as the temperature at which the intrinsic carrier concentration equals 5×10^{15} cm^{-3} and is intended as a rough estimate of the band-gap limitation on device operation [4]. More important for the eventual maximum operating temperature is the physical stability of the material. The large breakdown field and high thermal conductivity, coupled with high operational junction temperature, will allow SiC electronic devices work at extremely high power density with good efficiency.

Property	Si	GaAs	GaP	3C SiC (6H SiC)	4H SiC	Diamond	GaN
Bandgap (eV) At 300 K	1.1	1.4	2.3	2.2 (2.9)	3.3	5.5	3.39
Maximum operating Temperature (K)	600	760	1250	1200 (1580)	900	1400	
Melting point (K)	1690	1510	1740	3103	3103	Phase change	
Physical stability	Good	Fair	Fair	Excellent	Excellent	Very good	Good
Electron mobility RT, cm^2/Vs	1400	8500	350	1000 (600)	1000	2200	900
Hole mobility RT, cm^2/Vs	600	400	100	40	56	1600	150
Breakdown Voltage E_b, 10^6/V/cm	0.3	0.4	-	4	4	10	5
Thermal conductivity C_T, W/cm	1.5	0.5	0.8	5	3.7	20	51.3
Sat. C. elec. Drift vel. υ(sat), 10^7cm/s	1	2	-	2	0.8	2.7	2.7
Dielectric const. K	11.8	12.8	11.1	9.7	9.7	5.5	9

Table 1.1: Comparison of important semiconductor properties for high-temperature electronics.

1.2.3 SiC Substrate Crystal Growth

High quality SiC wafers have been commercially available for a number of years. One major advantage of SiC compared with other wideband-gap competitors is the established, commercialized growth process. Thermal decomposition, growth from a carbon-enriched Si melt and sublimation had been successfully used to obtain SiC in the laboratory [22-24]. The sublimation growth technique is used by Cree, Inc. for the growth of commercial substrates. One hundred centimeter wafers are available with both n- and p-type conductivity over a wide range.

Early SiC growth was performed using liquid-phase epitaxy (LPE) due to the lower growth temperatures (1500-1700°C) compared to sublimation. However, it was difficult to eliminate C contamination from the graphite crucibles for the process in early days [24, 25]. This problem was solved by introducing a graphite-free technique in which the Si melt is suspended in an electromagnetic field [26].

In sublimation growth, the vapor phase SiC is transported to the seed crystal held at a lower temperature. Under the typical growth conditions which are 1800°C for the seed crystal compared with a source temperature in the 2000°C range and a thermal gradient of 20°C/cm across the crystal, a growth rate of 0.7 mm/h has been achieved. Larger growth rates have also been observed at higher source and seed crystal temperatures (2300 and 2200°C) at an ambient pressure of about 5 Torr. In order to form high-quality single-crystal 6H-SiC at higher growth rate, the sublimated SiC clusters must be diffused though porous graphite under carefully controlled thermal and pressure

gradients. Reduced defect densities were noted when the source was situated below the seed crystal. Sublimation is also a suitable technique for epitaxial growth of SiC.

As the growth method of choice, chemical vapor deposition (CVD) has replaced LPE and sublimation. Both low- and atmospheric-pressure CVD have been successfully applied to SiC epitaxy. For 1 inch wafers, atmospheric-pressure CVD is good enough to provide adequate uniformity. Low pressure is preferred when the deposition is over larger area substrates. Gas-source molecular-beam epitaxy (GSMBE) has also been used for SiC epitaxial growth when low growth rate is not an issue.

1.2.4 Ohmic Contacts to SiC

Many vital semiconductor device characteristics such as high frequency and high power performance depend critically on and are often limited by ohmic contact resistances. For wide band gap semiconductors, the contact resistance is especially important due to the large Schottky barrier heights at the metal-semiconductor interface. This problem can often be alleviated in other semiconductors by choosing a metal with an optimal barrier height. However, little flexibility is available for SiC because of its Fermi level being pinned by defects at the metal-semiconductor interface.

Nickel-based alloys are the most widely used metals for fabricating ohmic contacts on n-SiC [27-29]. Nickel reacts with SiC and forms nickel silicides ($NiSi_2$, NiSi and Ni_2Si) at temperatures greater than 900°C. These silicides are thermally stable at lower temperatures [28, 29]. The reported specific contact resistance varies between 1×10^{-2} Ω.cm^2 and 1×10^{-6} Ω.cm^2 [30], depending on the doping concentration and processing method.

Aluminum based metal alloys, including AlTi and NiAl, are widely used for ohmic contact fabrication on p-SiC [31, 32]. Alumimum spikes into SiC at a temperature greater than 800°C and forms a "field emission" ohmic contact. The disadvantage for Al-based contacts is that Al is more easily oxidized during long-term operation. Ohmic contacts with excellent uniformity and reproducibility have been reported with Al-Ti alloys [33-35]. Al70Ti30 is considered most suitable to for contacts on heavily doped p-type SiC due to its liquid phase present at the anneal temperature (1000°C) [35]. The reported specific contact resistance varies between 1×10^{-2} Ω.cm^{2} and 1×10^{-6} Ω.cm^{2} [30], depending on doping concentration.

1.2.5 Devices and Applications

SiC Field-effect Transistors

FETs have long been the mainstay of power switching applications due to their ease of fabrication and amenability to large-scale integration. Several types of SiC FETs

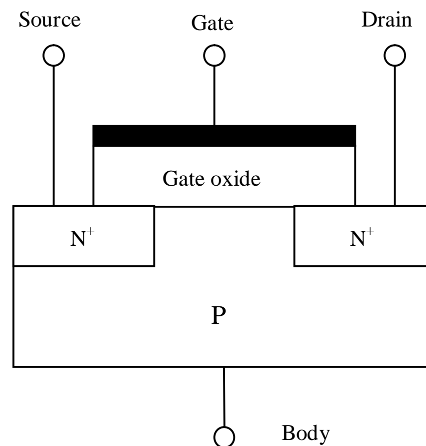

Fig. 1.4: The basic structure of a MOSFET.

have been developed, including MOSFETs, junction FETs (JFET), and metal-semiconductor FETs (MESFET). All the FETs have a structure which is similar to the MOSFET structure shown in Fig. 1.4. The advantages of SiC FETs include the extremely low leakage currents, large breakdown voltage and high operating temperature [36-39].

SiC Light-emitting Diodes (LEDs)

Even though SiC has indirect band gap, it can be made to exhibit electroluminescence across the entire visible spectrum by introducing various impurities. The first blue SiC LED was fabricated by Brander and Sutton [40], and it has developed quickly. Presently, Cree Inc. markets SiC blue LEDs which have a pure blue emission centered at 470 nm [13]. Groups at Siemens AG, Sanyo, and Sharp have also developed prototype devices, and some have reached the marketplace. Due to its indirect band gap, the efficiency of SiC LED is only 0.02%-0.03%. The radiation rate is 18.3 μW at 25 mA and 3V forward bias with a spectral half-width of 69 nm [13]. However, it can be partially compensated by flowing higher current. The radiation rate of 36 μW has been achieved at 50mA [13].

It has been found that the main light-producing mechanisms are donor-to-acceptor (DA) pair recombination (~480 nm), bound exciton recombination at localized Al centers (~455 nm), and free-exciton recombination (~425 nm). The key to reaching shorter wavelengths is reducing the background N contamination which increases exciton related luminescence. Despite the suggestion that an increased DA density could result in an overall increase in high power performance, the efficiency actually decreases at higher

power levels. This is believed to be partly due to a saturation of the DA pair levels [13]. The basic structure of Light-emitting Diode is shown in Fig. 1.5.

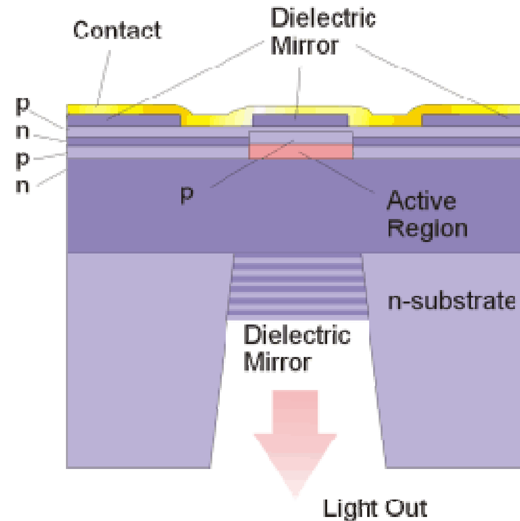

Fig. 1.5: The basic structure of Light-emitting Diode.

SiC Bipolar Transistor

SiC npn bipolar junction transistors (BJTs) were first fabricated from CVD-grown layers by Muench, Hoeck, and Pettenpau [41]. The corresponding current gain is 4-8 with low leakage ($10^{-5} A/cm^2$) at $V_{cE} = 40V$. A current gain of 10.2 measured at 400 ^{o}C was observed on 6H-SiC BJTS [42]. Recently, Cree has reported high performance/high voltage npn bipolar junction transistors in 4H-SiC for application in low frequency (<5MHz) power systems. The devices showed a maximum current gain of 11 with the specific on-resistance (8 m$\Omega\cdot$cm^2) at room temperature [42]. However, the current gain in SiC BJTs is limited by the short lifetime and low diffusion coefficient of minority carriers in the base. Moreover, device characteristics are degraded at high power/high frequency due to both higher ohmic contact resistance and the low hole concentrations in the p-base

region resulting from the large acceptor ionization energies in SiC. Fig. 1.6 shows the basic structure of an npn SiC bipolar transistor.

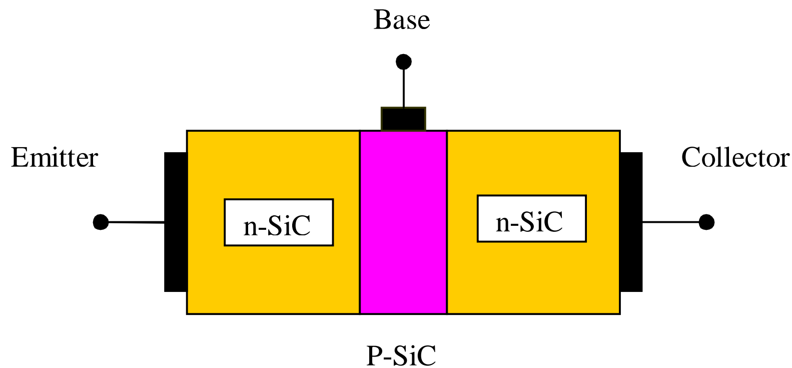

Fig. 1.6: npn SiC Bipolar Transistor

SiC Photodiodes

The SiC photodiode was one of the first wide band gap devices on the market. 4H-SiC visible-blind avalanche photodiodes (RAPDs) with optical gain of 500 and responsivity of 106 A/W have been demonstrated [43]. The peak photo-responsivity is more than 600 times higher than that of conventional 6H-SiC photodiodes [44].

SiC photodiodes are mainly used for UV optical detection due to their insensitivity to longer wavelengths and their very small dark current levels, even at elevated temperatures. The sensitivity of SiC photodiodes is four orders of magnitude higher compared to Si UV detectors due to low dark current [45]. The ruggedness of SiC is another important advantage. Many of the applications for UV detection involve hostile environments such as in situ combustion monitoring and satellite-based missile plume detection. Other applications requiring the sensitivity of wide band gap semiconductor detectors are air quality monitoring, gas sensing, and personal UV exposure dosimetry. The cross section of SiC photodiode device is shown in Fig. 1.7.

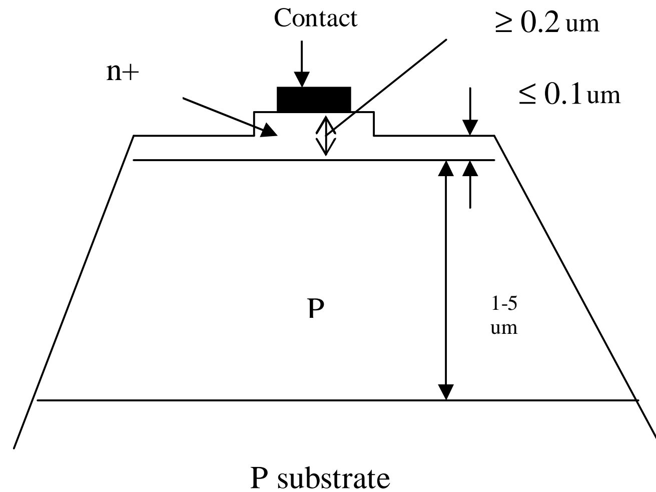

Fig. 1.7: SiC photodiode device cross section.

SiC Schottky Barrier Rectifiers

SiC is also an ideal material for rectifying applications due to its power handling capability at high temperature. SiC diode rectifiers have been fabricated by Cree Inc. [13]. The prime benefits of the SiC Schottky barrier diode (SBD) lie in its ability to switch very quickly (<50 ns), with almost zero reverse-recovery charge during high temperature operation. Comparable silicon PiN diodes have a reverse-recovery charge of 100-500 nC and take at least 100 ns to turn-off. Si SBDs are not viable in the 600 V range because of their large on-state voltage drops. Six hundred volt SiC SBDs are presently available from Cree [46] with the forward current ratings between 1 and 20A.

1.3 Scope of the Thesis

In this work, nitrogen implantation was performed into p-type (0001) 4H-SiC with implant concentrations of 1×10^{18} cm^{-3}, 4×10^{18} cm^{-3}, 1×10^{19} cm^{-3}, 4×10^{19} cm^{-3} and

1×10^{20} cm^{-3}. Aluminum was implanted into n-type (0001) 4H-SiC with concentrations of 2×10^{18} cm^{-3}, 8×10^{18} cm^{-3}, 2×10^{19} cm^{-3}, 8×10^{19} cm^{-3} and 2×10^{20} cm^{-3}. The implantation box files were simulated by using the software 'SRIM' [47]. The surface roughness of the N- and Al-implanted 4H SiC (0001) was investigated by AFM.

In order to determine the relationships between specific contact resistance (r_c) and implant concentration (N_D), linear transmission line model measurements (LTLM) were carried out for both N- and Al-implanted samples. The specific contact resistances for fixed implant concentrations (5×10^{18} and 1×10^{20} cm^{-3}) were also studied as a function of activation anneal temperature for both N- and Al-implanted samples.

In order to determine the activation percentages as a function of the implant concentrations, Hall samples were prepared and measured for both N- and Al-implants.

CHAPTER 2

METAL-SEMICONDUCTOR CONTACTS

One of the key technical issues for a semiconductor device is the metal-semiconductor (MS) contact. An ideal MS contact can either be a rectifying (Schottky) or non-rectifying (ohmic). Metal-semiconductor combinations generally upon preparation are rectifying due to the Schottky barrier at the metal-semiconductor interface. Schottky contacts are essential for current switching and rectification. Ohmic contacts may be considered a limiting case of Schottky contacts with a modified Schottky barrier. A good ohmic contact, usually formed by depositing a metal on the semiconductor, does not perturb device characteristics and is stable both electrically and mechanically. The contact resistance should be negligible compared to the device resistance. The ohmic contact provides interconnection between a device and the outside world.

2.1 Schottky Contact

A Schottky barrier refers to a metal-semiconductor contact having a large barrier height (i.e. $f_B > kT$) and a low semiconductor doping concentration, which is less than the density of states in the conduction band or valence band. The potential barrier between the metal and the semiconductor can be identified on an energy band diagram.

Fig.2.1 shows the energy levels of a metal and semiconductor before and after contact. As can be seen in Fig. 2.1 (a), the vacuum levels of the metal and the semiconductor are the same. As they are brought together, the Fermi energies of the two materials must be equal under thermal equilibrium [Fig. 2.1 (b)].

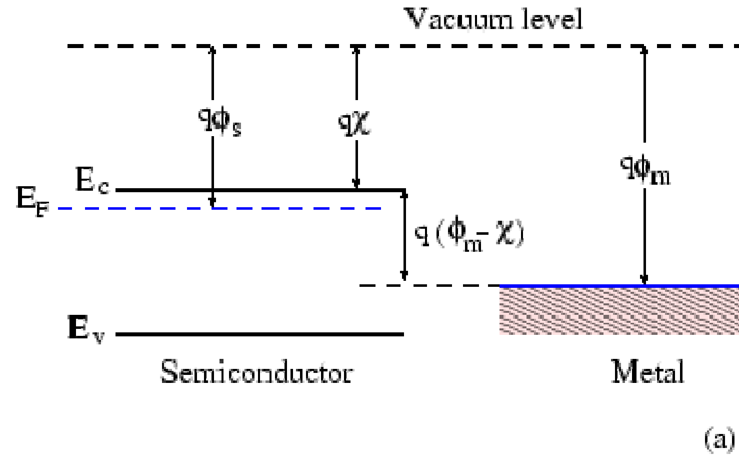

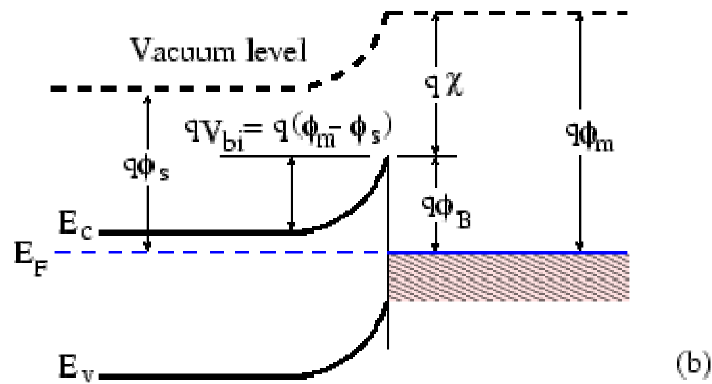

Fig. 2.1: (a) Energy band diagram of a metal adjacent to an n-type semiconductor under thermal equilibrium condition [49]. (b) metal-semiconductor contact in thermal equilibrium [49].

The barrier height f_B is defined as the potential difference between the Fermi energy of the metal and the band edge where the majority carriers reside. For n-type semiconductors, the barrier height is

$$f_{Bn} = f_m - c\,, \tag{2.1}$$

where f_m is the work function of the metal and c is the electron affinity. The work function of selected metals as measured in vacuum can be found in Fig. 2.2.

For p-type material, the barrier height is given by the difference between the valence band edge and the Fermi energy in the metal,

$$f_{Bp} = \frac{E_g}{q} + c - f_m \tag{2.2}$$

A metal-semiconductor junction will therefore form a barrier for electrons and holes if the Fermi energy of the metal is located between the conduction and valence band edges.

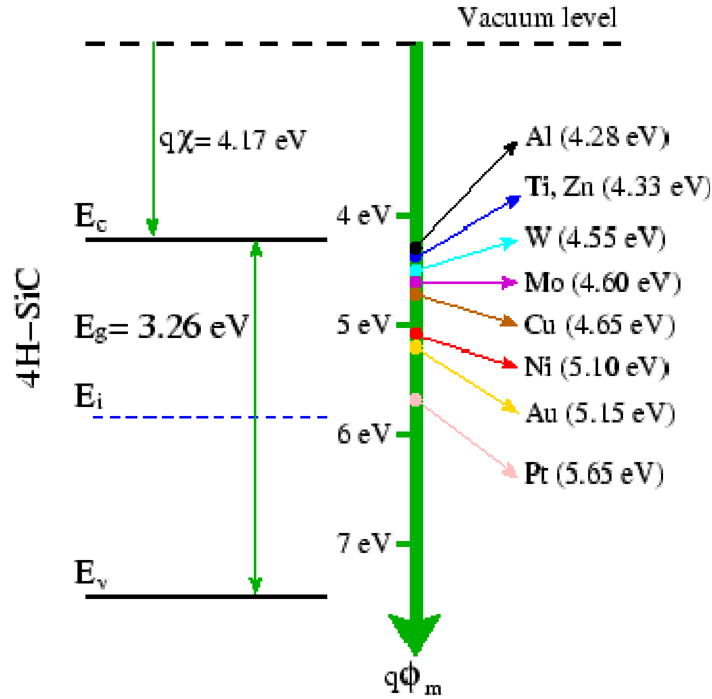

Fig. 2.2: Energy band diagram of the selected metals and 4H-SiC [50].

The measured barrier heights for selected metal/4H-SiC junctions are listed in Table 2.1 [51, 52]. These experimental barrier heights depend on the surface polarity of SiC (Si- and C-face), and often differ from those calculated using equations 2.1 and 2.2. This is due to the detailed behavior of the metal-semiconductor interface. The ideal metal-semiconductor theory assumes that both materials are pure and that there is no interaction between the two materials or any interfacial layer. Chemical reactions between the metal and the semiconductor alter the barrier height as do interfacial layers (e.g., thin oxides) and interface states at the surface of the semiconductor. Furthermore, one finds that the barrier heights reported in the literature can vary widely due to different surface cleaning procedures.

	Al	Ti	Zn	W	Mo	Cu	Ni	Au	Pt
f_m	4.28	4.33	4.33	4.55	4.69	4.65	5.10	5.15	5.65
f_B (Si-face)		1.12					1.69	1.81	
f_B (C-face)		1.25					1.87	2.07	
f_B (Calculated)	1.01	1.06	1.06	1.28	1.33	1.38	1.63	1.68	2.08

Table 2.1: Work function of selected metals and their measured and calculated barrier height on n-type 4H-SiC [49]

Schottky contacts are generally made on lightly doped semiconductors. Rectification in Schottky contacts can be explained by Bethe’s thermionic emission

theory assuming the carrier possesses enough energy to surmount the Schottky barrier in order to pass from one material to the other. The current density is calculated according to the thermionic emission condition [53] neglecting tunneling currents:

$$\mathbf{n} \cdot \mathbf{J}_n = -q \cdot \upsilon_n \cdot (n - n_s) \tag{2.3}$$

$$\mathbf{n} \cdot \mathbf{J}_p = q \cdot \upsilon_p \cdot (p - p_s) \tag{2.4}$$

where n, p, n_s and p_s are carrier densities and surface carrier densities, respectively, for electrons and holes, and v_n and v_p are thermionic recombination velocities for electrons and holes, respectively.

$$\upsilon_\nu = \sqrt{\frac{k_B \cdot T_L}{2\pi \cdot m_\nu}} = \frac{4\pi \cdot m_\nu \cdot (k_B \cdot T_L)^2}{N_\nu \cdot h^3}, \quad \nu = n, p \tag{2.5}$$

T_L is the lattice temperature, m_ν is the effective carrier mass, and N_ν is the concentration of dopant.

The effective *Richardson constant* A^* is written as

$$A^* = \frac{4\pi \cdot q \cdot m_\nu \cdot k_B^2}{h^3}, \quad \nu = n, p \tag{2.6}$$

Therefore,

$$\upsilon_\nu = A^* \cdot \frac{T_L^2}{q \cdot N_\nu}, \quad \nu = n, p \tag{2.7}$$

where A^* depends on the effective mass which has a theoretical value of 146 and 72 A-$cm^{-2}K^{-2}$ for n-type 4H- and 6H-SiC, respectively [50].

The carrier concentrations at the surface are given by [49]

$$n_s = N_c \cdot \exp\left(\frac{-E_c - E_w}{k_B \cdot T_L}\right) \tag{2.8}$$

$$p_s = N_v \cdot \exp\left(\frac{E_v - E_w}{k_B \cdot T_L}\right) \tag{2.9}$$

where E_w is the work function energy $E_w = q f_{wf}$. The work function difference f_{wf} is defined as the difference between the work function of the metal and that of the semiconductor. For n-type material it is

$$f_{wf} = f_m - c - \frac{E_c - E_{F,n}}{q} \tag{2.10}$$

Similarly, for p-type material we have

$$f_{wf} = c + \frac{E_c - E_{F,p}}{q} - f_m \tag{2.11}$$

It should be pointed out that the equations 2.1 and 2.2 are equivalent to the more commonly used equations 2.12 and 2.13 [53].

$$J_n = \frac{4pq \cdot m_n \cdot (k_B \cdot T_L)^2}{h^3} \exp(\frac{q \cdot f_m - E_c}{k_B \cdot T_L})\left[\exp\left(\frac{q \cdot f_{Bn} - q \cdot f_m}{k_B \cdot T_L}\right) - 1\right] \tag{2.12}$$

$$J_p = \frac{4pq \cdot m_p \cdot (k_B \cdot T_L)^2}{h^3} \exp(\frac{E_v - q \cdot f_m}{k_B \cdot T_L})\left[\exp\left(\frac{q \cdot f_m - q \cdot f_{Bp}}{k_B \cdot T_L}\right) - 1\right] \tag{2.13}$$

The Schottky contact boundary conditions are similar to the ones which apply for the Ohmic contact. The carrier temperatures T_n and T_P are set equal to the lattice temperature T_L , which is further discussed in section **2.2**.

2.2 Ohmic Contact

A metal-semiconductor combination can be converted into an ohmic contact with certain processing steps which modify the shape of Schottky barrier. The modified barrier is either too low or too thin to produce an asymmetric I-V characteristic.

In many cases, the doping of the semiconductor immediately beneath the metal determines the characteristic of the contact. A metal deposited on a heavily doped semiconductor will have the same barrier height as the same metal deposited on a more lightly doped sample of the same semiconductor. However, the barrier will be much thinner and therefore affords carriers, holes or electrons, the chance to quantum mechanically tunnel through the Schottky energy barrier as opposed to traveling over the barrier.

Energy band diagrams depicting field emission, thermionic field emission, and thermionic emission for an n-type semiconductor is shown in Fig. 2.3. Field emission occurs when the Schottky barrier is sufficiently thin to allow tunneling at the semiconductor Fermi energy, E_{Fs}. When the barrier is not sufficiently thin due to insufficient doping, the electrons tunnel at energy greater than the semiconductor Fermi energy. For lightly doped semiconductor, the barrier is too thick at all energies, therefore no tunneling can occur. For this case, carriers must have sufficient energy to pass over the Schottky barrier, which is known as thermionic emission.

For Ohmic contacts, the metal quasi-FERMI level is equal to the semiconductor quasi-FERMI level. Thus, the contact potential f_S at the semiconductor boundary can be written as

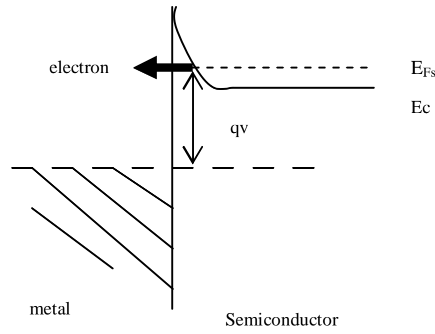

(a) Field emission

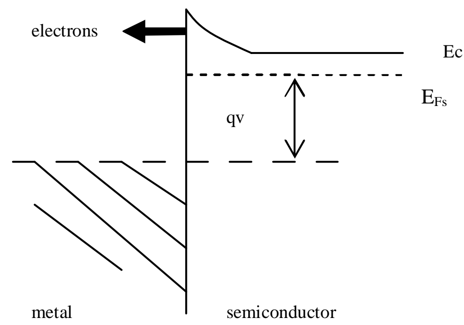

(b) Thermionic field emission

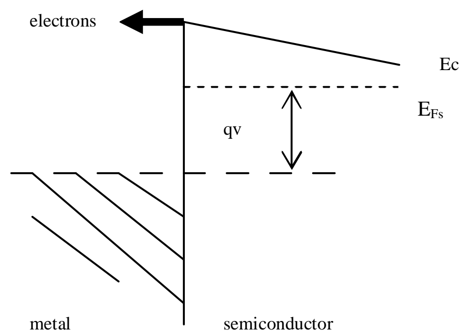

(c) Thermionic emission

Fig.2.3: Energy band diagram depicting field emission, thermionic field emission, and thermionic emission for an n-type semiconductor [30].

$$f_s = f_m + y_{bi}\,, \tag{2.14}$$

where y_{bi} is the built-in potential [54],

$$y_{bi} = -\frac{k_B \cdot T_L}{q} \cdot \ln\left(\frac{1}{2N_1}(N + \sqrt{N^2 + 4N_1N_2}) \right)$$

$$= -\frac{k_B \cdot T_L}{q} \cdot \ln\left(\frac{1}{2N_2}(-N + \sqrt{N^2 + 4N_1N_2}) \right) \tag{2.15}$$

and N is the net concentration of dopants and other charged defects at the contact boundary. The variables N_1 and N_2 are defined by

$$N_1 = N_c \cdot \exp\left(\frac{-E_c}{k_B \cdot T_L} \right) \tag{2.16}$$

$$N_2 = N_v \cdot \exp\left(\frac{-E_v}{k_B \cdot T_L} \right) \tag{2.17}$$

By setting the carrier concentrations in the semiconductor are equal to the carrier concentrations at the contact, we have

$$n_s = N_c \cdot \exp\left(\frac{-E_c + q \cdot y_{bi}}{k_B \cdot T_n} \right) \tag{2.18}$$

$$p_s = N_v \cdot \exp\left(\frac{E_v - q \cdot y_{bi}}{k_B \cdot T_p} \right) \tag{2.19}$$

where T_n and T_p are carrier temperatures for electrons and holes, respectively, both of which are equal to the lattice temperature T_L.

In the case of a thermal contact, the lattice temperature T_L is calculated using a specified contact temperature T_C and thermal resistance R_T. The thermal heat flow density $\mathbf{S_L}$ at the contact boundary is:

$$\mathbf{n} \cdot \mathbf{S}_{\mathrm{L}} = \frac{T_{\mathrm{L}} - T_C}{R_{\mathrm{T}}} \tag{2.20}$$

If no thermal resistance is specified, an isothermal boundary condition will be assumed, and the lattice temperature T_L will be set equal to the contact temperature T_C ($T_L = T_C$).

In the case of drift diffusion simulation with self-heating, an accounting of the additional thermal energy must be made. This thermal energy is produced when the carriers have to surmount the potential difference between the conduction or valence band and the metal quasi-FERMI level. The energy equation reads

$$\mathbf{J}_n \cdot \left(\frac{E_c}{q} + f_m \right) + \mathbf{J}_p \cdot \left(\frac{E_v}{q} + f_m \right) = \mathrm{div}\mathbf{S}_{\mathrm{L}} \tag{2.21}$$

where div $\mathbf{S}_{\mathbf{L}}$ denotes the surface divergence of the thermal heat flux at the considered boundary.

2.3 Ohmic Contacts to SiC

As mentioned previously, many vital parameters of semiconductor devices (e.g. operating temperature, switching speed and high power performance) depend critically on ohmic contact resistance. The issue is especially important for wide band gap semiconductors due to the large Schottky barrier heights at the metal-semiconductor interface. In other semiconductors, this problem can be partially solved by choosing an optimum metal in order to achieve a lower barrier height. However, little flexibility is available in SiC due to the Fermi level being pinned at the surface. The best ohmic

contact resistance values for moderately doped SiC still ranges from 10^{-4} Ω.cm^2 to 10^{-3} Ω·cm^2 for both n- and p-type contacts [30].

2.3.1 n-type α-SiC

Although much of the previous work for ohmic contact development was performed with 6H SiC, the focus now has been shifted to 4H-SiC due to its superior bulk mobility characteristics [30]. Contact resistances on n-type α–SiC (6H and 4H) have been successfully decreased over the last two decades to levels that are now difficult to measure. For very heavily doped 6H- and 4H-SiC (> 10^{19}cm^{-3}), contact resistances in the order of 10^{-5} Ω.cm^2 are now common.

The dominant mechanism forming ohmic contacts to n-SiC is the formation of the metal silicide. Studies have shown the formation of contacts on both 6H and 4H materials has the same mechanism. As predicted, the specific contact resistance increases with increasing barrier height and decreases tremendously for heavily doped materials.

Nickel is the most widely used metal for contacts on n-SiC. It makes a relatively good ohmic contact on moderately doped material (~10^{18} cm^{-3}). Nickel silicide is formed during the high temperature annealing process with specific contact resistances between 1×10^{-6} to 1×10^{-2} Ω.cm^2, depending on the doping concentration. Both Rutherford backscattering spectroscopy and Auger electron spectroscopy have shown that high temperature anneal leads to the reaction of Ni with SiC forming nickel silicide. The formation of nickel silicide has also been observed by Liu, *et al* [29]. At high temperature, nickel reacts with SiC and replaces carbon.

Other metals can also be used to form n-type contacts. Research shows that metals such as Hf, Co, and Ta can also produce ohmic contacts with physical and electrical properties similar to the nickel silicide contact [30]. Binary alloys and multilayer contacts have also been investigated. For example, TiN and TiW contact characteristics have been reported by Glass, *et al.* [55, 56] and Crofton, *et al.* [57], respectively. TiN has a low work function which decreases the barrier height at MS interface. X-ray photoelectron spectroscopy (XPS) shows that a metal-insulator-semiconductor (MIS) structure forms at the MS interface due to the presence of a thin insulating layer (0.5-1.5 nm) of silicon nitride. The MIS structure can improve the ohmic behavior [60]. A list of metals used for ohmic contacts on n-type α-SiC is shown in Table 2.2.

2.3.2 P-type a-SiC

It is more difficult to form ohmic contacts on p-type SiC due to the higher Schottky barrier heights (SBHs) at the MS interface. Therefore, the ohmic contact on p-SiC is mainly created by reducing the thickness of Schottky barrier via high doping concentration instead of lowering the SBH. When tunneling dominates the current transport as occurs for sufficiently high doping concentrations and finite barrier height, the specific contact resistance varies according to the following relation [30]

$$r_c \propto \exp\left(\frac{f_B}{\sqrt{N}}\right) \tag{2.22}$$

where r_c is the specific contact resistance; f_B is the Schottky barrier height and N is the carrier concentration.

Metallization	SiC carrier Conc. (cm^{-3})	Annealing condition	r_c (Ωcm^2)	Method of r_c measurement	Ref.
Ni	4.5×10^{17}	1000°C, 20s	1.7×10^{-4}	TLM	[59]
Ni	4.7×10^{18}	950°C, 5mins	mid 10^{-2}	4-pt. probe	[57]
Ni	7.9×10^{18}	950°C, 2mins	$< 5\times10^{-6}$	TLM	[28]
Ni	9.8×10^{17}	1050°C, 5mins	10^{-3}-10^{-4}	TLM	[60]
Ni	4.5×10^{20}	1000°C, 5mins	1×10^{-6}	cont.	[27]
Ni	3.2×10^{17}	1000-1200°C,	1.3×10^{-5}-	TLM	[61]
	1.4×10^{18}	1mins	3.6×10^{-6}		
Ni	2×10^{18}- 2×10^{19}	950-1000°C	4×10^{-4} - $\sim10^{-6}$	TLM	[62]
Mo	2×10^{18}- 2×10^{19}	950-1000°C	4×10^{-4}-10^{-5}	TLM	[62]
Ni60%Cr40%	4.7×10^{18}	950°C, 5mins	1.8×10^{-3}	Circular TLM	[57]
Ti	2×10^{18}- 1×10^{20}	as-deposited	1×10^{-2}-2×10^{-5}	Circular TLM	[63]
W	3×10^{18}- 1×10^{19}	1200-1600°C	5×10^{-3}-1×10^{-4}	4-pt. probe	[64]
TiW	4.7×10^{18}	600°C, 5mins	7.8×10^{-4}	Circular TLM	[57]
Mo	$> 1\times10^{19}$	as-deposited	$\sim1\times10^{-4}$	4-pt. probe	[65]
				TLM	
Ta	$> 1\times10^{19}$	as-deposited	$\sim1\times10^{-4}$	4-pt. probe	[65]
				TLM	
Ni, Ni/W Ni/Ti/W	10^{17}- 10^{18}	1000-1050°C 5-10min	10^{-3}-10^{-6}	TLM	[66]
Cr/W Cr/Mo/W	10^{17}- 10^{18}	1000-1050°C 5-10min	10^{-2}-10^{-4}	TLM	[66]
TiC	4×10^{19}	Etched at 1300°C 15min in H_2	1.3×10^{-5}	TLM	[67]

Table 2.2: Some ohmic contacts on n-type α-SiC. The layers in multi-layered contacts are separated with slashes; layers at the surface to the interface with SiC proceed from right to left. [58]

Al and Al alloys are conventionally used to form ohmic contacts on p-SiC. Aluminum may diffuse a few nanometers into SiC during the annealing process, which can lead to enhanced p-type doping concentration near the surface. This high doping concentration narrows the Schottky barrier which makes easier for carriers to tunnel through. However, the low melting point and high oxidation rate of Al still cause problems for ohmic contact processing. The melting point can be increased by using Al alloys, e.g., Al-Ti of different compositions. The difficulties due to high oxidation rate can be managed with careful processing. It has been reported that Al is lost to the annealing environment from Al90Ti10 alloy layer at 1000°C [33].

Non-aluminum based contacts have also been studied for SiC. Platinum which has high work function (5.65eV) is used in order to reduce the Schottky barrier height. The ohmic characteristics of Pt contacts have been observed either as deposited or after contact anneals at 850°C [60].

Double-layer contacts (160 nm Silicon on 50 nm Cobalt) on 6H-SiC with a p-type doping concentration of 2×10^{19} cm^{-3} were annealed sequentially at 500°C for 5 hours, and then 900°C for 2 hours [68]. The reported specific contact resistance was as low as 4×10^{-6} $\Omega\cdot cm^{2}$. Rutherford backscattering spectrometry (RBS) indicated that $CoSi_2$ is formed with the absence of carbon at the interface. Silicon in the contact layer is used to prevent the formation of a C-rich phase has been reported as the cause of high contact resistance [68]. A list of metals used for ohmic contacts on p-type α-SiC is shown in Table 2.3.

Ohmic contacts on either n-type or p-type SiC can also be formed without annealing by metal deposition directly onto very heavily doped region of the sample (doping concentration ~ 1×10^{20} cm^{-3}). It has been reported that as deposited Mo, Ta, and

Ti contacts on heavily doped SiC exhibit ohmic characteristics with specific resistances the order of $10^{-4}\ \Omega\cdot cm^2$ [69]. .

2.3.3 n-type b-SiC

Nickel is also the most commonly used metal for ohmic contacts to β-SiC [74-78]. Other metals such as Au-Ta, Ti, W, TaSi2, and Al are also used [75]. In addition, multilevel metallization schemes have been extensively studied. Shor, *et al.*, [79] investigated multilevel metallization schemes based on Ti and W for high temperature (650C-750°C) applications. Multilevel contact metallization concerns reactivity, oxidation and diffusivity within the metal layers and with the SiC. Au/Pt/TiN/Ti has been reported to be the most promising metallization scheme to n-type β-SiC since it can remain ohmic for 31 hours at 650°C. The TiN layer blocks diffusion from the top layers to the SiC. A list of metals used for ohmic contacts on n-type β-SiC is shown in Table 2.4.

Metallization	SiC carrier Conc. (cm^{-3})	Annealing condition	r_c (Ωcm^2)	Method of r_c measurement	Ref.
Al	1.8×10^{18}	700°C, 10min	1.7×10^{-3}	TLM	[57]
Al	8×10^{18}	800°C, 10mins	10^{-2}-10^{-3}	TLM	[60]
Al-Ti	5×10^{15}- 2×10^{19}	1000°C, 5mins	2.9×10^{-2}- 1.5×10^{-5}	Circular TLM	[70]
Ta	> 1×10^{19}	as-deposited	7×10^{-4}	TLM	[65]
Ti	> 1×10^{19}	as-deposited	3×10^{-4}	TLM 4pt. probe	[65]
Mo	> 1×10^{19}	as-deposited	2×10^{-4}	TLM	[65]
				4pt. probe	
Al/Ti	Al implant Dose: 1×10^{15}	500°C, 20min (1650°C, 30min)	5.6×10^{-4}	4pt. probe	[71]
Al/Ti/Al	2×10^{18}- 2×10^{19}	950-1000°C	4×10^{-4}- ~10^{-5}	TLM	[72]
W	NR	1900°C	NR	-	[73]
Al/W/Au-W/W	NR	1900°C, 2min	2-5×10^{-4}	4-pt. probe	[64]

Table 2.3: Some ohmic contacts on p-type α-SiC. The layers in multi-layered contacts are separated with slashes; layers at the surface to the interface with SiC proceed from right to left [58].

Metallization	SiC carrier Conc. (cm^{-3})	Annealing condition	r_c (Ωcm^2)	Method of r_c measurement	Ref.
Al	5×10^{16}	as-deposited	1.6×10^{-1}	3-cont.	[75]
Ni	5×10^{16}	1250°C, 5mins	1.4×10^{-1}	3-cont.	[75]
Cr	5×10^{16}	1250°C, 5mins	$7.6\text{-}\ 9.2\times10^{-3}$	3-cont.	[75]
Ti	$10^{17}\text{-}10^{18}$	300°C, 30-90mins	7×10^{-4}	4-point	[80]
W	$10^{17}\text{-}10^{18}$	as-deposited 600°C, 10mins	1.5×10^{-2}	4-point	[80]
Ta	5×10^{19}	as-deposited 1000°C, 1hr	$4.3\times10^{-6}\text{-}\ 7\times10^{-7}$	Circular TLM	[81]
Re	5×10^{19}	as-deposited 900°C, 30min	$1\times10^{-4}\text{-}\ 1\times10^{-5}$	Circular TLM	[81]
Pt	5×10^{19}	as-deposited 500°C, 30min	$1\times10^{-5}\text{-}\ 6\times10^{-6}$	Circular TLM	[81]
Au/Pt/Ti	$10^{16}\text{-}10^{17}$	650°C, 1hr	1.1×10^{-4}	4 pt. probe	[79]
Au/Pt/W	$10^{16}\text{-}10^{17}$	650°C, 8hr	2×10^{-4}	4-pt. probe	[79]
Au/Pt/TiN/Ti	$10^{16}\text{-}10^{17}$	650°C, 31hr	1.4×10^{-4}	4-pt. probe	[79]
Pt/TiW/Ti	$10^{16}\text{-}10^{17}$	650°C, 31hr	2.6×10^{-4}	4-pt. probe	[79]
$TaSi_2$	5×10^{16}	850°C, 5min	2×10^{-2}	3-cont.	[75]
Ti Si_2	$10^{17}\text{-}10^{18}$	1000°C, 10s + 450°C, 390min	1.1×10^{-4}	4-point	[80]
W Si_2	$10^{17}\text{-}10^{18}$	1000°C, 10s + 450°C, 390min	3.9×10^{-4}	4-point	[80]

Table 2.4: Some ohmic contacts on n-type β-SiC. The layers in multi-layered contacts are separated with slashes; layers at the surface to the interface with SiC proceed from right to left [58].

2.3.4 P-type b-SiC

It has been well known that the crystal quality of β-SiC is not as good as that of α-SiC due to a much higher defect density [60]. The reported specific contact resistance is 3.1×10^{-2} Ω.cm^2 for aluminum contacts annealed at 880°C for 3 min on p-type β-SiC with doping concentration 1×10^{16} cm^{-3}, which is in the same order as that of α-SiC [35]. Aluminum alloys and higher annealing temperature have also been tried. However, results do not show much improvement. It should be noted that the specific contact resistance for p-type β-SiC is sometimes not stable [60]. Probably, this is because of poor crystal quality and state of the SiC surface prior to metal deposition. A list of metals used for ohmic contacts on p-type β-SiC is shown in Table 2.5.

Metallization	SiC carrier Conc. (cm^{-3})	Annealing condition	r_c (Ωcm^2)	Method of r_c measurement	Ref.
Al	1×10^{16}	880°C, 3min	3.1×10^{-2}	3-cont.	[75]
Ni	10^{17}- 10^{18}	as-deposited 700°C, 15mins	4.1×10^{-2} 2.8×10^{-2}	3-cont.	[77,78]
Al-Ta-Al (91:2:7 at %)	1×10^{16}	1200°C, 30mins	4.7×10^{-1}	3-cont.	[75]
$TaSi_2$/Al	1×10^{16}	1200°C, 30mins	2×10^{-1}	3-cont.	[75]

Table 2.5: Some ohmic contacts on p-type β-SiC. The layers in multi-layered contacts are separated with slashes, layers at the surface to the interface with SiC proceed from right to left [58].

CHAPTER 3

METHODOLOGIES

3.1 Atomic Force Microscope (AFM)

The atomic force microscope (AFM) is a high-resolution type of scanning probe microscope. The resolution of AFM can be fractions of a nanometer, which is more than 1000 times better than the optical diffraction limit. Because of the high resolution, the AFM is one of the most powerful tools for imaging, measuring and manipulating matter at the nanoscale.

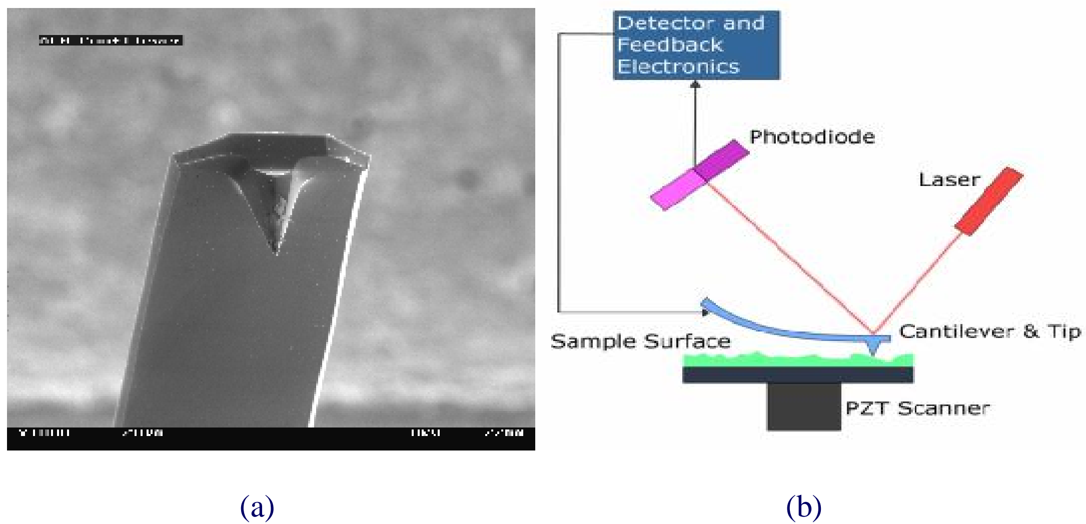

(a) (b)

Fig.3.1: (a) AFM cantilever in the Scanning Electron Microscope; (b) Block Diagram of Atomic Force Microscope [82].

As can be seen in Fig. 3.1, the AFM consists of a microscale cantilever with a sharp tip (probe) that is used to scan the specimen surface. Typically, the cantilever is made of silicon or silicon nitride, and the curvature of tip is in the order of nanometers. According to Hooke's law, the cantilever deflects due to forces between the tip and the sample when the tip is brought into proximity of a sample surface. Depending on the situation, forces that are measured in AFM include mechanical contact force, Van der Waals forces, capillary forces, chemical bonding, electrostatic forces, magnetic forces, Casimir forces, solvation forces, *etc.* [82]. Typically, the deflection is measured using a reflected laser beam from the top surface of the cantilever. Additional spectroscopic techniques such as scanning thermal microscopy, photothermal microspectroscopy have been developed through the use of specialized probes..

In order to avoid damage to the tip by the specimen surface, a feedback mechanism is employed to adjust the tip-to-sample distance to maintain a constant force between the tip and the sample. The tip is mounted on a vertical piezo scanner while the sample is being scanned in X and Y using another piezoelectric block. The resulting map of the area $s = f(x,y)$ represents the topography of the sample.

3.2 Collinear Four-point Probe Measurement

In a sheet resistance (R_{sh}) measurement, several parasitic resistances, including R_p, R_{cp} and R_{sp}, need to be considered as shown in Fig. 3.2 (a) [83]. R_p is the probe resistance which can be determined by shorting two probes and measuring their resistances. R_{cp} is a probe contact resistance at the interface between the probe tip and the semiconductor. R_{sp} is a spreading resistance when the current flows from the small tip and spreads out in the

semiconductor. Fig. 3.2 (b) shows the arrangement of the 4 probes for collinear four-point measurement.

Fig. 3.2 (c) shows the equivalent circuit for the measurement of R_{sh} by using the collinear four-point probe, where two probes carry the current and the other two probes sense the voltage. These parasitic resistances (R_p, R_{cp} and R_{sp}) can be neglected for the two voltage probes because the voltage is measured with a high impedance voltmeter which draws very little current. Thus the voltage drops across these parasitic resistances are insignificantly small. The voltage reading from the voltmeter is approximately equal to the voltage drop across the semiconductor sheet resistance.

By using the four-point probe method, the semiconductor sheet resistance can be calculated as [83]

$$IR_{sh} = FV \tag{3.1}$$

where V is the voltage reading from the voltmeter, I is the current carried by the two current carrying probes, and F is a correction factor.

For collinear or in-line probes with equal probe spacing, the correction factor F can be written as a product of three separate correction factors [83]

$$F = F_1 F_2 F_3 \tag{3.2}$$

F_1 corrects for finite sample thickness, F_2 corrects for finite lateral sample dimensions, and F_3 corrects for placement of the probes with finite distances from the sample edges.

For very thin samples with the probes being far from the sample edge, F_2 and F_3 are approximately equal to one (1.0), and the expression of the semiconductor sheet resistance becomes [83]

$$R_{sh} = \frac{p}{\ln 2}\frac{V}{I} \tag{3.3}$$

The four-point probe method can eliminate the effect introduced by the probe resistance R_p, probe contact resistance R_{cp} and spreading resistance R_{sp}. Therefore, this method is more accurate than the two point probe method.

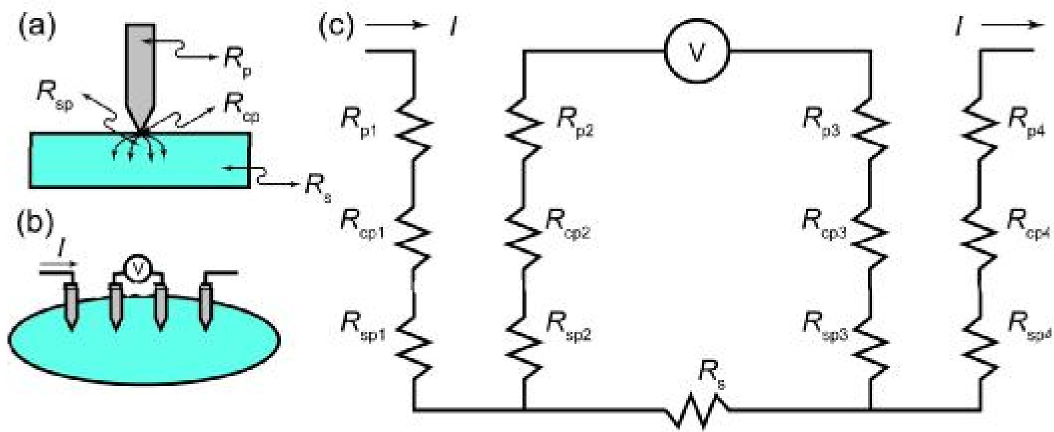

Fig.3.2: Four-point measurement of semiconductor sheet resistance. [84]

3.3 Van der Pauw Measurement and Hall Effect

The Van der Pauw Method is a commonly used technique to measure the sheet resistance (R_{sh}) of a material, which was first proposed by L.J. Van der Pauw in 1958 [85]. The resistivity (r) can be inferred from the measured sheet resistance for a sample of a given thickness (t): $r = {}^{R_{sh}}\!/_{t}$.

The Van der Pauw method is also often used to measure the Hall effect, which can be used to determine the type of semiconductor, majority carrier density and majority carrier mobility. The Hall effect setup typically consists of a current source, voltmeter, and a magnet. Since resistivity and Hall coefficient measurements at different temperature play an important part in research on semiconductors, Hall effect systems are usually attached to accurate cooling and heating systems in order to provide a range of temperatures.

3.3.1 Sample Preparation

First of all, four ohmic contacts need to be fabricated on the sample. The contacts must be on the boundary of the sample or as close to the boundaries as possible. Theoretically, the contact region must be infinitely small compared with the overall sample dimensions. Typically, $\frac{D}{L} < \frac{1}{10}$ is mandatory, where D is the diameter of the contact and L is the distance between the contacts. Secondly, the samples should be symmetrical, and their thickness must be less than the width and length of the sample. The surface of Hall sample should be smooth. Especially, there must be no isolated holes within the sample, which can change the current distribution in the sample. Lastly, contacts and leads from the contacts should be of the same material in order to minimize thermoelectic effects and keep the symmetry of the measurement. The most commonly used Hall patterns are shown in Fig. 3.3.

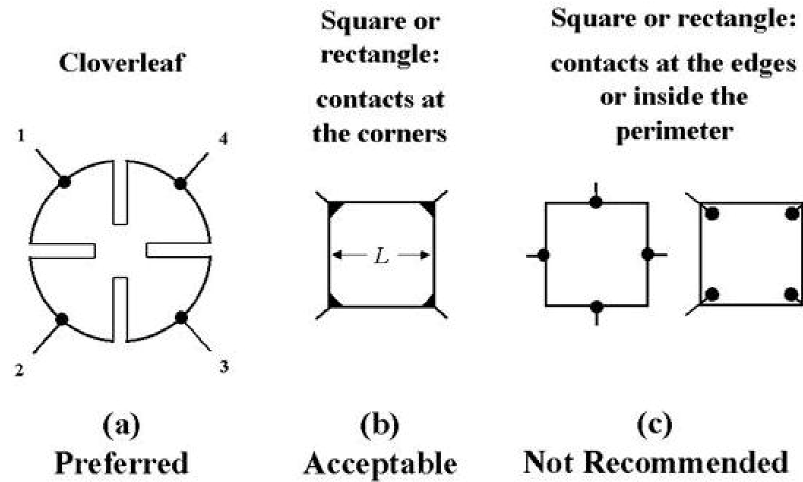

Fig.3.3: Some Van der Pauw sample patterns [86].

3.3.2 Resistivity Measurements

Basic Measurements

A current is injected along one edge of the sample (for instance, I_{12}) and the voltage across the opposite edge (in this case, V_{34}) is measured as shown in Fig.3.4. Based on these two values, a resistance (for this example, $R_{12,34}$) can be found by using Ohm's law:

$$R_{12,34} = \frac{V_{34}}{I_{12}} \tag{3.4}$$

Similarly, one can measure $R_{23,14}$. The sheet resistance of samples with arbitrary shape can be determined from these two resistances. The vertical resistance is the resistance measured along a vertical edge ($R_{12,34}$), and the horizontal resistance is the resistance measured along a horizontal edge ($R_{23,41}$). The actual sheet resistance R_s can be derived from the Van der Pauw formula [85]

$$e^{-pR_{12,34}/R_s} + e^{-pR_{23,41}/R_s} = 1 \tag{3.5}$$

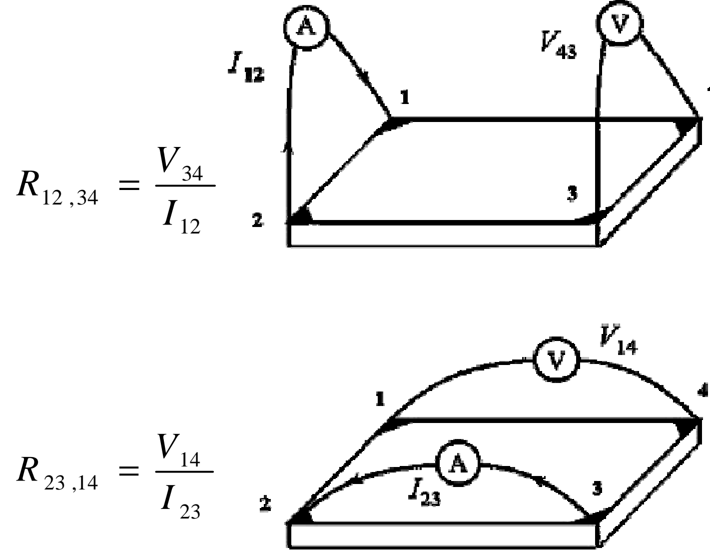

Fig.3.4: Schematic diagram of measuring $R_{12,34}$ and $R_{23,14}$ [85].

Reciprocal Measurements

In equation 3.5, one assumes that $R_{AB,CD} = R_{CD,AB}$ from the reciprocity theorem [85]. However in reality, $R_{AB,CD}$ is very often not equal to $R_{CD,AB}$ due to non-identical ohmic contacts. Therefore, one may obtain a more precise value for the resistances by averaging $R_{12,34}$ and $R_{23,41}$ with their reciprocal values $R_{34,12}$ and $R_{41,23}$.

Defining

$$R_{vertical} = \frac{R_{12,34} + R_{34,12}}{2} \tag{3.6}$$

and

$$R_{horizontal} = \frac{R_{23,41} + R_{41,23}}{2} \tag{3.7}$$

Using the above values in the Van der Pauw formula,

$$e^{-pR_{vertical}/R_s} + e^{-pR_{horizontal}/R_s} = 1 \tag{3.8}$$

Reversed Polarity Measurements

The accuracy of the resistance values can be further improved if the offset voltages such as thermoelectric potential due to the Seebeck effect can be eliminated from the values of $R_{vertical}$ and $R_{horizontal}$. In order to cancel out the offset voltage, one can repeat the resistance measurements after switching polarities of both the current source and the voltage meter. Then, the values of $R_{vertical}$ and $R_{horizontal}$ can be calculated as the averages of the standard and reversed polarity measurements. Now, one can have

$$R_{vertical} = \frac{R_{12,34} + R_{34,12} + R_{21,43} + R_{43,21}}{4} \tag{3.9}$$

and

$$R_{horizontal} = \frac{R_{23,41} + R_{41,23} + R_{32,14} + R_{14,32}}{4} \tag{3.10}$$

3.3.3 Hall Measurements

3.3.3.1 Introduction to Hall Effect

When a steady current is sourcing into a semiconductor sample as shown in Fig. 3.5, the velocity of the electrons is expressed as

$$u = \frac{I}{nAq} \tag{3.11}$$

where n is the electron density, A is the cross-sectional area of the sample and q is the elementary charge (1.602×10^{-19} coulombs).

If the semiconductor material is under an external magnetic field as shown in Fig. 3.5, then a Lorentz force will be exerted on the electrons due to the motion of electrons in magnetic field. The Lorenz force is

$$\vec{F}_L = q\vec{v} \times \vec{B} \tag{3.12}$$

where q is the charge on the particle in coulombs, v is the traveling velocity in magnetic field in the units of cm/s, and B is the strength of the magnetic field in the units of Wb/cm². Note that this force becomes strongest when the direction of motion is perpendicular to the direction of the magnetic field.

Assuming the magnetic field is perpendicular to the current flow, the resulting Lorenz force causes the electrons to move to one side of the semiconductor bar until it is balanced by the electrical force due to electrical field produced by the accumulated

electrons. Therefore, a potential difference known as Hall voltage V_H is built up across the semiconductor bar. Combining the above equations and noting that q is the charge on an electron, a formula for the *Lorentz* force experienced by the electrons can be obtained.

$$F_L = \frac{IB}{nA} \tag{3.13}$$

Since $F_L = Eq$ under equilibrium condition, one gets

$$E = \frac{IB}{qnA} \tag{3.14}$$

and

$$V_H = wE = \frac{WIB}{qnA} = \frac{IB}{qnd} = \frac{IB}{n_s q} \tag{3.15}$$

where d is the thickness of the material, n_s is sheet density, and the constant $1/nq$ is called Hall Coefficient R_H [87].

A Hall sample usually has a square configuration with an ohmic contact at each corner as shown in Fig. 3.3 (b). In order to measure the Hall voltage V_H, two sets of measurements need to be made: one with a magnetic field in the positive *z*-direction as shown in Fig. 3.6, and one with the field in the negative *z*-direction. For each set of measurements, reciprocal and reversed polarity measurements are performed to improve the accuracy of V_H. It should be noted that the voltages measured with a positive field will be indicated by a subscript P (for instance, $V_{13,\,P}$) and those with a negative field will

have a subscript N (such as $V_{13, N}$). For all of the measurements, the magnitudes of the injected current and magnetic field should be kept constant.

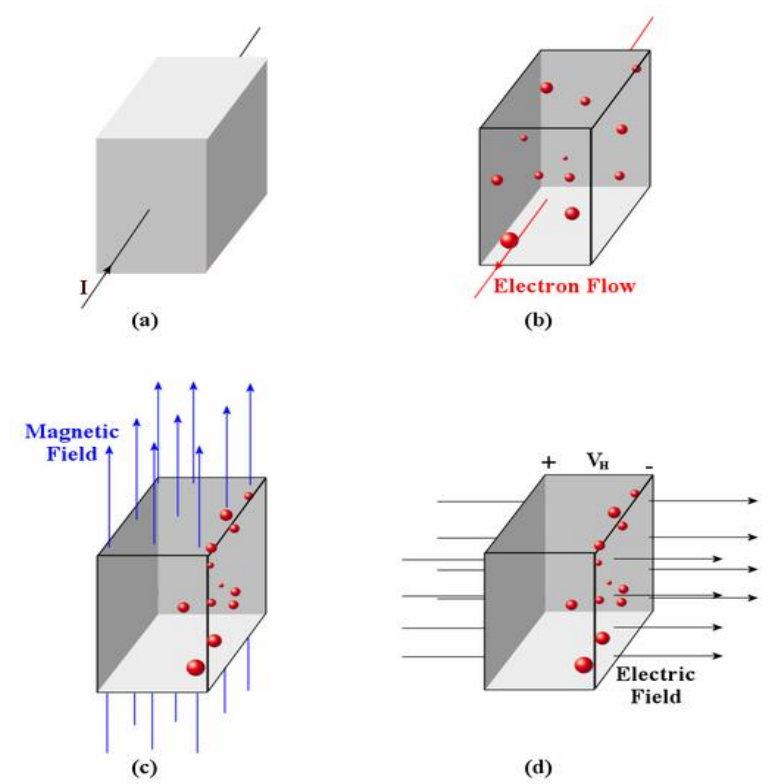

Fig.3.5 The Hall effect as it is used for the Van der Pauw method [88].
(a) a current flowing through a piece of semiconductor material.
(b) the electrons flowing due to the current.
(c) the electrons accumulating at one edge due to the magnetic field.
(d) the resulting electric field and Hall voltage V_H.

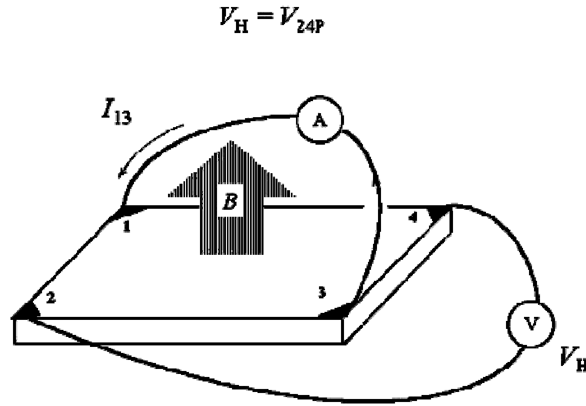

Fig. 3.6: The schematic diagram of Hall measurement [86].

3.3.3.2 Calculations

Hall Voltage

If the reciprocal and reversed polarity measurements are taken into account, the Hall voltage is given by

$$V_H = \frac{V_{13} + V_{24} + V_{31} + V_{42}}{8} \tag{3.16}$$

where

$$V_{13} = V_{13,P} - V_{13,N}$$

$$V_{31} = V_{31,P} - V_{31,N}$$

$$V_{24} = V_{24,P} - V_{24,N}$$

$$V_{42} = V_{42,P} - V_{42,N}$$

The polarity of this Hall voltage indicates the type of the semiconductor material. The material is p-type for $V_H > 0$ and n-type for $V_H < 0$. Finally, the sheet density is

$$n_s = \frac{IB}{q|V_H|} \tag{3.17}$$

where the strength of the magnetic field B is in units of Wb/cm².

Mobility

The resistivity of a semiconductor material can be shown to be [89]:

$$\rho = \frac{1}{q(n\mu_n + p\mu_p)} \tag{3.18}$$

where n and p are the concentration of electrons and holes, respectively, and μ_n and μ_p are the corrensponing carrier mobilities.

Since doping concentration in the doped epitaxial layer is higher than that in the substrate, usually many orders of magnitude higher, this equation can be simplified to

$$\rho = \frac{1}{qn_m\mu_m} \tag{3.19}$$

where n_m is the doping level and μ_m is mobility of the majority carriers.

Substituting $R_{sh} = \frac{\rho}{d}$ and $n_s = n_m d$ into equation (3.19) yields

$$R_{sh} = \frac{1}{q n_s \mathbf{m}_m} \tag{3.20}$$

By rearranging this equation, one can have the majority carrier mobility in terms of the previously calculated sheet resistance and sheet density

$$\mathbf{m}_m = \frac{1}{q n_s R_{sh}} \tag{3.21}$$

3.4 Linear Transmission Line Model

3.4.1 The Specific Contact Resistance

In the study of ohmic contacts to semiconductors, the greatest interest is in the specific contact resistance r_c (units of Ω.cm^2) rather than contact resistance R_c. Contact resistance is the total electrical resistance present at interface between the metal and semiconductor in an ohmic contact. Thus, it depends on the area or the geometry of the contact. However, specific contact resistance describes certain properties of the interface itself which influence the contact resistance R_c. Theoretically, the specific contact resistance is the interfacial property which is independent of the contact geometry. Contact resistance is equal to the specific contact resistance divided by contact area A or $R_c = \frac{r_c}{A}$, assuming the entire contact area takes part in the conduction process. Since the specific contact resistance is related to the current density J (units of A/cm^2), it is also given as [30]

$$r_c = \lim_{V \to 0} \left(\frac{dJ}{dV} \right)^{-1} \tag{3.22}$$

3.4.2 The Linear Transmission Line Model

The linear transmission line model (LTLM) is often used to investigate the specific contact resistance (r_c) of the ohmic contacts on semiconductors. The specific contact resistance can be inferred from the sheet resistance (R_{sh}) of the semiconductor and contact resistance (R_c). As shown in Fig. 3.7, the total resistance (R_T) between two adjacent contact pads is a function of the inter-pad spacing L. From the plot of R_T versus L, R_c can be estimated from y-intercept and R_{sh} can be derived from the slope of the plot.

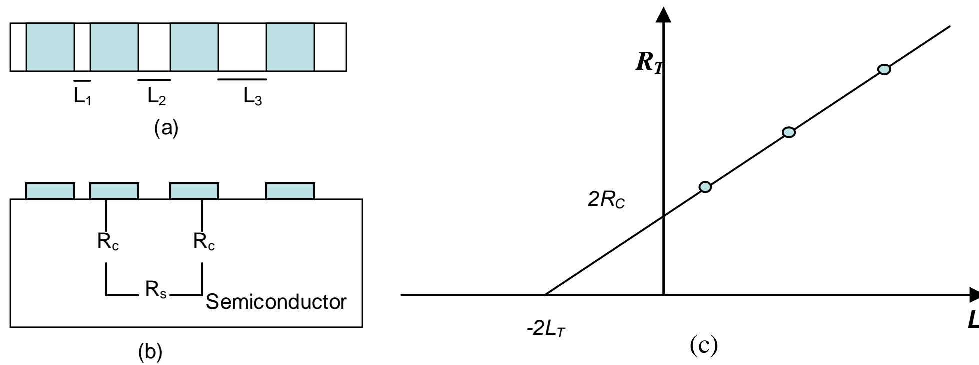

Fig. 3.7: The block diagrams of TLM pattern: (a) top view and (b) cross-sectional view; (c) R_T versus L plot. [90]

The total resistance between any two adjacent pads is

$$R_T = 2R_c + R_s \tag{3.23}$$

where R_c is the contact resistance, R_s is the resistance from the semiconductor between two pads. Since

$$R_s = R_{sh} \frac{L}{W} \tag{3.24}$$

where W is the width of the pads.

Therefore,

$$R_T = 2R_c + R_{sh} \frac{L}{W} \tag{3.25}$$

The contact between a metal and a semiconductor layer can be described with the resistive network shown in Fig. 3.8. This equivalent circuit is obtained by slicing the structure into small sections with length Δx, so that the contact resistance, R_1, and the semiconductor resistance, R_2, are given by [91]

$$R_1 = \frac{r_c}{W \Delta x} \quad \text{and} \quad R_2 = R_{sk} \frac{\Delta x}{W} \tag{3.26}$$

where r_c is the specific contact resistance, and R_{sk} is the modified sheet resistance of the semiconductor under the contact with units of Ω/□ (ohms/square).

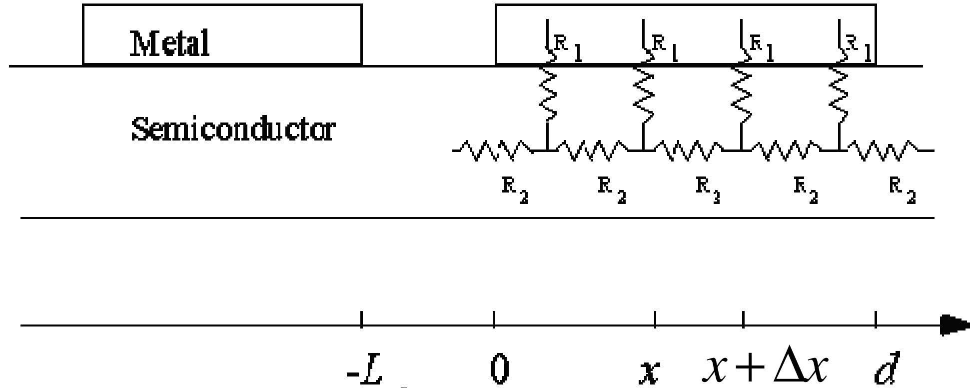

Fig.3.8: The equivalent resistive network of ohmic contact. [91]

Applying *Kirchoff's* laws, the following relations can be obtained

$$V(x+\Delta x)-V(x)=I(x)R_2=I(x)\frac{R_{sk}}{W}\Delta x \tag{3.27}$$

$$I(x+\Delta x)-I(x)=\frac{V(x)}{R_1}=V(x)\frac{W}{r_c}\Delta x \tag{3.28}$$

where $V(x)$ is the voltage across the M-S interface, and $I(x)$ is the current parallel to the interface at x and $x+\Delta x$.

In the limit $\Delta x \rightarrow 0$,

$$\frac{dV}{dx}=\frac{I(x)R_{sk}}{W} \tag{3.29}$$

and

$$\frac{dI}{dx}=\frac{V(x)W}{r_c} \tag{3.30}$$

Combining the two equations

$$\frac{d^2 I(x)}{d^2 x} = \frac{W}{r_c}\frac{dV}{dx} = I(x)\frac{R_{sk}}{r_c} = \frac{I(x)}{L_T} \tag{3.31}$$

where $$L_T = \sqrt{\frac{r_c}{R_{sk}}}$$

The parameter L_T is the so-called 'transfer length' which is the characteristic distance over which the current changes under the metal contact. The general solution for $I(x)$ and $V(x)$ are:

$$I(x) = I_0 \frac{\sinh \frac{d-x}{L_T}}{\sinh \frac{d}{L_T}} \tag{3.32}$$

$$V(x) = I_0 \frac{L_T R_{sk}}{W} \frac{\cosh \frac{d-x}{L_T}}{\sinh \frac{d}{L_T}} \tag{3.33}$$

where d is the length of the contact pad.

The contact resistance is

$$R_c = \frac{V(0)}{I(0)} = \frac{L_T R_{sk}}{W} \coth \frac{d}{L_T} = \frac{\sqrt{r_c R_{sk}}}{W} \coth \frac{d}{L_T} \tag{3.34}$$

In the limit of $d \to \infty \, (d >> L_T)$,

$$R_c = \frac{\sqrt{r_c R_{sk}}}{W} \tag{3.35}$$

In addition, one can assume $R_{sh} \approx R_{sk}$ if the sheet resistance of the semiconductor beneath the contacts is not significantly modified. Thus, the total resistance between any two adjacent contact pads is given by:

$$R_T = 2\frac{\sqrt{r_c R_{sh}}}{W} + R_{sh}\frac{L}{W} \tag{3.36}$$

As can be seen in this equation, R_T is a linear function of L. Therefore, the measured total resistance from a TLM structure can be fitted to a straight line shown in Fig.3.7 (c). L_T can be obtained from the y-axis intercept; R_{sh} can be obtained from slope, and r_c can be derived from the y-axis interception.

In the case of $R_{sk} \neq R_{sh}$, the contact end resistance (R_E) has to be measured in order to get the correct specific contact resistance r_c [90]. R_E is given by [92]

$$R_E = \frac{V}{I} = \frac{\sqrt{R_{sk} r_c}}{W} \frac{1}{\sinh(\frac{d}{L_T})} \tag{3.37}$$

where I is the constant current between two adjacent pads and V is the potential difference between one of the two current pads and the third adjacent pad.

Substituting $R_{sk} = \frac{r_c}{{L_T}^2}$ into the equation,

$$R_E = \frac{r_c}{L_T W} \frac{1}{\sinh(\frac{d}{L_T})} \quad \text{and} \quad \frac{R_c}{R_E} = \cosh(\frac{d}{L_T}) \tag{3.38}$$

CHAPTER 4

EXPERIMENTAL METHODS

4.1 Standard Procedures for Device Fabrication

The (0001) 4H-SiC used in this research was purchased from Cree, Inc. The original 2 inch wafers were diced into 5mm×5mm and 1cm×1cm pieces, which are used for LTLM and Hall measurements, respectively. The doping concentration of the epitaxial layer for both n- and p-type as purchased material was in the range of 10^{15} to 10^{16} cm^{-3}, which is more than 100 times smaller than the implant concentrations that were used.

4.1.1 The Standard Sample Cleaning Process

Samples were cleaned using both organic and Radio Corporation of America (RCA) cleaning processes. Organic cleaning is used to degrease the samples, and the RCA cleaning removes ionic and heavy metallic impurities.

Organic Clean:

- Immerse in acetone and agitated in an ultrasonic bath for 5 minutes.
- Immerse in trichloroethylene (TCE) and agitated in an ultrasonic bath for 5 minutes.

- Immerse in acetone and agitated in an ultrasonic bath for 5 minutes.
- Immerse in methanol and agitated in an ultrasonic bath for 5 minutes.
- Immerse in fresh methanol and agitated in an ultrasonic bath for 5 minutes.
- Rinse in de-ionized water (DI water) for 5 minutes.
- Immerse in buffer oxide etch (BOE) for 4 minutes.
- Rinse in DI water for 2 minutes and dried with N_2 gas.

RCA Clean:

- Immerse in a 1:1 solution of H_2O_2:H_2SO_4 for 15 minutes.
- Rinse in DI water for 2 minutes.
- Immerse in BOE for 1 minute.
- Rinse in DI water for 2 minutes.
- Immerse in a boiling 5:1.5:1.5 solution of DI- H_2O: H_2O_2: NH_4OH heated gently on hot plate for 15 minutes.
- Rinse in DI water for 2 minutes.
- Immerse in BOE for 1 minute.
- Rinse in DI water for 2 minutes.
- Immerse in a boiling 5:1.5:1.5 solution of DI- H_2O: H_2O_2: HCl heated gently on hot plate for 15 minutes.
- Rinse in DI water for 2 minutes.
- Immerse in BOE for 1 minute.
- Rinse in DI water for 2 minutes and dried with N_2 gas.

4.1.2 Sample Oxidation

An oxide layer is grown on SiC by using a high temperature furnace with a maximum temperature 1200°C shown in Fig. 4.1. The temperature of the furnace is kept at 800°C, and the furnace tube is filled with Ar gas when the furnace is not in use. The oxidation tube is made of high purity quartz (GE 224) with a cap at the right end. A high purity quartz paddle is used to load the samples, which can slide into the tube. A few ports at the right end of the tube for flowing gases, including O_2, NO, Ar and H_2, into the tube are connected to a gas controller. The gas flowing into the tube is exhausted from the port at the left end of the tube. The oxide growth rate is about 6nm/hour with 1atm of pure O_2 at 1150°C flowing at 500 sccm.

Oxidation Procedure:

- Open the cap at the right end of the tube.
- Pull the sample paddle out slowly and gently.
- Load the samples on the paddle with face up.
- Slide the paddle into the tube slowly and gently, and position the samples at the center of the hot zone of the furnace.
- Put the cap back on and screw it tightly.
- Open Ar valves, and flow Ar into the tube with the flowing rate 500sccm.
- Increase the temperature to 1150°C with a ramping rate 5°C /min.
- Close Ar valves and open O_2 valves when the temperature is stabilized at 1150°C. Then, start counting the oxidation time.

- Close O_2 valves and open Ar valves when the oxidation is finished. Then, decrease the temperature to 800°C with a decreasing rate 20°C /min..
- Open the cap and pull out the paddle slowly and gently.
- Remove samples from the paddle.
- Push the paddle back into the tube and close the cap.
- Stop Ar flowing and close the Ar valves.

Fig. 4.1: Oxidation furnace.

4.1.3 Sample Implantation

In order to make ohmic contacts, the samples are implanted at 700°C using the Auburn University 6SDH-2 Pelletron tandem accelerator shown in Fig. 4.2. The accelerator provides ions from two ion sources with a wide energy range from 100 keV to

12 MeV. Helium ion beams are produced from an rf exchange ion source. Heavier ions, such as nitrogen, aluminum, silicon, phosphorous and gold, are available from the SNICS II (Source of Negative Ions by Cesium Sputtering). The accelerator is used for Rutherford backscattering spectroscopy (RBS), light ion channeling (LIC), nuclear reaction analysis (NRA) and heavy ion implantation (HII).

Before implantation is performed, a sacrificial oxide layer (~30 nm) is grown on all the samples. On top of the oxide, A layer of molybdenum is then sputter-deposited over the oxide. Since nitrogen ions of the same energy travel further than aluminum ions into the SiC, the thicknesses of the Mo layers are different; 150 nm for nitrogen implantation and 100nm for aluminum implantation. After the implantation, H_2O_2 is used to remove the Mo layer, and BOE is used to remove the oxide layer. Finally, both organic and RCA cleaning are performed to the samples before further processing.

The additional layers of material serve a twofold purpose, first to bring the implant profile to the surface of the SiC and second to prevent the Mo from being driven by the high energy ions into the SiC.

Nitrogen implantation is performed to p-type substrates, whereas Al is implanted into n-type substrates. Thus, a PN junction forms at the interface between the implantation layer and the remaining epitaxial layer. This junction prevents injected current from getting into the substrate bulk when electrical measurements are made. The thickness of the implantation layer is around 550 nm with the implantation energies of 170, 250, 350, 450 and 600 keV. The implantation doses depend on the desired doping concentration. The implantation box profiles for both N- and Al-implantation shown in

Fig. 4.3 are simulated with the above five implantation energies using software ‘SRIM’ [48]. The profiles of implanted samples and their uses are listed in Table 1.

Fig. 4.2: Pelletron tandem accelerator used for implantation.

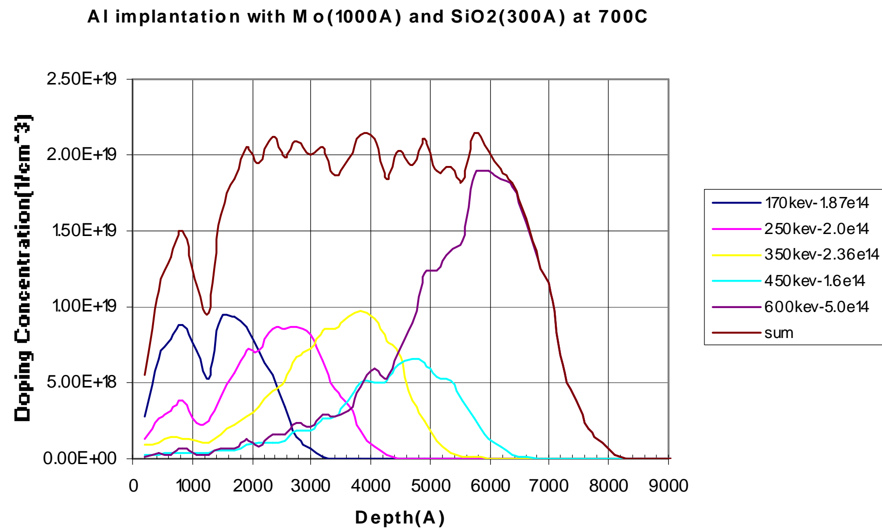

(a)

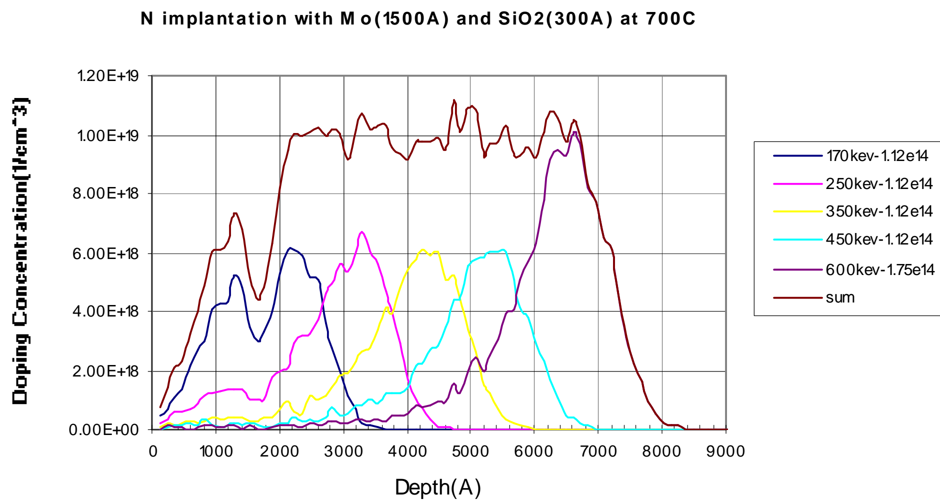

(b)

Fig. 4.3: Two examples of the simulated implantation box profiles: (a) The simulated Al implantation box profile for doping concentration $2\times10^{19}cm^{-3}$; (b) The simulated N implantation box profile for doping concentration $1\times10^{19}cm^{-3}$.

Implanted (001) 4H-SiC profile (cm^{-3})	Activation Temperature (^{o}C)	Purpose
P sub/0.6 μm N-impl. (1×10^{18})	1550	TLM & Hall
P sub/0.6 μm N-impl. (4×10^{18})	1550	TLM & Hall
P sub/0.6 μm N-impl. (5×10^{18})	1350, 1450, 1550, 1650	TLM
P sub/0.6 μm N-impl. (1×10^{19})	1550	TLM & Hall
P sub/0.6 μm N-impl. (4×10^{19})	1550	TLM & Hall
P sub/0.6 μm N-impl. (1×10^{20})	1350, 1450, 1550, 1650	TLM
N sub/0.6 μm Al-impl. (2×10^{18})	1650	TLM & Hall
N sub/0.6 μm Al-impl. (5×10^{18})	1400, 1500, 1600, 1700	TLM
N sub/0.6 μm Al-impl. (8×10^{18})	1650	TLM & Hall
N sub/0.6 μm Al-impl. (2×10^{19})	1650	TLM & Hall
N sub/0.6 μm Al-impl. (8×10^{19})	1650	TLM & Hall
N sub/0.6 μm Al-impl. (1×10^{20})	1400, 1500, 1600, 1700	TLM
N sub/0.6 μm Al-impl. (2×10^{20})	1650	TLM & Hall

Table 4.1: The implanted profile and purpose of 4H-SiC samples

4.1.4 Optical Photolithography

Photolithography is a process which is often used in micro-fabrication. The main purpose of photolithography is to transfer a geometric pattern from a photo-mask to a sample. Some fundamental principles of photography are also applied in photolithography. With a thin film of light-sensitive chemical photoresist on top of the substrate, the pattern is created by exposing it to light through an optical mask. This process affords exact control over the shape and size of the patterns with ultra high resolution. In addition, the patterns can be created over the entire surface simultaneously. The main disadvantages of photolithography are the following: it requires a flat substrate;

it is not very effective at creating shapes that are not flat; and the process requires extremely clean operating conditions.

A Karl Suss MJB3 UV400 mask aligner shown in Fig. 4.4 is used to make both TLM and Hall Effect patterns. This manually controlled mask aligner is equipped with an optical microscope having magnifications of 5, 10 and 20, and a UV light source having an output power of 160W. The resolution of the mask aligner is 2-3 um.

Fig. 4.4: Karl Suss MJB3 UV400 mask aligner equipped with an optical microscope.

The sample is held at the center of a 3in silicon wafer. The whole wafer is then covered with photo-resist by spin coating for 30s at a rotor speed of 4000 rmp. Fig. 4.5 shows the photoresist spinner. The resulting thickness of photoresist on the sample is around 1.5 um. The photoresist-coated wafer is soft-baked for 30s at 90°C on a hot plate, which will dry the photoresist and make it more sensitive to UV light. Overbaking or

underbaking should be avoided since this harms the response sensitivity of the photoresist. Baking causes a cross linking reaction for the photoresist, allowing it to be removed by development.

Fig. 4.5: Photoresist Spinner.

After soft-baking, the wafer is mounted to the mask aligner and brought into alignment by adjusting the X, Y and θ positions of the sample holder. The sample is then exposed to UV light for 30s, then hard-baked for 1min at 100°C on a hot plate, followed by the second UV exposure for 1min without photo-mask. Fig. 4.6 shows both the TLM and Hall masks used in this work.

The last step in the photolithographic process is development. Samples are developed in a mixture of DI water and chemical developer with a volume ratio of 3:1. The samples are immersed in the mixture for 10-15s, and then rinsed in DI water for 1 minute. As can be seen under microscope, the photoresist on the area where the UV light

is blocked by the mask during the first time exposure is washed away. If the edge of the pattern is not sharp enough, the sample can be developed for a few more seconds.

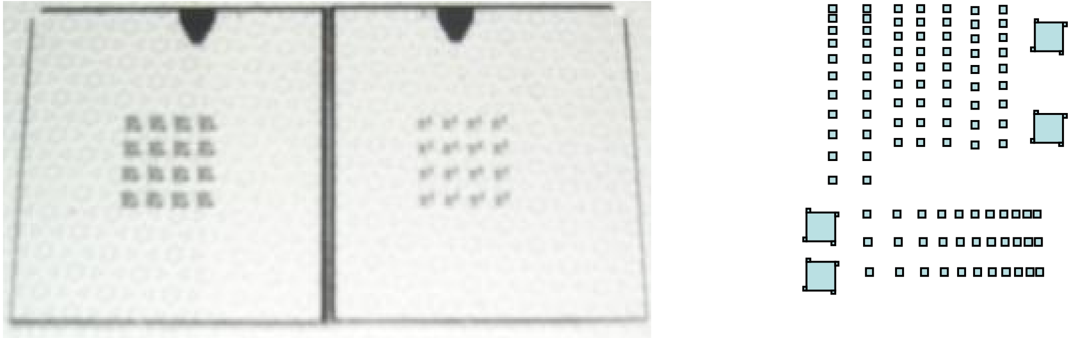

(a)

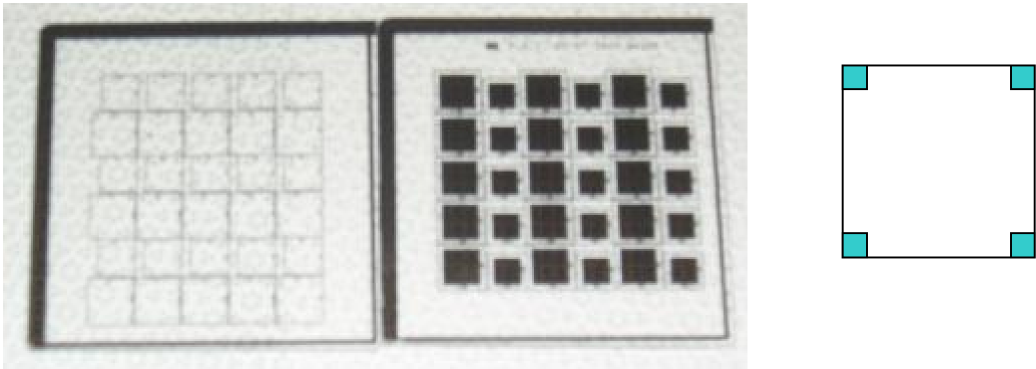

(b)

Fig. 4.6: (a) LTLM masks with an enlarged TLM pattern; (b) Hall Effect masks with an enlarged Hall pattern.

4.1.5 Metal Sputter-deposition

Metals are sputter-deposited on SiC substrates in an Ar plasma environment. The sputter system shown in Fig.4.7 (a) has a turbo pump, which achieves a high vacuum to 10^{-8} Torr. Four 2in diameter magnetron sputtering guns shown in Fig.4.7 (b) are located in the vacuum chamber, water-cooled with 13°C water circuiting beneath the cathode surface. Four different targets can be sputtered consecutively without breaking vacuum in

(a)

(b)

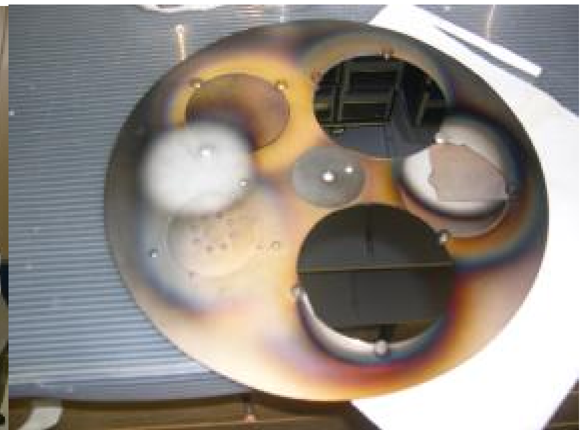

(c)

Fig. 4.7: (a) Overall sputter-deposition system; (b) Vacuum chamber of Sputter-deposition system; (c) Sample holder disc.

this system. The sputter targets, with a cathode potential range of 200-1500V, can operate at a maximum dc power of 1000W. The metals or metallic alloys to be sputtered are mounted on the magnetrons, and cylindrical glass chimneys are then placed on the guns to confine and focus the sputtered materials. Samples held on 3in Si wafers are screwed on a plain disk carrier shown in Fig.4.7 (c) that can be rotated during sputter-deposition. It takes roughly 2 hours to pump the chamber down to 5×10^{-7} Torr which is the standard pressure for sputter-deposition. The sputtering rate depends on the type, quality and thickness of the target materials. Calibration of the sputtering rate should be done from time to time even for the same target. In this work, a Tencor profilometer shown in Fig. 4.8 (a) is used to measure the thickness of the deposited thin film. Large area, uniform films can be obtained since the sample is 4in away from the target. Fig.4.8 (b) shows the sample holder of the Tencor profilometer.

Before starting sputter-deposition, chamber pressure and cooling water circulation to the guns should be checked. Argon gas flow is set at 106.4 sccm on an MKS 247 mass flow controller for most of the deposition in this work. At this flow rate, the chamber pressure rises to 20 mTorr with a butterfly valve to restrict the pumping speed of the turbo-pump. The power supply for the sputtering gun is turned on after the pump power is stabilized at around 225W. The dc voltage to the cathode is then increased until an Ar plasma is generated and the predetermined sputter current is attained and stabilized. In order to remove the impurities on the target surface, an off-sample pre-sputtering is carried out for few minutes before the sample is rotated to a position right above the

sputter-gun. The sputtering time is determined by the sputtering rate and the desired metal film thickness.

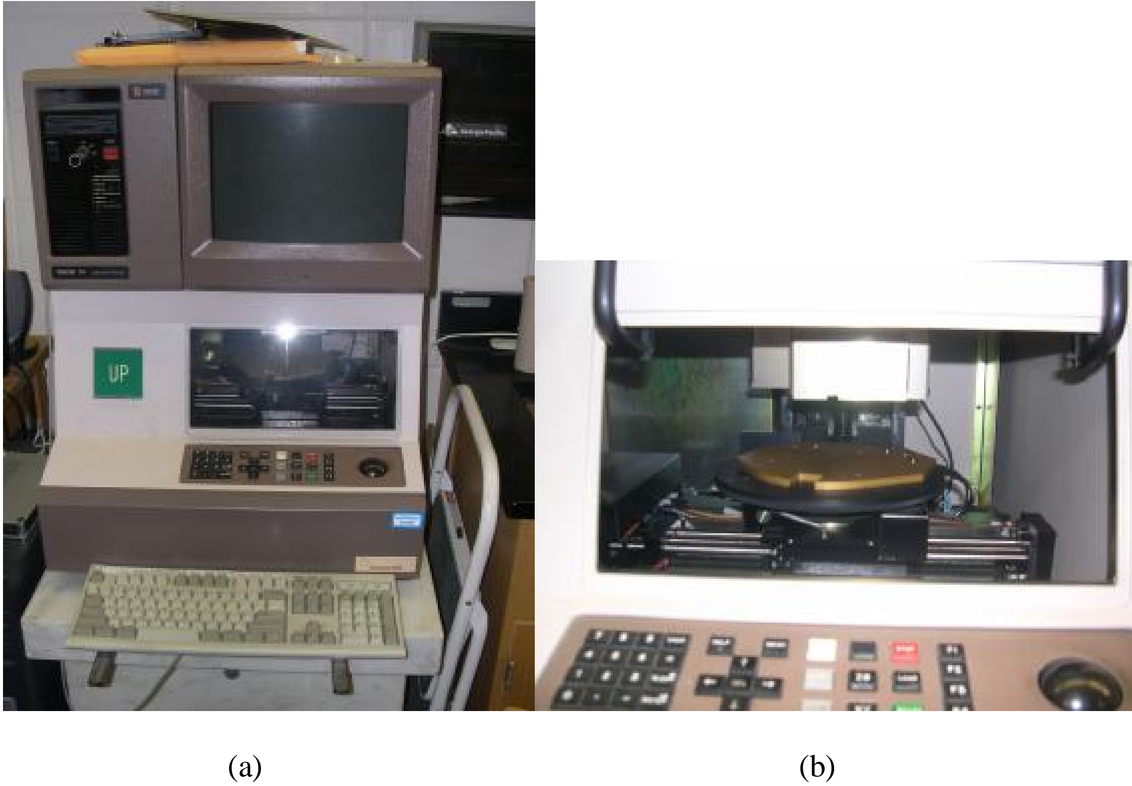

(a) (b)

Fig. 4.8: (a) Tencor profilometer; (b) Sample holder.

4.1.6 Sample Activation and Contact Anneal

The annealing system shown in Fig. 4.9 (a) for this study can be used for both Ohmic contact and high temperature implant activation anneals. The heating elements in this system are two thin carbon strips separated by 2in in vertical distance as shown in Fig. 4.9 (b). The input voltage and the current through the carbon strips can be manually adjusted using a variac. A thermocouple is used to monitor the temperature when the sample is heated in a carbon box in an Ar or nitrogen environment, while a pyrometer is

used to measure the temperature when the sample is located directly on the heating carbon strip. A stable temperature up to 1700°C can be achieved with this system. The annealing system can be pumped down to 2×10^{-7} Torr in 2 hours.

In this study, N- and Al-implanted samples are activated at different temperatures shown in Table 4.1. Hall samples are activated at 1550°C for n-type and 1650°C for p-type. TLM samples for investigating the relationship between specific contact resistance and implant concentration are activated at 1550°C for n-type and 1650°C for p-type, whereas, samples for studying specific contact resistance as a function of activation anneal temperature are activated at 1350/1450/1550/1650/1750°C for n-type and 1400/1500/1600/1700/1800°C for p-type. All samples are activated with carbon cap for 30 min in an Ar environment. The purpose of the carbon cap on top of the implanted surface is to protect the surface during high temperature activation. The sample is coated with a thin layer (~500 um) of photoresist and placed in the carbon box shown in Fig. 4.9 (c) with its coated face up. The carbon box is then put between the two carbon strips and surrounded with an insulating carbon foam box. The thermocouple is positioned near the edge of the carbon box through a hole on the carbon foam. After the chamber is pumped down to a vacuum of about 2×10^{-7} Torr, the pump is turned off, and Ar gas is flowed into the chamber at 1500 sccm. Power is turned on and the current through the carbon strips is increased slowly. The carbon cap temperature (600°C) is reached in 2-3 min with a variac setting of 25-28%. The sample is kept at this temperature for 30 min in order to form the protective carbon cap.

After carbon cap is formed, the sample is turned over with its face down, and the carbon box is closed with its lid. To activate N-implanted samples at 1550°C, the power variac is set at 53-56%. To activate Al-implanted samples at 1650°C, the power variac is set at 61-63%. The samples are taken out from the chamber when the temperature is below 100°C.

NiV7% contacts are annealed at 1000°C for 1 min in vacuum (~2×10^{-7} Torr) with samples clamped directly on the heating carbon strip shown in Fig. 4.9 (b). In 20-30s, the temperature will be 450°C with the variac setting of 25%, where the temperature is monitored by a pyrometer on top the chamber shown in Fig. 4.9 (a). The variac setting is increased to 42% and in another 20-30s, the anneal temperature of 1000°C is reached. Following the same procedure, Al70Ti30 contacts are annealed at 1100°C for 1 min under vacuum (~2×10^{-7} Torr) with a variac setting of 46%.

4.1.7 Reactive Ion Etching (RIE)

The RIE system shown in Fig. 4.10 (a) is used to define both the Hall patterns and TLM strips in this work. The sample is held on a 2in silicon wafer, and the wafer is then put on the cathode in the vacuum chamber Fig. 4.10 (b). The base pressure in the chamber is 9-12 mTorr. The working pressure with plasma is 34-38 mTorr when flowing NF_3 gas at 9 sccm. The etching rate is 90 nm/min for 4H-SiC with forward power of 18W and reflected power of 2W. Nitrogen gas is used to open the chamber. The etching mechanisms are [4]

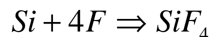

$$Si + 4F \Rightarrow SiF_4$$

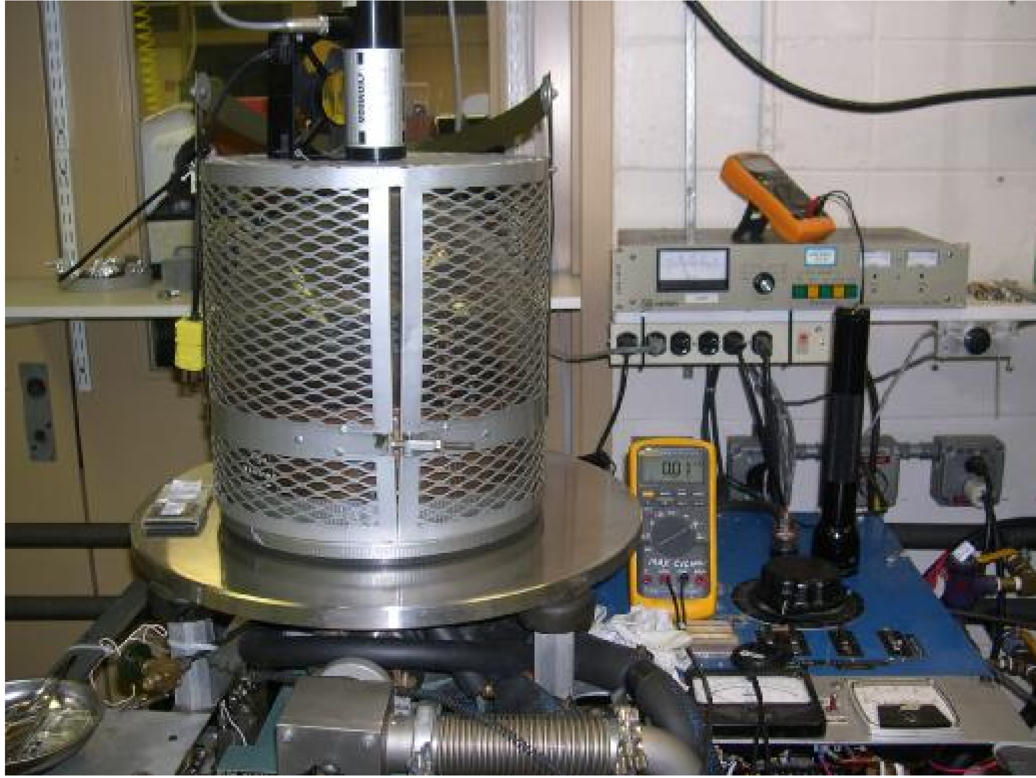

(a)

(b) (c)

Fig. 4.9: (a) Overall view of annealing system; (b) Heating carbon strip with sample clipped on; (c) Carbon box for carbon cap and activation anneal.

where SiF_4 is in gaseous form, and

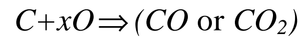

$$C + xO \Rightarrow (CO \text{ or } CO_2)$$

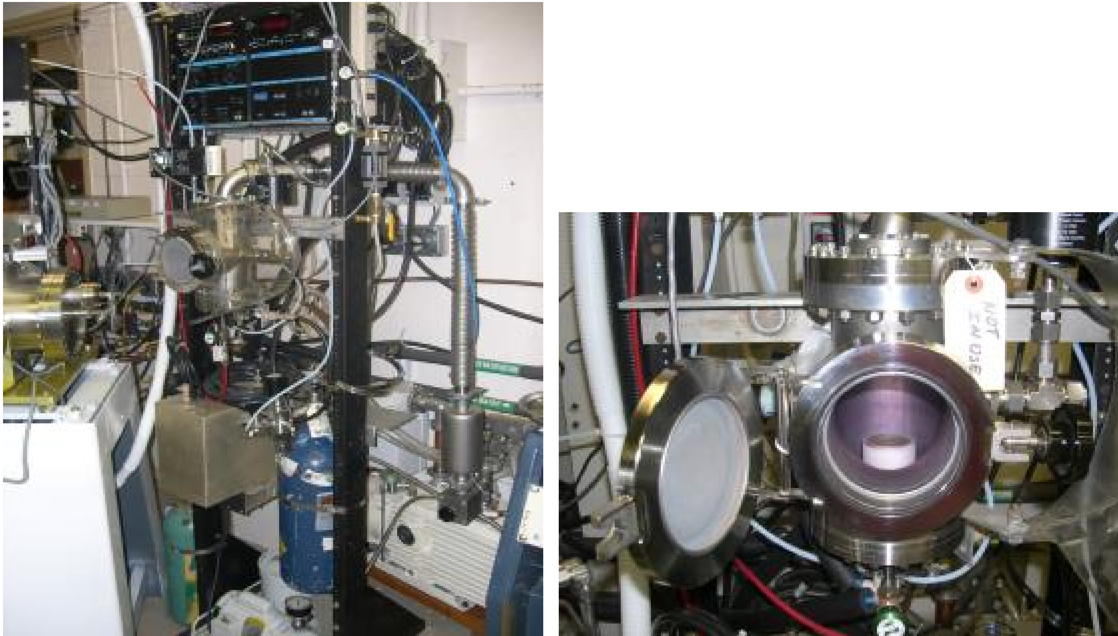

(a) (b)

Fig. 4.10: (a) Overall view of RIE system; (b) Vacuum chamber of RIE system with a cathode inside.

4.1.8 Sample Wire-bonding

A method used to attach a fine wire from one connection pad to another, completing the electrical connection in an electronic device, is called wire bonding. All the Hall samples fabricated in this study were wire-bonded by using a manual gold wire bonder shown in Fig. 4.11 in the department of Electrical and Computer Engineering.

This manual wire bonder is equipped with an optical microscope having a magnification up to 40 and a sample holder that can be heated to 800°C. The diameter of Au wire is 30um. The bonding technique is Au ball-wedge at a temperature 300°C.

Fig. 4.11: The manual ball-wedge wire bonder.

4.2 Device Fabrication and Measurements

4.2.1 Hall Sample

Hall samples are fabricated for both N- and Al-implanted samples. The implanted doping concentrations are 1×10^{18}, 4×10^{18}, 1×10^{19}, 4×10^{19}, 1×10^{20} cm^{-3} for N implanted samples, and 2×10^{18}, 8×10^{18}, 2×10^{19}, 8×10^{19}, 2×10^{20} cm^{-3} for Al implanted samples. The implantation box profiles for these samples are listed in Table 4.1. The alloy NiV7% was

used for contacts to N-implanted samples with an anneal at 1100°C for 1 min at 10^{-7} Torr. The alloy Al70%Ti30% was used for Al-implanted samples with an anneal at 1000°C for 1 min at 10^{-7} Torr. A gold layer (180nm) is then deposited on top of the ohmic contact. The size of Hall sample is 0.6cm×0.6cm with the contact size 200um×200um. The Hall sample is formed by mesa etching on a 1cm×1cm implanted SiC piece. The sequence for Hall sample fabrication is shown in Fig. 4.12, and schematic views of a Hall sample are shown in Fig. 4.13.

4.2.2 Ohmic Conact Fabrication for LTLM

Ohmic contacts were fabricated on both N- and Al-implanted 4H-SiC. TLM patterns are made by photolithography using TLM masks shown in Fig. 4.4 (a). The alloy NiV7% is used for contacts to N-implanted samples with an anneal at 1100°C for 1 min at 10^{-7} Torr. The alloy Al70%Ti30% is used for Al-implanted samples with an anneal at 1000°C for 1 min at 10^{-7} Torr. A gold layer (60 nm) is then deposited on top of the ohmic contact. The sequence for ohmic contact fabrication is shown in Fig. 4.14.

4.2.3 TLM Measurement

The set-up for TLM measurements shown in Fig. 4.15 (a) includes a microscope, four probes (two for sourcing current and two for voltage measurement), a Keithley 220 programmable current source and a Hewlett Packard 3478A multimeter. Fig. 4.15 (b) shows the equivalent circuit for the TLM measurement. The measurements are performed by passing a 1 mA current between two adjacent TLM pads using the current source. The resultant potential difference between these two pads is then measured by the multi-

meter. The total contact-to-contact resistance can be derived by using Ohm's law. Assuming all the ohmic contacts are identical, the total resistance between adjacent pads is plotted as a function of inter-contact spacing. The contact resistance, semiconductor sheet resistance and specific contact resistance are then obtained from the TLM analysis discussed in Section 3.4.

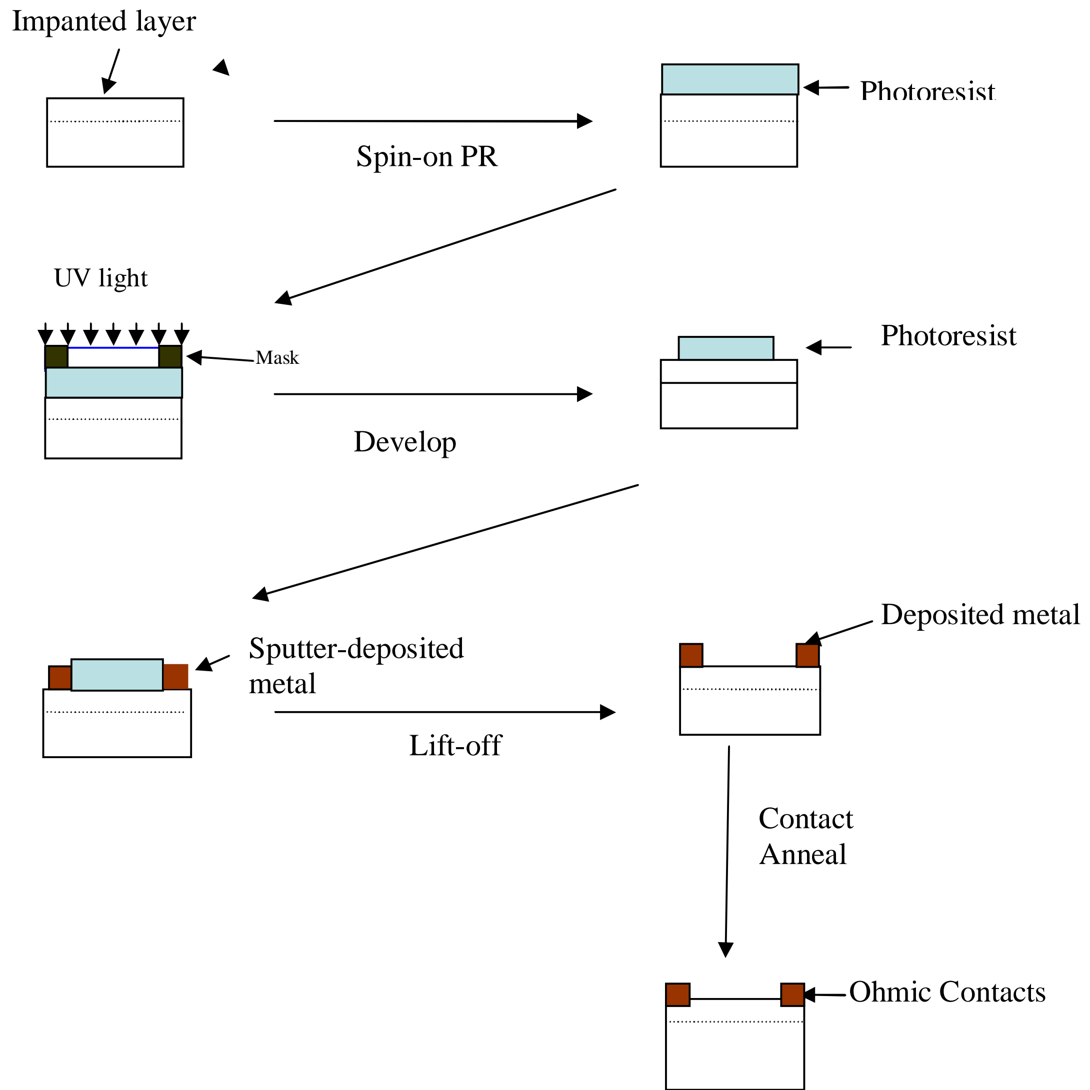

Fig. 4.12: The sequence of events for Hall sample fabrication.

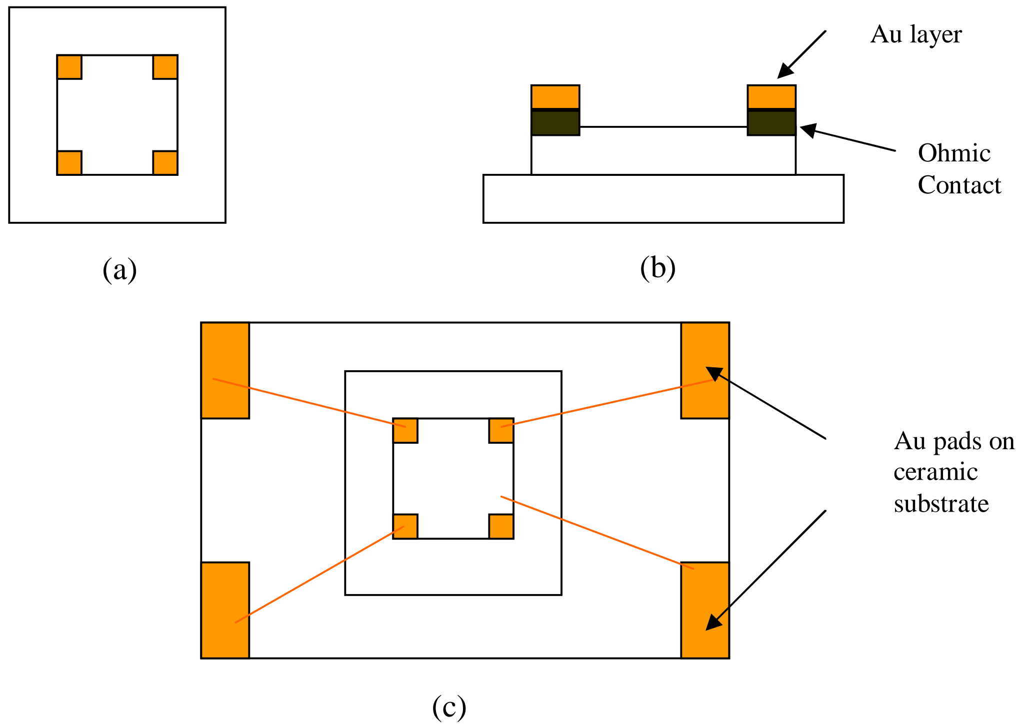

Fig. 4.13: (a) Top view of Hall sample; (b) Cross-sectional view of Hall sample; (c) Wire-bonded Hall sample.

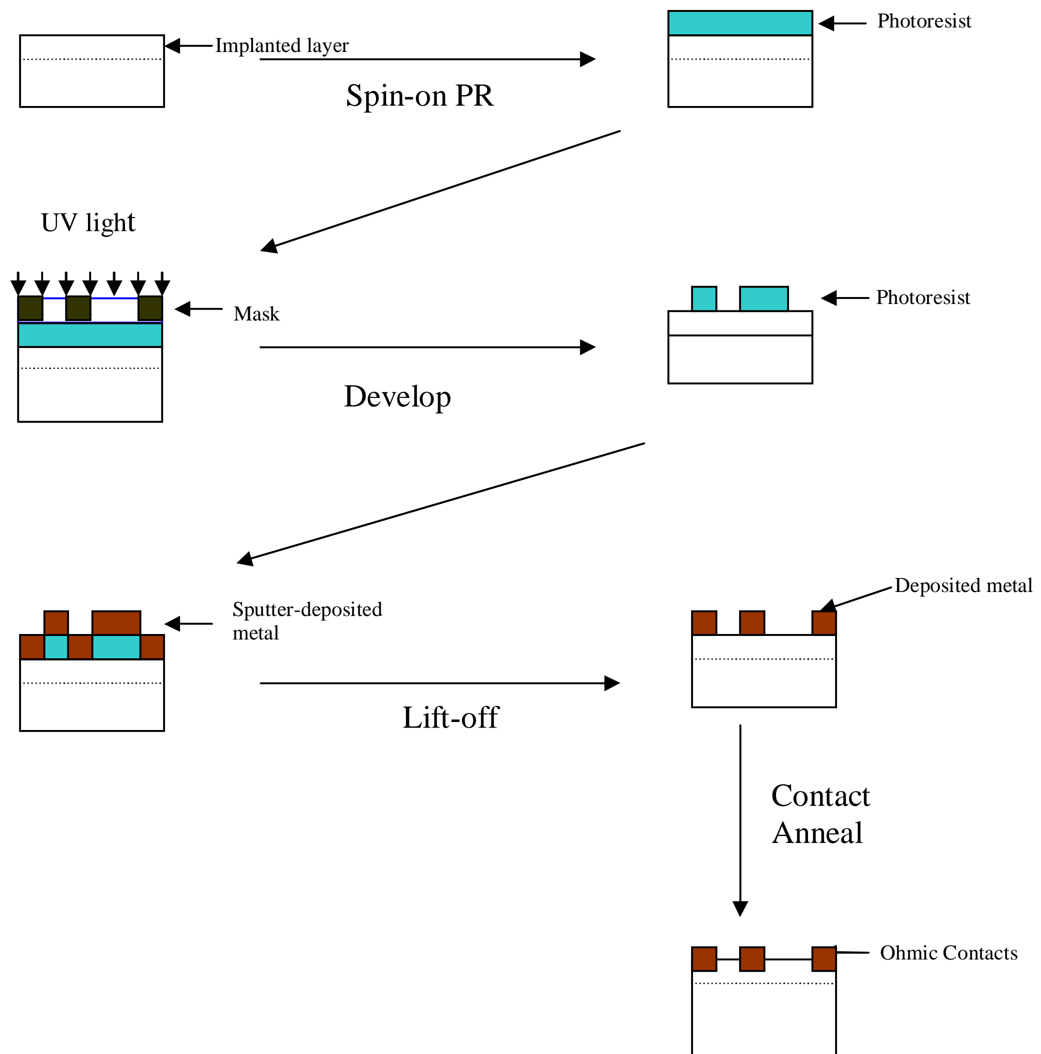

Fig. 4.14: Sequence of ohmic contact fabrication.

.

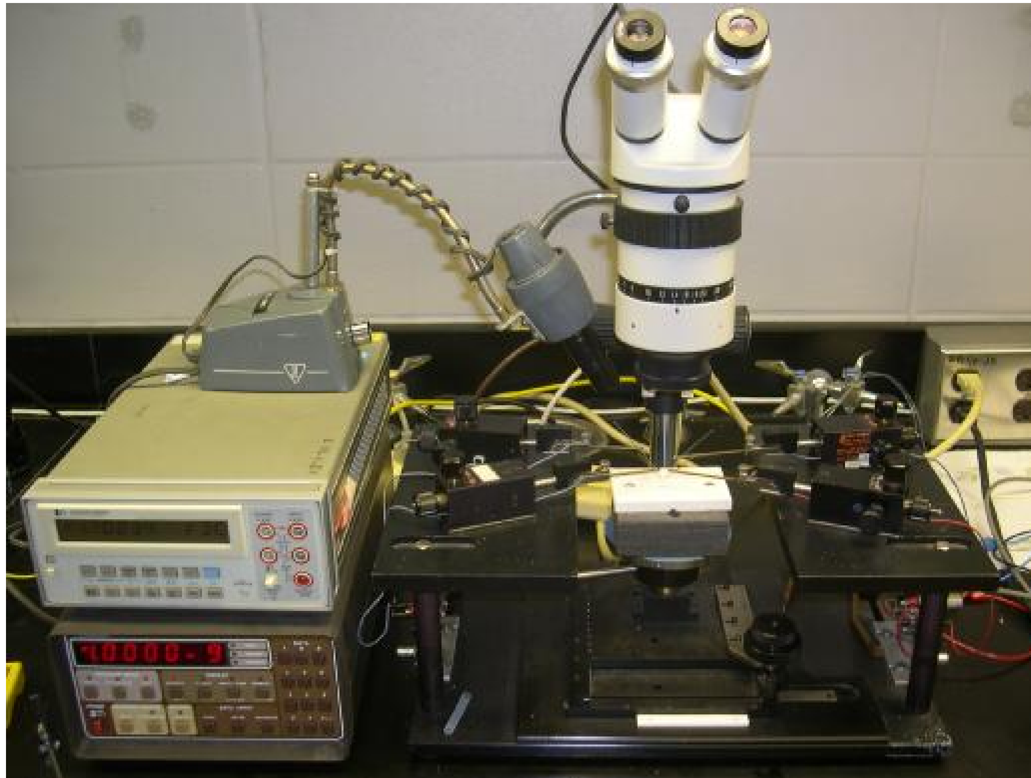

(a)

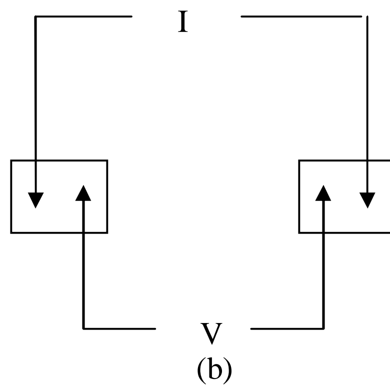

(b)

Fig. 4.15: (a) LTLM System; (b) Equivalent circuit of TLM measurement.

4.2.4 Hall Effect Measurement

The Hall system shown in Fig. 4.16 (a) includes a liquid nitrogen VPF-700 Cryostat, a GMW Model 5403 electromagnet, a KEPCO power supply, KEITHLEY 7001 switch system, KEITHLEY 6514 system electrometer, KEITHLEY 6220 precision current source and a temperature controller. The temperature range is available 77K to 700K, and the maximum sourcing current is 100 mA. The electromagnet is water cooled with a maximum magnetic field strength 0.6 T.

The Hall measurements are taken in the range 300K to 700K for both N- and Al-implanted samples. The Hall sample is held on the sample holder as shown in Fig. 4.16 (b) and four wires from the holder are connected to the sample (two for sourcing current and two for voltage measurement). The sample holder is then inserted into the cryostat. The sourcing current is kept less than 10mA since high current can heat up the sample and cause error in the measurement. The magnetic field varies from 0.1T to 0.6T.

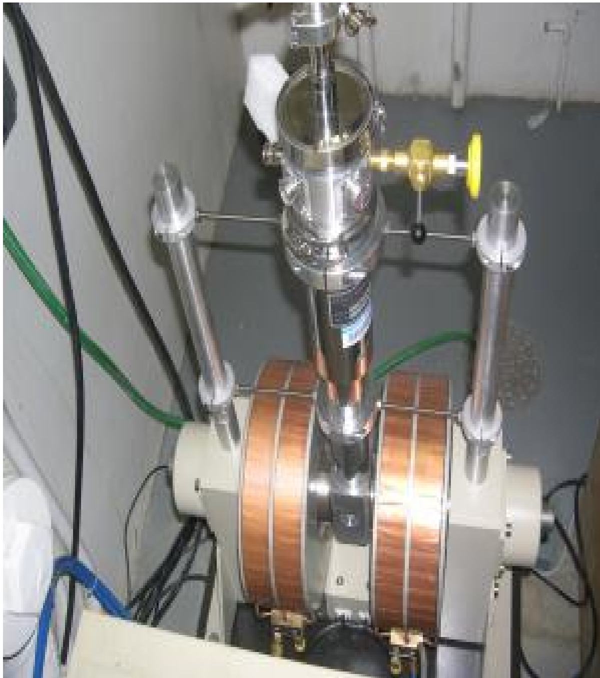

(a) (b)

Fig. 4.16: (a) Overall view of Hall system; (b) Sample holder inserted in cryostat.

CHAPTER 5

RESULTS AND DISCUSION

5.1 AFM Measurements

Surface roughness is a very important factor which can affect the performance of SiC devices. For instance, the channel mobility of carriers in a MOSFET is closely related to semiconductor surface roughness. As discussed in the previous chapter, an oxide layer was grown and a Mo layer was deposited on top of the oxide layer before implantation. Those two extra layers were removed completely after implantation. In order to compare the sample surface before and after implantation, AFM scans were taken for both virgin and implanted samples as shown in Fig. 5.1 to Fig. 5.11. The measured surface roughness of Al-implanted samples are 0.39, 0.73, 0.64, 0.51, 0.34 and 0.53 nm, corresponding to implant concentrations 0 (n type virgin), 2×10^{18}, 8×10^{18}, 2×10^{19}, 8×10^{19} and 2×10^{20} cm^{-3}, respectively. The measured surface roughness of N-implanted samples are 0.73, 0.45, 0.44, 0.51 and 0.32 nm, corresponding to implant concentrations 0 (p type virgin), 4×10^{18}, 1×10^{19}, 4×10^{19} and 1×10^{20} cm^{-3}, respectively.

AFM results show that the surface roughness of the implanted samples is similar to that of virgin samples for both types. For most of the samples, signal/noise ratio was poor, which suggests that the roughness measurement is close to the sensitivity limit of the profilometer setup. In addition, RBS performed on N-implanted samples with

implant concentrations 1×10^{19} and 1×10^{20} cm^{-3} does not show any trace of Mo. As a conclusion, the damage to sample surface from implantation is small.

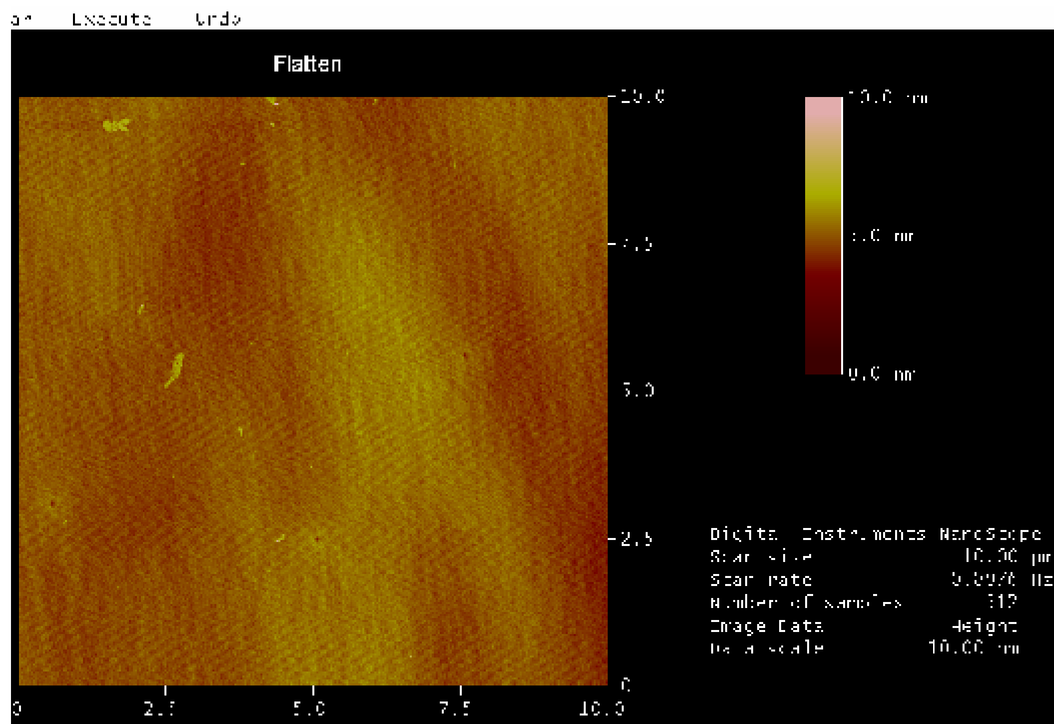

Fig. 5.1: AFM for n type virgin sample with surface roughness 0.39nm.

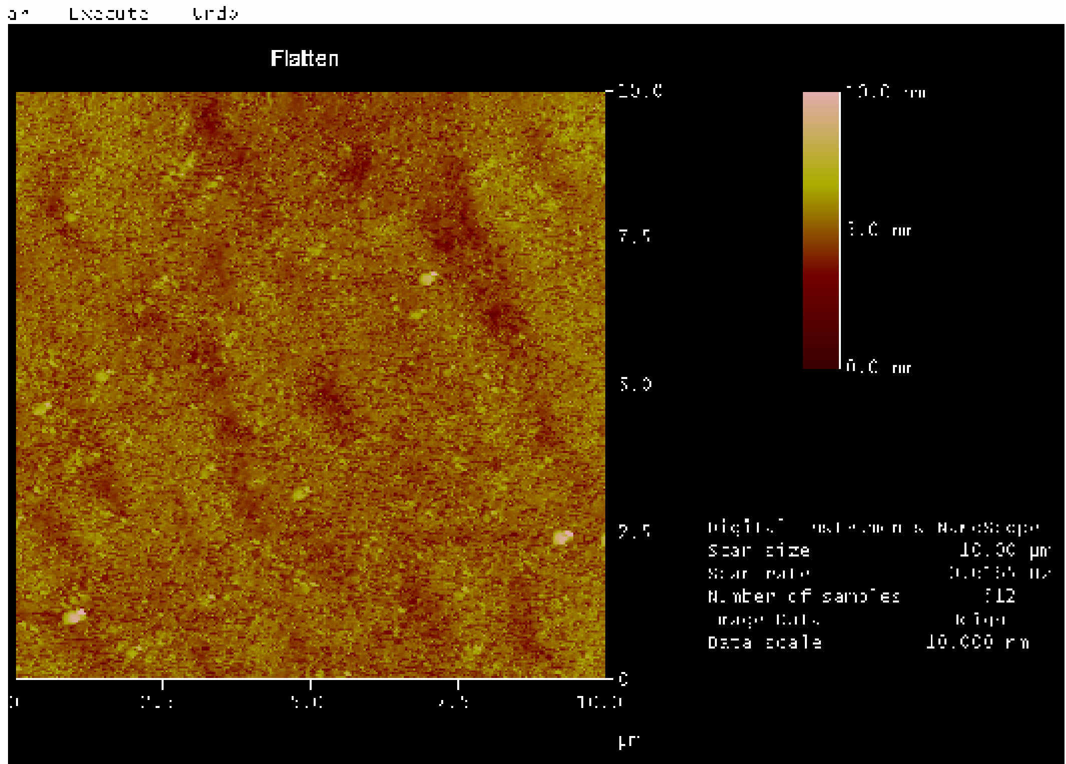

Fig. 5.2: AFM for Al-implanted sample (2×10^{18} cm^{-3}) with surface roughness 0.79nm.

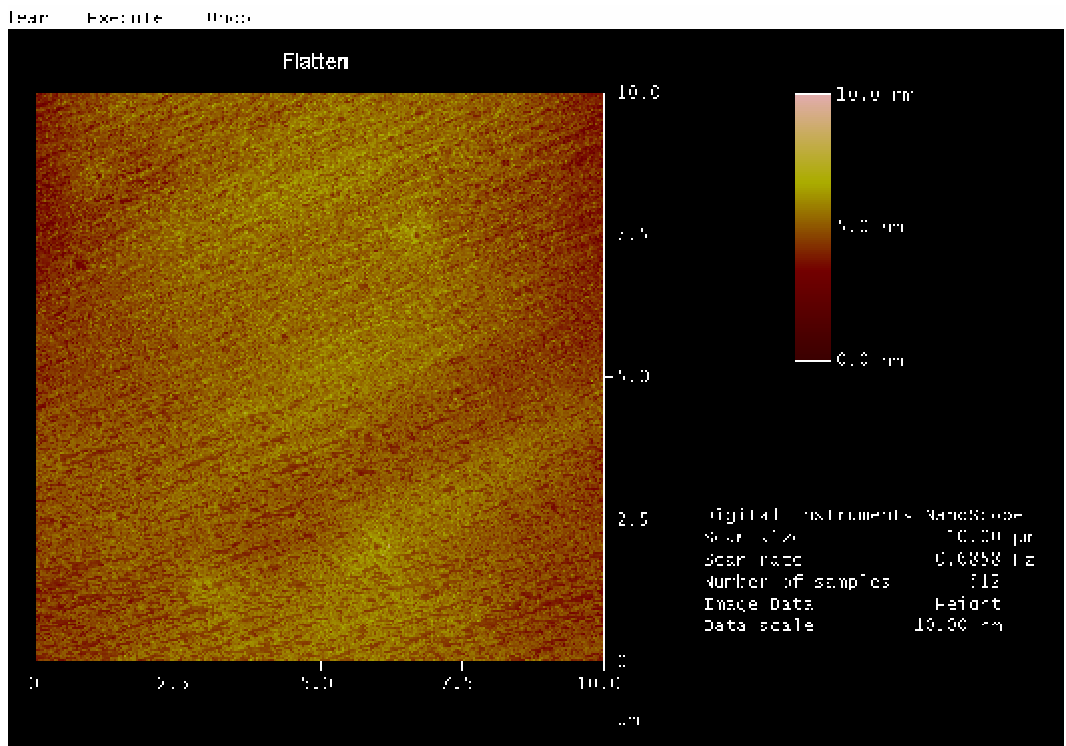

Fig. 5.3: AFM for Al-implanted sample (8×10^{18} cm^{-3}) with surface roughness 0.64nm.

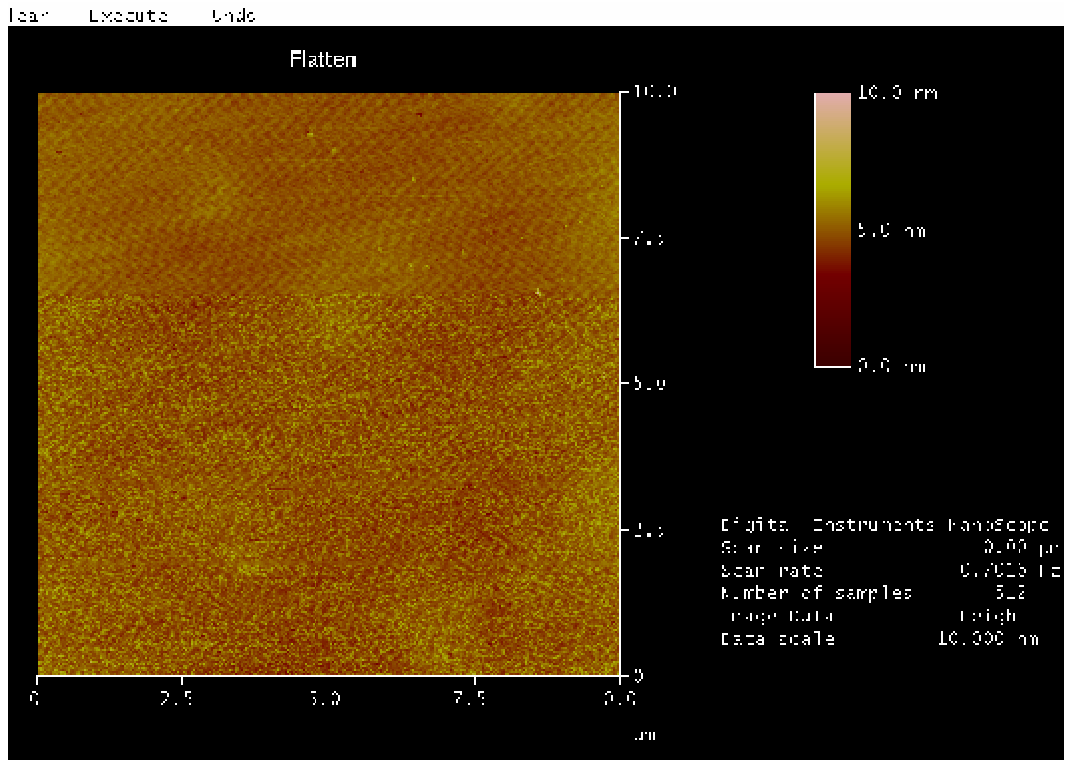

Fig. 5.4: AFM for Al-implanted sample (2×10^{19} cm^{-3}) with surface roughness 0.51nm.

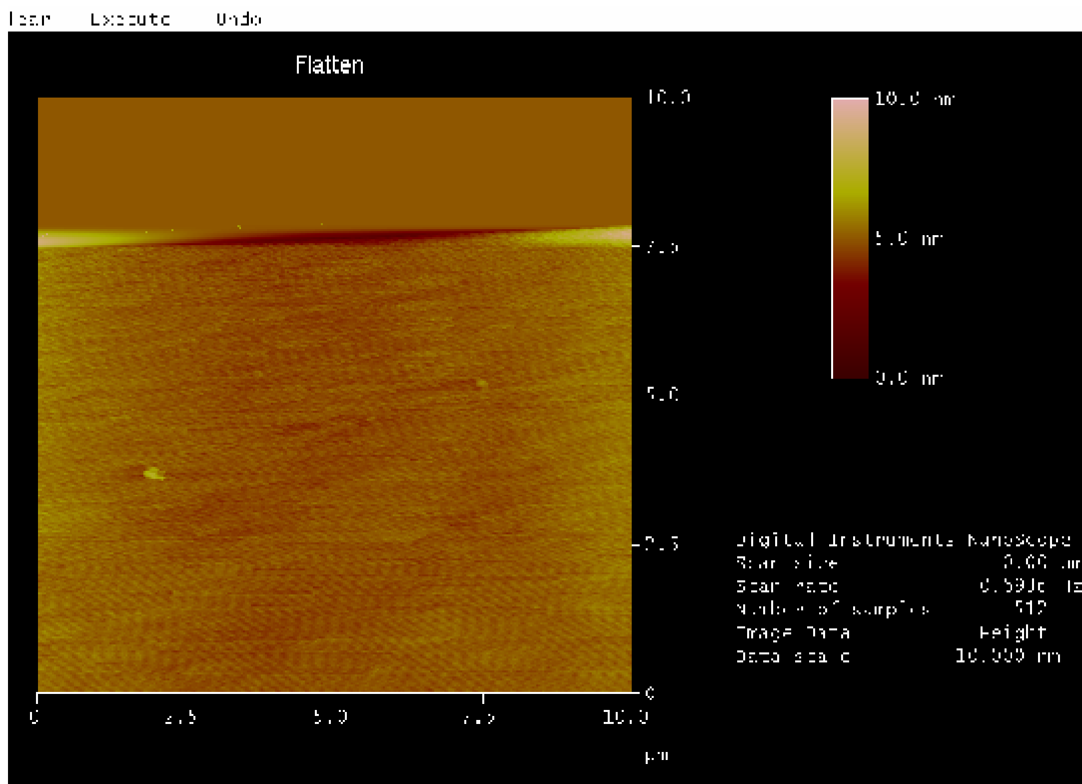

Fig. 5.5: AFM for Al-implanted sample (8×10^{19} cm^{-3}) with surface roughness 0.34nm.

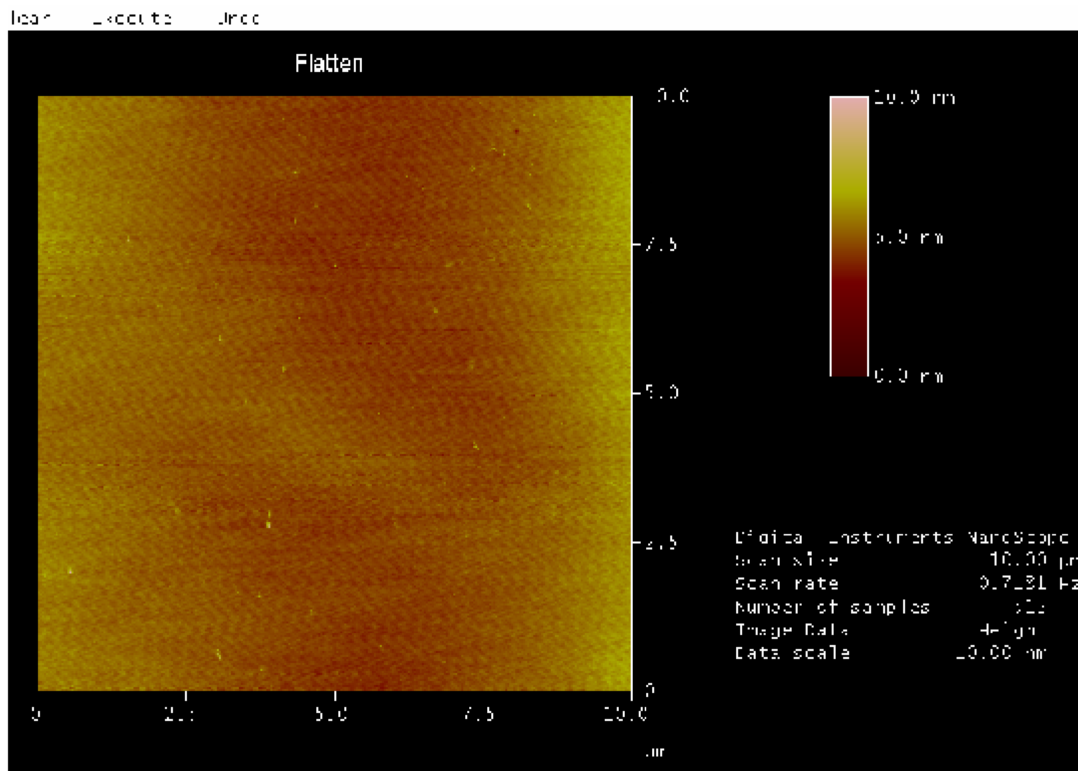

Fig. 5.6: AFM for Al-implanted sample (2×10^{20} cm^{-3}) with surface roughness 0.53nm.

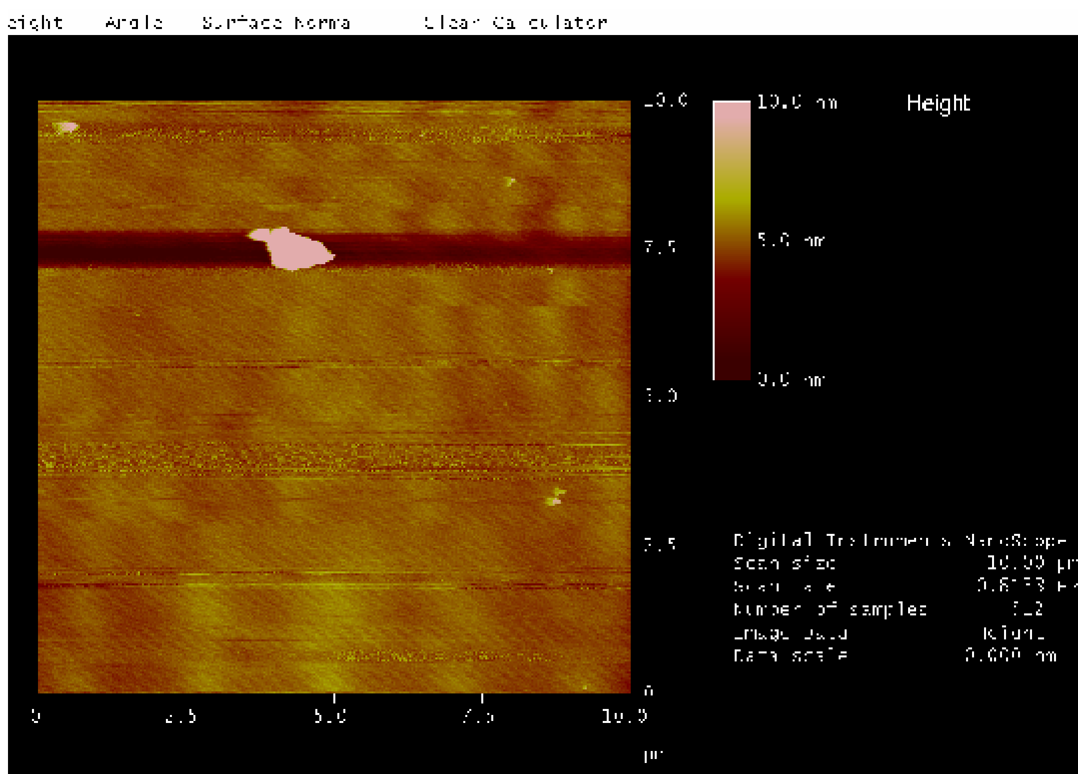

Fig. 5.7: AFM for p type virgin sample with surface roughness 0.73nm.

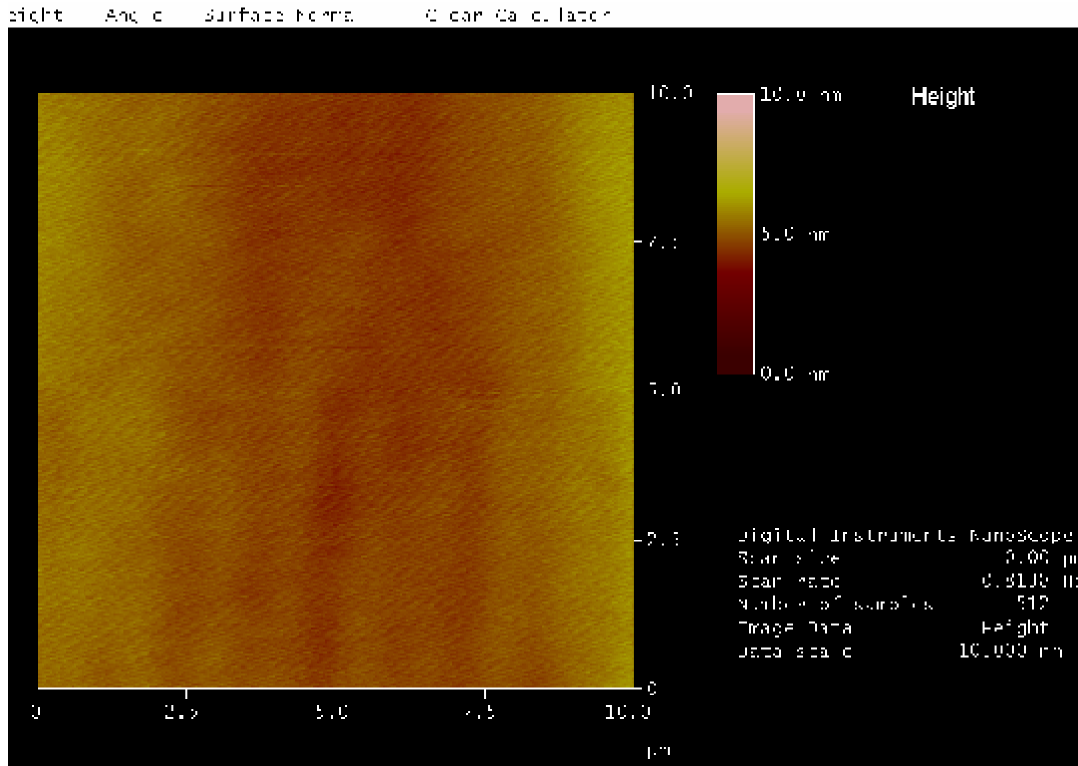

Fig. 5.8: AFM for N-implanted sample (4×10^{18} cm^{-3}) with surface roughness 0.45nm.

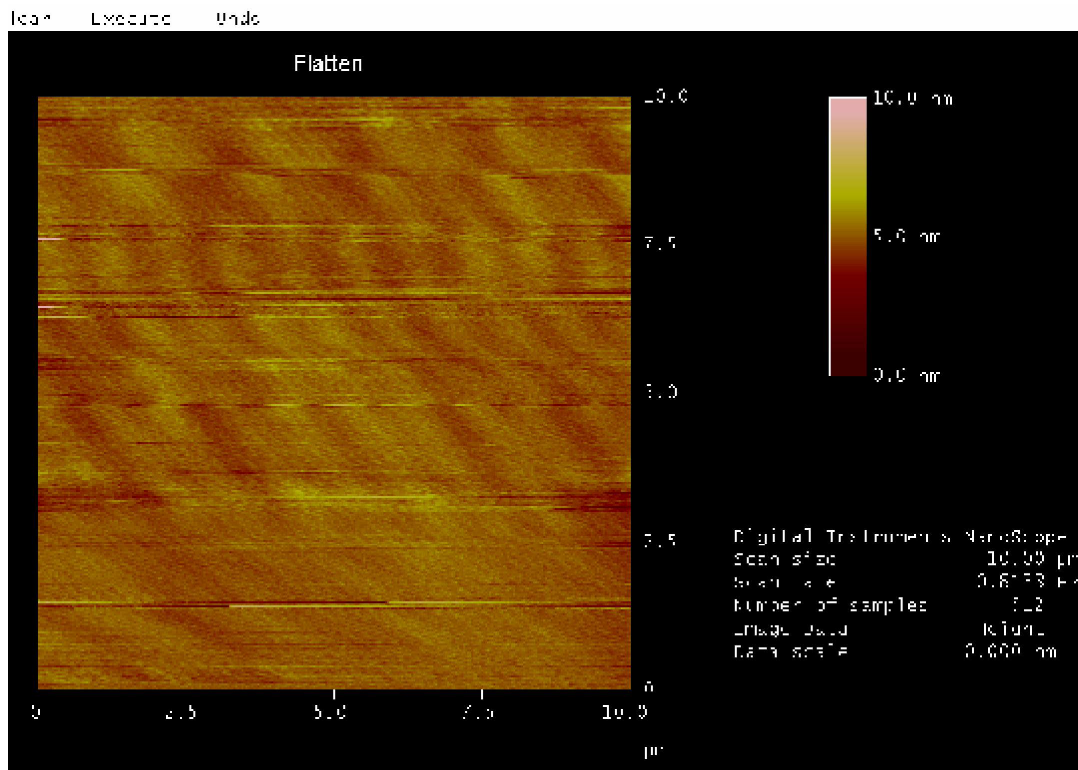

Fig. 5.9: AFM for N-implanted sample (1×10^{19} cm^{-3}) with surface roughness 0.44nm.

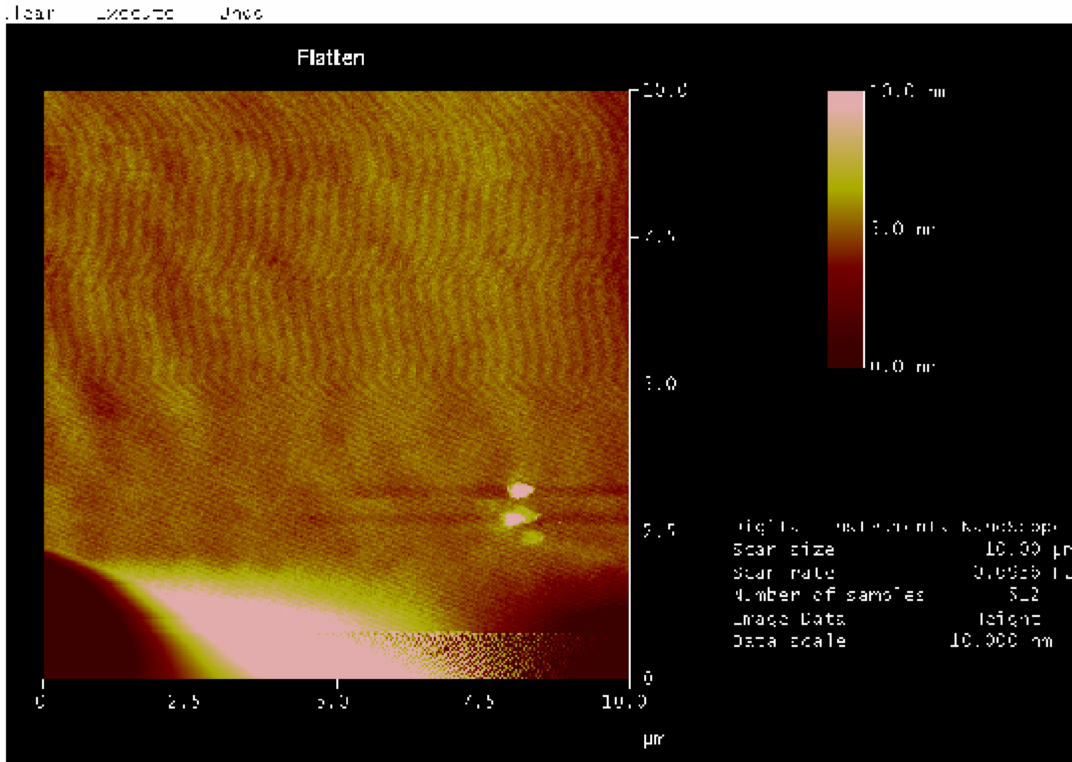

Fig. 5.10: AFM for N-implanted sample (4×10^{19} cm^{-3}) with surface roughness 0.51nm.

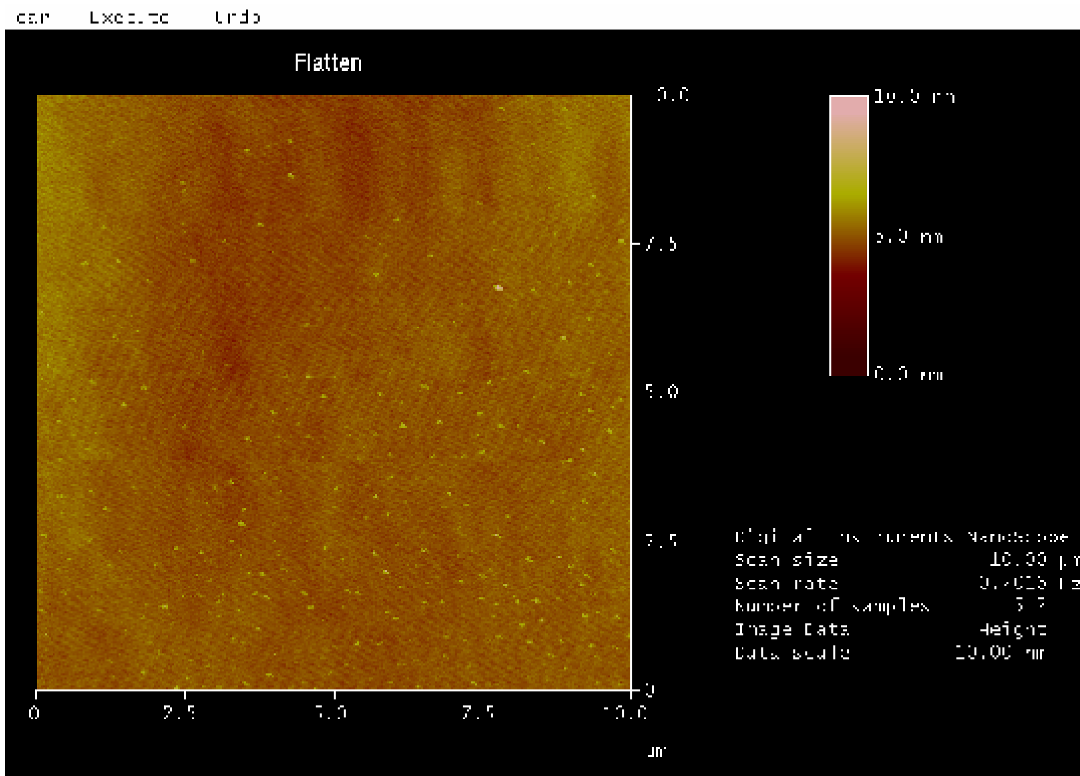

Fig. 5.11: AFM for N-implanted sample (1×10^{20} cm^{-3}) with surface roughness 0.32nm.

5.2 Optimization of Contact Anneal

5.2.1 NiV7% Contact Annealed at 1000°C

NiV7% contacts were fabricated on N-implanted samples with implant concentrations 1×10^{18}, 4×10^{18} and 1×10^{19} cm^{-3}. In order to study the annealing time dependence of contact resistance at a fixed temperature, alloy contacts were initially annealed at 1000°C at vacuum 10^{-7} Torr for 2 min. Then, they were re-annealed for 1 more minute each time up to 5 min in total under the same anneal conditions.

The total resistance between two contact pads (200um×200um) with a gap (76 um) was measured after each anneal. The corresponding values for all three implant concentrations are listed in Table 5.1. Fig. 5.12 shows the total resistance as a function of annealing time for each implant concentration. It can be seen that the contact resistance becomes stable after the second anneal for all the three implant concentrations. TLM measurements were also performed after the last time anneal. The extracted physical parameters including specific contact resistance and sheet resistance from both TLM and Van der Pauw techniques are given in Table 5.2. TLM data for each implant concentration annealed for 2+1+1+1 minutes are shown in Fig. 5.13-5.15. No trend can be seen in Fig. 5.13 from the data points for implant concentration 1×10^{18} cm^{-3}. This is due to the fact that contact resistance is high for the low implant concentration. Both the TLM and averaged TLM data for implant concentrations 4×10^{18} cm^{-3} (Fig. 5.14) and 1×10^{19} cm^{-3} (Fig. 5.15) show a clear trend, where the total resistance goes linearly with contact pad interspacing. This is because contact resistance is lower for higher implant

concentration. This work has shown that the annealing time should be 3 min at least at anneal temperature 1000°C and that higher anneal temperature (>1000°C) is needed for N-implanted samples with implant concentration below 4×10^{18} cm^{-3}.

Anneal Time (min.)	N1E18 R(Ω)	N4E18 R(Ω)	N1E19 R(Ω)
2	2205	556	103
2+1	1135	288	104
2+1+1	975	239	101
2+1+1+1	962	216	99

Table 5.1: Resistance between two NiV7% contacts (200um×200um) separated by 76 um.

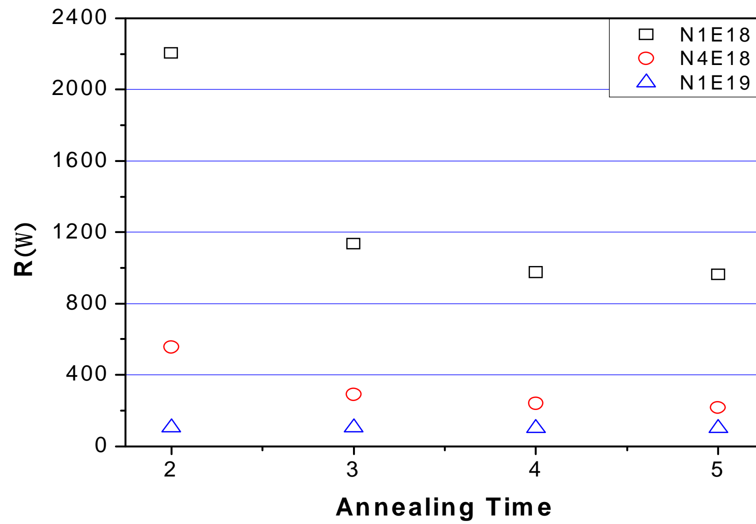

Fig. 5.12: Resistance as a function of annealing time for NiV7% contacts with a gap 76um.

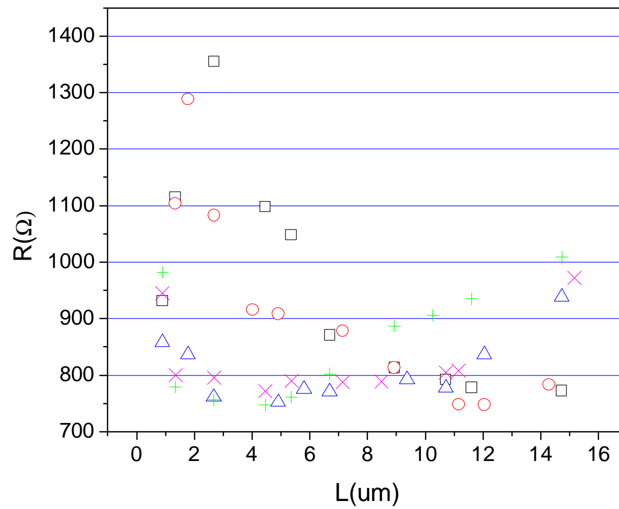

Fig. 5.13: TLM data for NiV7% contacts with N implant concentration 1×10^{18} cm^{-3} annealed at 1000°C /2+1+1+1min/vacuum. Each type of symbol represents the data from one TLM stripe.

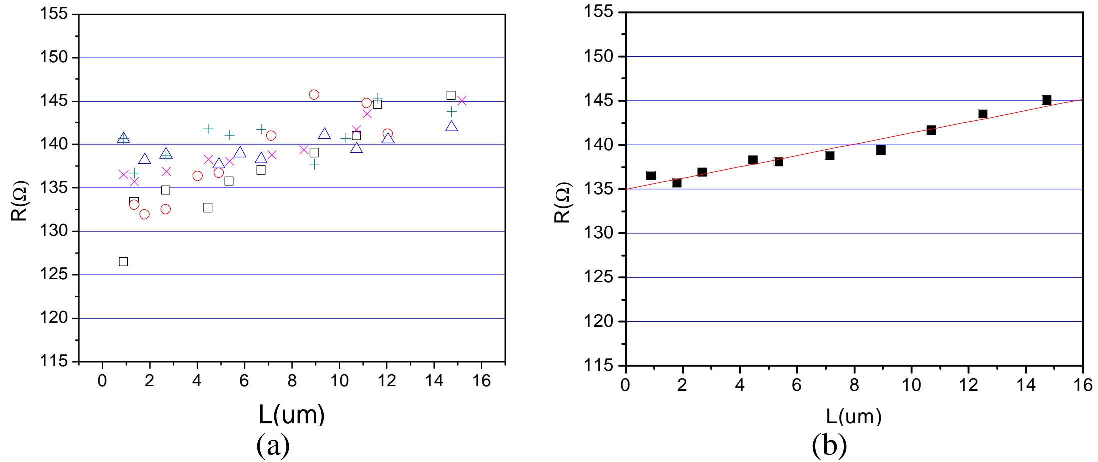

Fig. 5.14: TLM data for NiV7% contacts to N implant concentration 4×10^{18} cm^{-3} annealed at 1000°C/2+1+1+1min/vacuum. (a) R as a function of interspaces. Each type of symbol represents the data from one TLM stripe. (b) The averaged R values from all TLM stripes with a linear fit.

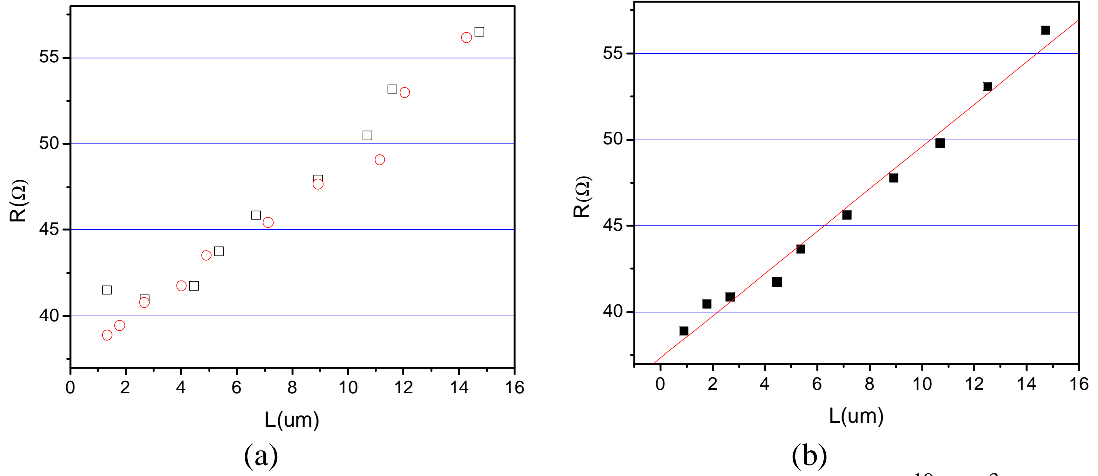

(a) (b)

Fig. 5.15: TLM data of NiV7% contacts for N implant concentration 1×10^{19} cm^{-3} annealed at 1000°C/2+1+1+1min/vacuum. (a) R as a function of interspaces. Each type of symbol represents the data from one TLM stripe. (b) The averaged R values from all TLM stripes with a linear fit.

Impl. Conc. (cm^{-3})	R_{sh} (Ω/□) (Van der Pauw)	R_{sh} (Ω/□) (TLM)	R_c (Ω) (TLM)	r_c (Ω·cm^2) (TLM)
1×10^{18}	583	no	no	no
4×10^{18}	309	226	65	1.43×10^{-2}
1×10^{19}	190	148	22	5.7×10^{-4}

Table 5.2: Summery of TLM and Vander der Pauw results for NiV7% contacts annealed at 1000 °C /2+1+1+1min/vacuum. "no" means data is unavailable.

5.2.2 Ni80Cr20 contacts annealed at 1000°C

In order to compare with NiV7% contact, especially for low implant concentrations, Ni80Cr20 contacts were also fabricated on a piece of N-implanted sample with implant concentration 1×10^{18} cm^{-3}. These contacts were annealed three times, each time for 2 minutes. After each anneal, the sample was probed to see if the contacts were

ohmic. If so, the TLM and Van der Pauw patterns were probed to yield specific contact resistance values.

Due to the high contact resistance, TLM analysis was not possible until the sample was annealed for a third time, for an annealing time of 6 minutes in total, as shown in Fig. 5.16. The extracted specific contact resistance is about 10^{-5} Ω.cm^2 The TLM and Van der Pauw results after each anneal are shown in Table. 5.3. Compared with NiV7% contact, lower contact resistance for Ni80Cr20 contact can be achieved at anneal temperature 1000°C, but longer anneal time (6 minutes) is needed.

Anneal Time (min.)	R_{sh} ($\Omega/\square$) (Van der Pauw)	R_{sh} ($\Omega/\square$) (TLM)	R_c (Ω) (TLM)	r_c ($\Omega \cdot cm^2$) (TLM)
2	419	no	no	no
2+2	395	no	no	no
2+2+2	340	627	8.7	8.72×10^{-5}

Table 5.3: TLM results for N implant concentration 1×10^{18} cm^{-3} with Ni80Cr20 contacts annealed at 1000°C in vacuum. “no” means data is unavailable.

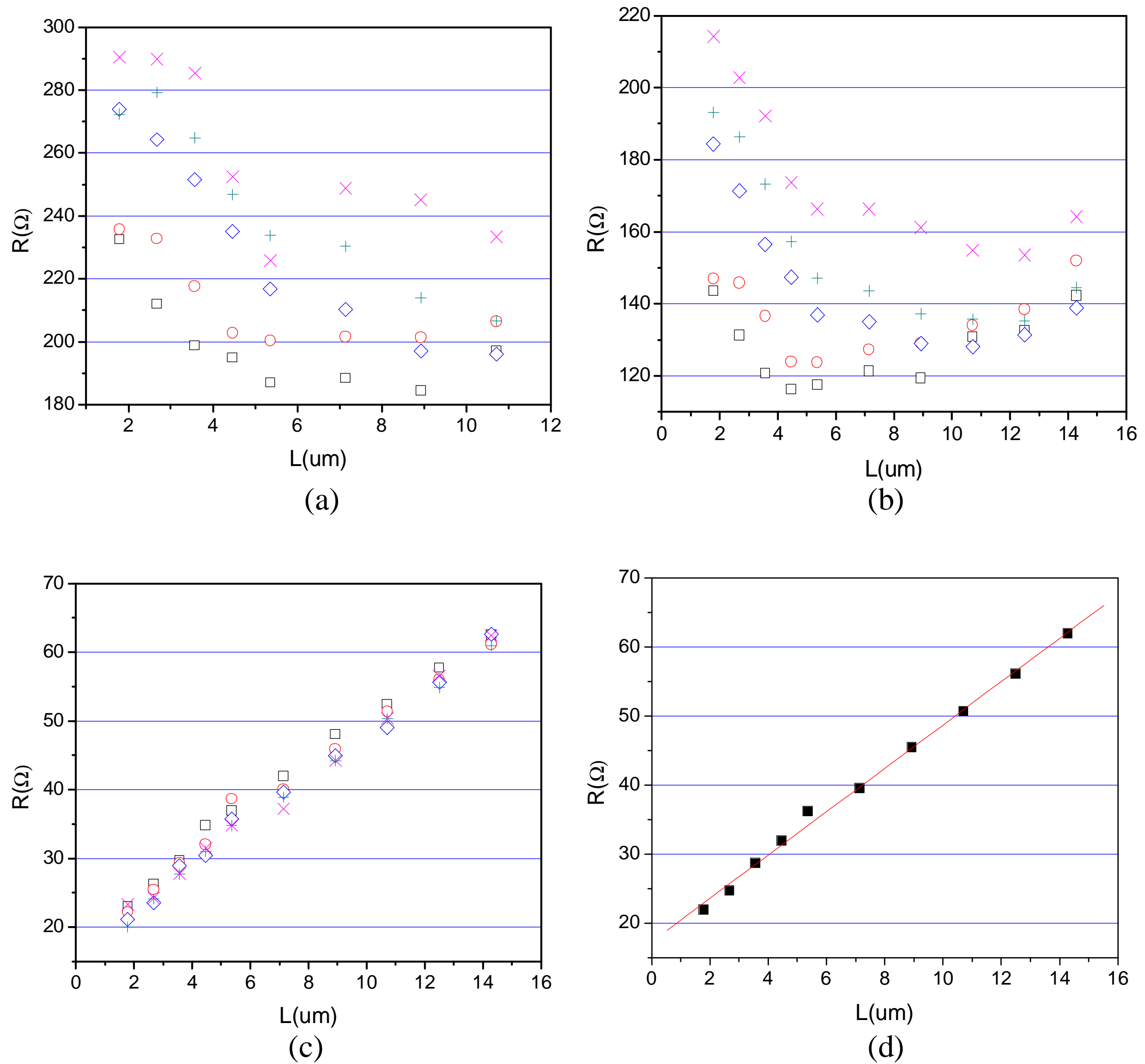

Fig. 5.16: TLM data of Ni80Cr20 contacts for N implant concentration 1×10^{18} cm^{-3} annealed at 1000^oC in vacuum. Each type of symbol represents the data from one TLM stripe; (a) annealed at 1000^oC/2min/vacuum; (b) annealed at 1000^oC/2+2min/vacuum; (c) annealed at 1000^oC/2+2+2min/vacuum; (d) The averaged R value of 4 TLM strips with a linear fit, annealed at 1000^oC/2min/vacuum.

5.3 Ohmic Contacts to N-implanted Samples

5.3.1 NiV7% Contacts Annealed at 1000^oC/2min/vacuum

Previous work has shown that the specific contact resistance of NiV7% contacts can be improved significantly if higher annealing temperature is applied (>1000^oC) [61]. However, the higher anneal temperature and time can induce more damage to the real devices. For example, high temperature can degrade the gate oxide quality of a MOSFET. Therefore, NiV7% contacts were initially annealed at 1000^oC, instead of 1100^oC. TLM measurements were performed for a set of N-implanted samples with implant concentration 1×10^{18}, 4×10^{18}, 1×10^{19}, 4×10^{19} and 1×10^{20} cm^{-3}, respectively. TLM data for each implant concentration are given in Fig. 5.17. It can be seen that contacts are getting better when the implant concentration increases. The extracted physical parameters including sheet resistance and specific contact resistance from both the TLM and Van der Pauw techniques are given in Table 5.4. It should be pointed out that TLM analysis can't be done for implant concentration 1×10^{18} cm^{-3} since the TLM data points are chaotic as shown in Fig. 5.17(a). In addition, the extracted sheet resistances from TLM are in good agreement with that from the Van der Pauw technique for implant concentrations 1×10^{19}, 4×10^{19} and 1×10^{20} cm^{-3}, which suggests that the TLM results are reliable for those implant concentrations.

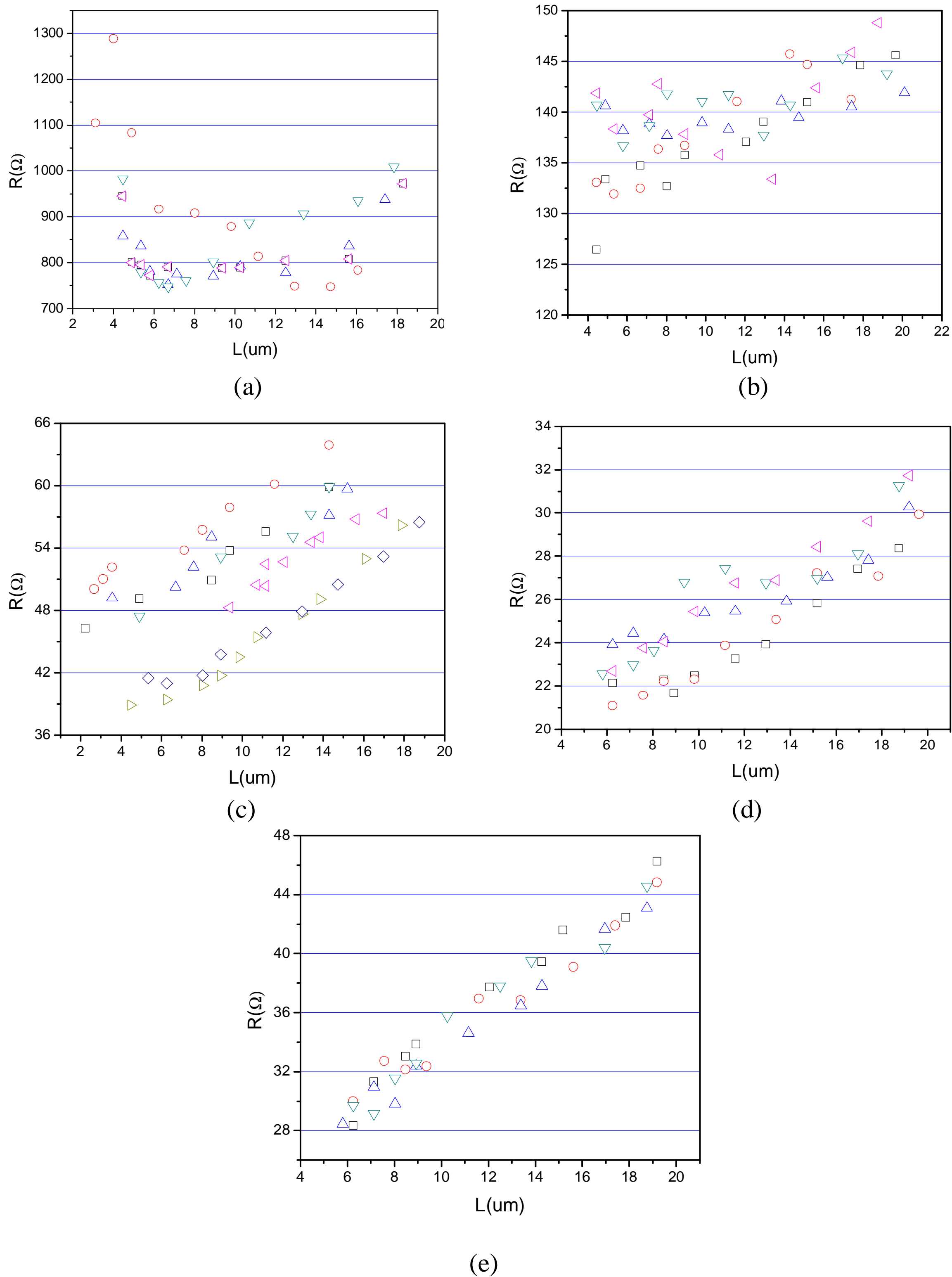

Fig. 5.17: TLM data of NiV7% contacts annealed at 1000°C/2min/vacuum for implant concentration (a) 1×10^{18} cm^{-3}, (b) 4×10^{18} cm^{-3}, (c) 1×10^{19} cm^{-3}, (d) 4×10^{19} cm^{-3} and (e) 1×10^{20} cm^{-3}. Each type of symbol represents the data from one TLM stripe.

Implant Conc. (1/cm^3)	Strip No.	R_c (Ω)	$r_c^{avg.}$ (Ω.cm^2) (TLM)	$R_{sh}^{avg.}$ (Ω/□) (TLM)	$R_{sh}^{avg.}$ (Ω/□) (Van der Pauw)
1×10^{18}	4	no	no	no	598
4×10^{18}	5	66.4	1.47×10^{-2}	120	326
1×10^{19}	6	16	4.1×10^{-4}	250	201
4×10^{19}	5	9.33	3.07×10^{-4}	114	148
1×10^{20}	4	11.2	2.17×10^{-4}	231	225

Table 5.4: Summary of specific contact resistance and sheet resistance measurement for N-implanted (0001) 4H-SiC annealed at 1000°C/2min/vacuum for NiV7% contacts. "no" means data is unavailable.

5.3.2 NiV7% Contacts Annealed at 1100°C/1min/vacuum

In the previous section, TLM results for NiV7% contacts annealed at 1000°C/2min/vacuum show that the extracted specific contact resistance values are in the region of 10^{-4} Ω·cm^2 for implant concentrations greater than 1×10^{19} cm^{-3}, and that no TLM analysis can be completed for implant concentration below 4×10^{18} cm^{-3}. Therefore, a higher anneal temperature 1100°C was also used to anneal NiV7% contacts for 1 minute in vacuum. In order to have more accurate results, more than one TLM sample was prepared for each implant concentration. The number of samples prepared were 4, 2, 2, 2 and 3 for implant concentrations 1×10^{18}, 4×10^{18}, 1×10^{19}, 4×10^{19}, and 1×10^{20} cm^{-3}, respectively. The TLM data are shown in Figs. 5.18 - 5.22, and the extracted sheet resistance, contact resistance and specific contact resistance are listed in Table 5.5 - 5.9 for each implant concentration. As can be seen, a clear linear relationship between total

resistance and pad inter-space is observed for each implant concentration. The specific contact resistance also drops by one order of magnitude to $10^{-5} \sim 10^{-6}$ Ω.cm^2.

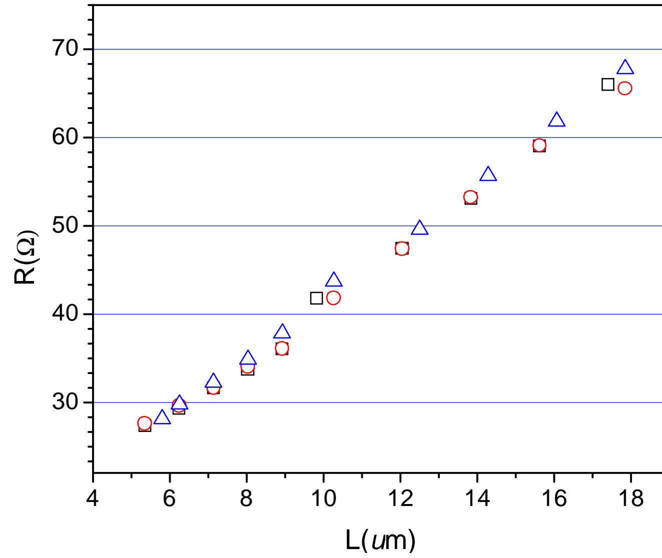

Fig. 5.18: TLM data from one of four prepared samples with implant concentration 1×10^{18} cm^{-3}.

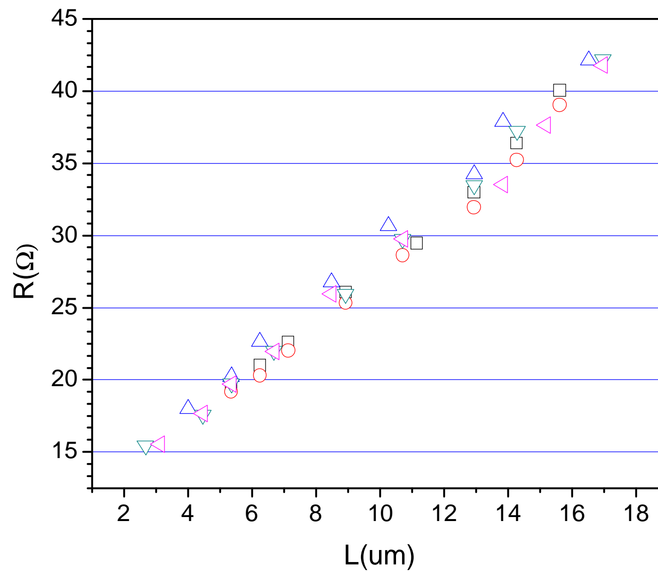

Fig. 5.19: TLM results from one of two prepared samples with implant concentration 4×10^{18} cm^{-3}.

Strip No.	LTLM			Van Der Pauw
	$R_c\,(\Omega)$	$R_{sh}\,(\Omega/\square)$	$r_c\,(\Omega \cdot cm^2)$	$R_{sh}\,(\Omega/\square)$
1	4.89	612.9	1.56×10^{-5}	Pattern 1: R_{sh}=487 Pattern 2: R_{sh}=784 Pattern 3: R_{sh}=692 Pattern 4: R_{sh}=693 Pattern 5: R_{sh}=754 Pattern 6: R_{sh}=457 Pattern 7: R_{sh}=400 Pattern 8: R_{sh}=516
2	4.79	622.2	1.47×10^{-5}	
3	5.11	618.7	1.69×10^{-5}	
4	7.36	874.6	2.48×10^{-5}	
5	6.06	857.3	1.71×10^{-5}	
6	9.43	692.5	5.13×10^{-5}	
7	8.18	700.16	3.82×10^{-5}	
8	5.44	659.1	1.79×10^{-5}	
9	5.10	637.9	1.63×10^{-5}	
10	3.88	697.7	8.64×10^{-6}	
11	3.38	699.5	6.55×10^{-6}	
12	3.0	713.2	5.04×10^{-6}	
Avg.	5.55	698.8	1.94×10^{-5}	599
d	1.92	85.9	1.33×10^{-5}	149

Table 5.5: Summary of specific contact resistance and sheet resistance measurement for N-implanted (0001) 4H-SiC with implant concentration 1×10^{18} cm^{-3}.

Strip No.	LTLM			Van der Pauw
	$R_c\,(\Omega)$	$R_{sh}\,(\Omega/\square)$	$r_c\,(\Omega \cdot cm^2)$	$R_{sh}\,(\Omega/\square)$
1	4.41	385.7	2.02×10^{-5}	Pattern 1: R_{sh}=298 Pattern 2: R_{sh}=240 Pattern 3: R_{sh}=287 Pattern 4: R_{sh}=304 Pattern 5: R_{sh}=302 Pattern 6: R_{sh}=270 Pattern 7: R_{sh}=270
2	4.30	375.8	1.97×10^{-5}	
3	5.11	388	2.70×10^{-5}	
4	4.72	381.4	2.34×10^{-5}	
5	4.86	368	2.56×10^{-5}	
6	3.44	376.8	1.25×10^{-5}	
7	3.36	374.7	1.21×10^{-5}	
8	2.89	379.1	8.83×10^{-6}	
9	2.87	376.2	8.74×10^{-6}	
10	2.77	392.3	7.85×10^{-6}	
Avg.	3.87	379.8	1.66×10^{-5}	281
d	0.90	7.2	7.4×10^{-6}	23

Table 5.6: Summary of specific contact resistance and sheet resistance measurement for N-implanted (0001) 4H-SiC with implant concentration 4×10^{18} cm^{-3}.

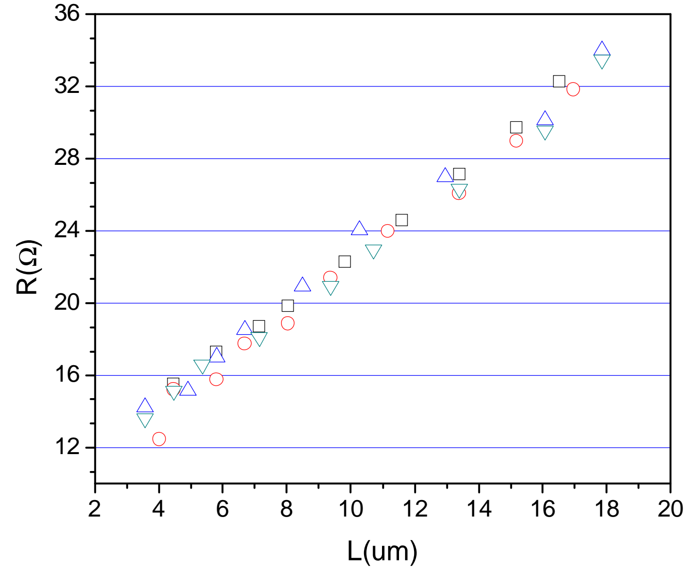

Fig. 5.20: TLM data from one of two prepared samples with implant concentration 1×10^{19} cm^{-3}.

Strip No.	LTLM			Van Der Pauw
	$R_c\,(\Omega)$	$R_{sh}\,(\Omega/\square)$	$r_c\,(\Omega\cdot cm^2)$	$R_{sh}\,(\Omega/\square)$
1	4.54	273.1	3.02×10^{-5}	Pattern 1: R_{sh}=233 Pattern 2: R_{sh}=188 Pattern 3: R_{sh}=184 Pattern 4: R_{sh}=255 Pattern 5: R_{sh}=260 Pattern 6: R_{sh}=300
2	3.97	279.4	2.26×10^{-5}	
3	4.59	273.1	3.09×10^{-5}	
4	4.49	263.7	3.06×10^{-5}	
5	1.80	304.2	4.27×10^{-6}	
6	1.47	301.3	2.88×10^{-6}	
7	1.97	288.1	5.38×10^{-6}	
8	2.04	286	5.81×10^{-6}	
9	2.16	278.2	6.74×10^{-6}	
Avg.	3.00	283.0	1.55×10^{-5}	237
d	1.35	13.3	1.27×10^{-5}	45

Table 5.7: Summary of specific contact resistance and sheet resistance measurement for N-implanted (0001) 4H-SiC with implant concentration 1×10^{19} cm^{-3}.

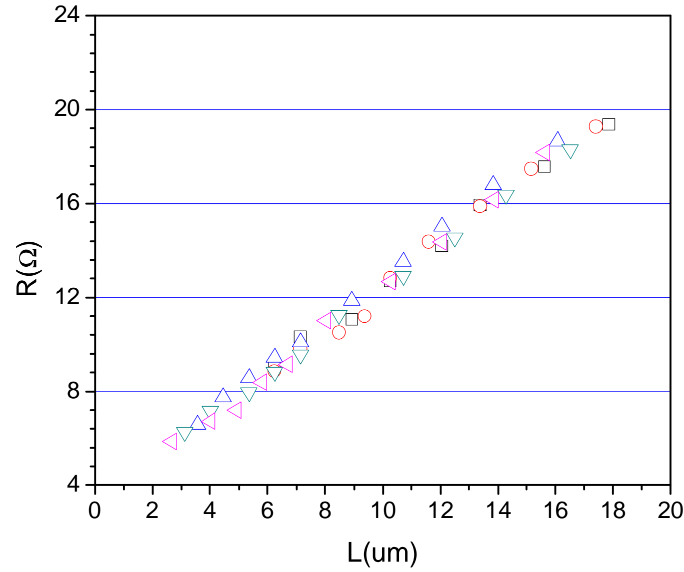

Fig. 5.21: TLM data from one of the two prepared samples with implant concentration 4×10^{19}cm^{-3}.

Strip No.	LTLM			Van Der Pauw
	$R_c\,(\Omega)$	$R_{sh}\,(\Omega/\square)$	$r_c\,(\Omega\cdot cm^2)$	$R_{sh}\,(\Omega/\square)$
1	1.8	179	6.90×10^{-6}	Pattern 1: R_{sh}=114.76 Pattern 2: R_{sh}=133.91 Pattern 3: R_{sh}=163.03 Pattern 4: R_{sh}=142 Pattern 5: R_{sh}=117 Pattern 6: R_{sh}=138
2	1.3	193	3.76×10^{-6}	
3	1.7	192	5.76×10^{-6}	
4	1.7	181	6.04×10^{-6}	
5	1.4	193	4.23×10^{-6}	
6	0.96	170.3	2.35×10^{-6}	
7	1.04	168.5	2.57×10^{-6}	
8	1.09	166.7	2.40×10^{-6}	
9	1.12	164.8	3.06×10^{-6}	
10	1.15	168.64	3.13×10^{-6}	
Avg.	1.3	177.7	4.02×10^{-6}	134.8
d	0.3	11.5	1.66×10^{-6}	17.8

Table: 5.8: Summary of specific contact resistance and sheet resistance measurement for N-implanted (0001) 4H-SiC with implant concentration 4×10^{19} cm^{-3}.

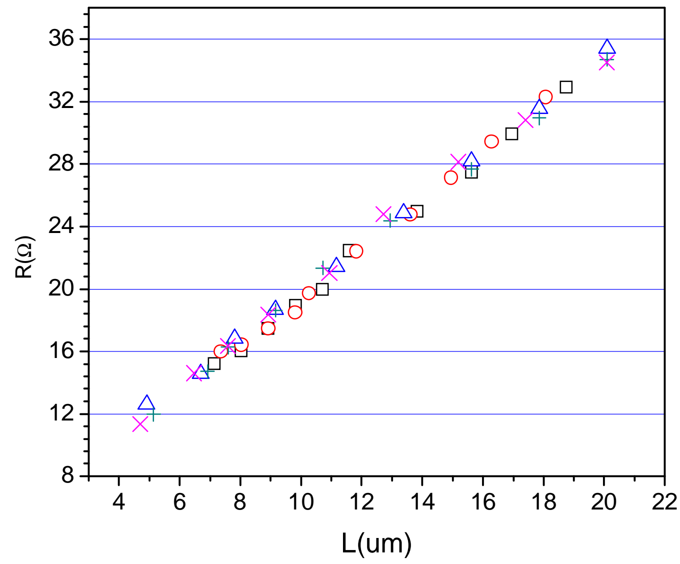

Fig. 5.22: TLM data from one of the three prepared samples with implant concentration 1×10^{20} cm^{-3}.

Strip No.	Small Gap			Van Der Pauw
	$R_c\,(\Omega)$	$R_{sh}\,(\Omega/\square)$	$r_c\,(\Omega \cdot cm^2)$	$R_{sh}\,(\Omega/\square)$
1	2.1	370	4.97×10^{-6}	Pattern 1: R_{sh}=222.89 Pattern 2: R_{sh}=257.78 Pattern 3: R_{sh}=210.26 Pattern 4: R_{sh}=189.38 Pattern 5: R_{sh}=230.94 Pattern 6: R_{sh}=296.35 Pattern 7: R_{sh}=178 Pattern 8: R_{sh}=147 Pattern 9: R_{sh}=151
2	2.3	358	5.93×10^{-6}	
3	2.3	370	5.71×10^{-6}	
4	1.8	368	3.57×10^{-6}	
5	2.0	311	4.90×10^{-6}	
6	1.9	314	4.39×10^{-6}	
7	2.4	300	7.87×10^{-6}	
8	2.4	297	7.70×10^{-6}	
9	2.4	301	7.77×10^{-6}	
10	1.5	203.8	4.34×10^{-6}	
11	1.4	203.7	3.94×10^{-6}	
12	1.5	205.5	4.48×10^{-6}	
13	1.6	200.4	4.97×10^{-6}	
14	1.4	213.0	3.48×10^{-6}	
Avg.	1.9	287	5.29×10^{-6}	209
d	0.4	68	1.52×10^{-6}	43

Table: 5.9: Summary of specific contact resistance and sheet resistance measurement for N-implanted (0001) 4H-SiC with implant concentration 1×10^{20} cm^{-3}.

Table 5.10 shows the summary of TLM and Van der Pauw results for the full set of implant concentrations. For each, the sheet resistance from TLM measurement is in a good agreement with that from Van der Pauw technique. In Fig. 5.23, the diamond symbols are the extracted specific contact resistances from epitaxial 6H-SiC samples [30]. The solid line is a theoretical calculation assuming a single parabolic energy barrier with a barrier height of 0.35eV [30]. The relationship of specific contact resistance as a function of barrier height and the semiconductor doping can be predicted by [30]

$$r_c \propto \exp\left(\frac{\Phi_B}{\sqrt{N}}\right) \tag{5.1}$$

To have a more accurate calculation, one must have knowledge of the semiconductor Fermi level, tunneling mass and other physical properties, and the current density and contact resistance should be evaluated [93, 94]. The calculated values were determined by [30, 61 and 70]

$$\frac{1}{r_c} = \frac{4pmq^2}{h^3}\int_0^\infty \frac{T(E)}{1+\exp\left[\frac{E-E_F}{kT}\right]}dE \tag{5.1}$$

where T(E) is the tunneling probability. The triangle symbols are the measured specific contact resistances from N-implanted samples. The experimental data points are far from the theoretical curve for implant concentrations 4×10^{19} and 1×10^{20} cm^{-3}. This is probably due to the damage to the crystal structure from high dose implantation, which might decrease the activation ratio of the implanted ions. Therefore, a higher activation temperature might be needed to have more implanted atoms activated.

To make sure that the implanted data drops as the increasing of implant concentration, the statistical analysis of variance between groups (ANOVA) was

performed [95, 96]. We have 5 data sets (one for each implant concentration), and each set has 9-14 measurements of r_c. Thus, a total of 54 degrees of freedom is obtained. For these data, a F-factor of approximately 3.5 implies a probability of less than 0.1% that the trend observed for the data is not real [97]. A higher F-value means lower probability, and the calculated F-value for our data is 7.4 (see Appendix).

Implant Conc. (cm^{-3})	Strip No.	$r_c^{avg.} \pm \Delta$ ($\Omega.cm^2$) (TLM)		$R_{sh}^{avg.} \pm \Delta$ ($\Omega/\square$) (TLM)		$R_{sh}^{avg.} \pm \Delta$ ($\Omega/\square$) (Van der Pauw)	
1e18	12	1.94×10^{-5}	$\pm$ 1.33×10^{-5}	699	± 86	599	±149
4e18	10	1.66×10^{-5}	$\pm$ 7.4×10^{-6}	380	± 7	281	± 23
1e19	9	1.55×10^{-5}	$\pm$ 1.27×10^{-5}	283	± 13	237	± 45
4e19	10	4.02×10^{-6}	$\pm$ 1.66×10^{-6}	178	± 12	135	± 18
1e20	14	5.29×10^{-6}	$\pm$ 1.52×10^{-6}	287	± 68	209	± 43

Table 5.10: Summary of specific contact resistance and sheet resistance measurement for N-implanted (0001) 4H-SiC.

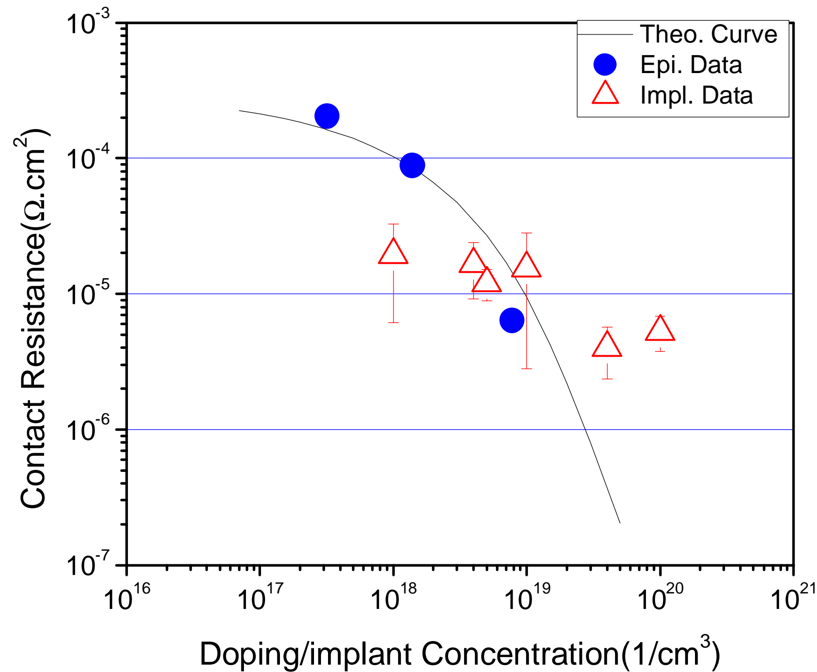

Fig. 5.23: Specific contact resistance vs. implant concentration for N-implanted 4H-SiC.

5.4 Ohmic Contacts to Al-implanted samples

Al70Ti30 was used to fabricate ohmic contacts to Al-implanted samples which were activated at 1650°C/30min/Ar with a carbon cap. The contacts were annealed at 1000°C/1min/vacuum. Since the contacts contains Al, it was initially assumed that contacts annealed at high temperature (>800°C) may result in diffusion of Al into SiC. Therefore, an enhanced p-type doping concentration near the surface can be achieved. A higher doping concentration corresponds to a narrower barrier height through which holes can quantum mechanically tunnel [30]. However, later work on Al-Ti contacts including surface studies of etched Al-Ti contact layers has revealed many pits in the SiC

surface. This suggests that Al may actually spike into the SiC surface, which leads to enhanced field emission by the creation of many small hemispherical intrusions [33].

The TLM data are shown in Fig. 5.24 - 5.28 for implant concentrations 2×10^{18}, 8×10^{18}, 2×10^{19}, 8×10^{19} and 2×10^{20} cm^{-3}, respectively. The extracted sheet resistance, contact resistance and specific contact resistance are listed in Table 5.11 - 5.15 for each implant concentration. In order to have more accurate results in the high implant concentration region, two TLM samples were prepared for concentration 8×10^{19} cm^{-3} and two for concentration 2×10^{20} cm^{-3}.

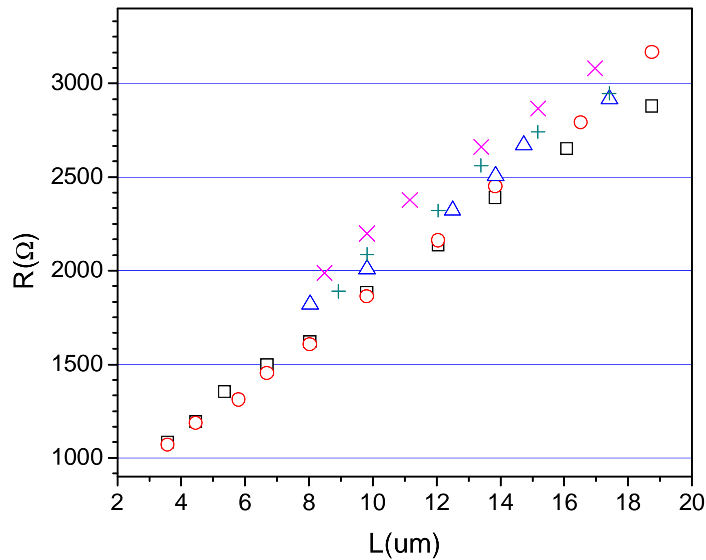

Fig. 5.24: TLM data from the sample with Al implant concentration 2×10^{18} cm^{-3}.

Strip No.	LTLM			Van Der Pauw
	$R_c\,(\Omega)$	$R_{sh}\,(\Omega/\square)$	$r_c\,(\Omega\cdot cm^2)$	$R_{sh}\,(\Omega/\square)$
1	338	24156	1.89×10^{-3}	Pattern 1: R_{sh}=13306 Pattern 2: R_{sh}=13915 Pattern 3: R_{sh}=12028
2	267	27542	1.04×10^{-3}	
3	421	24078	2.95×10^{-3}	
4	420	24780	2.84×10^{-3}	
5	469	25458	3.46×10^{-3}	
Avg.	383	25202	2.44×10^{-3}	13083
d	80	1420	9.65×10^{-4}	963

Table 5.11: Summary of specific contact resistance and sheet resistance measurement for Al-implanted (0001) 4H-SiC with implant concentration 2×10^{18} cm^{-3}.

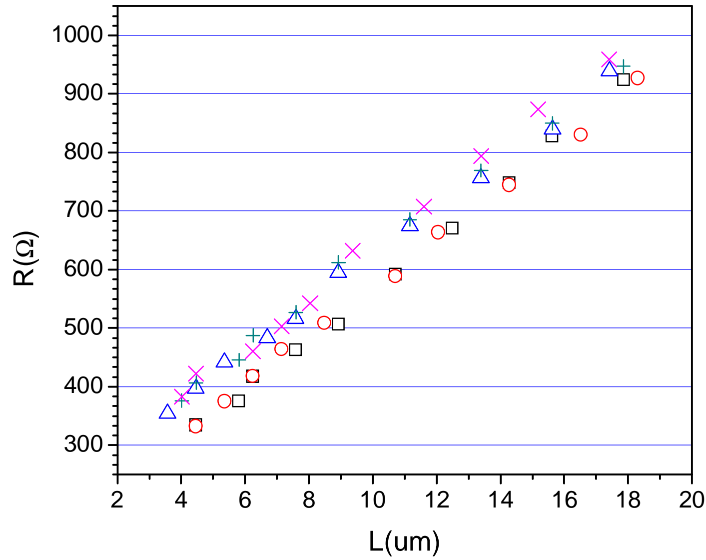

Fig. 5.25: TLM results from the sample with implant concentration 8×10^{18} cm^{-3}.

Strip No.	LTLM			Van Der Pauw
	$R_c\,(\Omega)$	$R_{sh}\,(\Omega/\square)$	$r_c\,(\Omega\cdot cm^2)$	$R_{sh}\,(\Omega/\square)$
1	63.18	8832	1.81×10^{-4}	Pattern 1: R_{sh}=6056 Pattern 2: R_{sh}=4910 Pattern 3: R_{sh}=5320
2	76.8	8831	2.83×10^{-4}	
3	106.6	8205	5.54×10^{-4}	
4	111.9	8140	6.15×10^{-4}	
5	103.1	8702	4.89×10^{-4}	
Avg.	92.3	8542	4.24×10^{-4}	5430
d	21.2	342	1.85×10^{-4}	580

Table 5.12: Summary of specific contact resistance and sheet resistance measurement for Al-implanted (0001) 4H-SiC with implant concentration 8×10^{18} cm^{-3}.

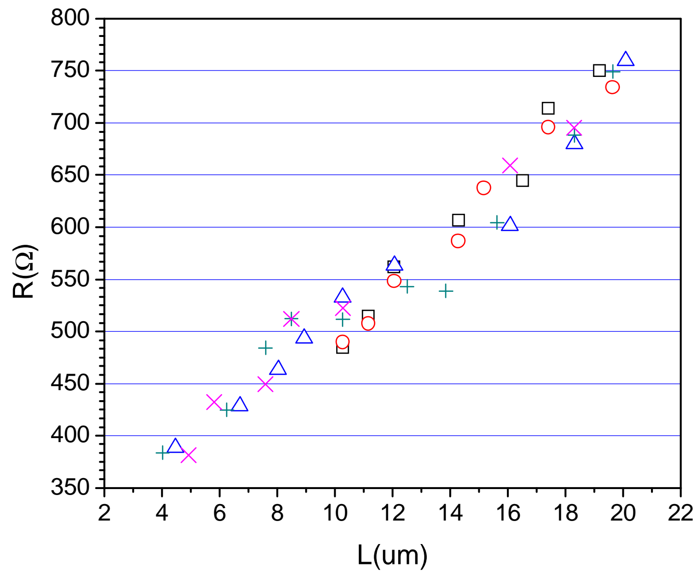

Fig. 5.26: TLM data from the sample with implant concentration 2×10^{19} cm^{-3}.

Strip No.	LTLM			Van Der Pauw
	$R_c\,(\Omega)$	R_{sh} (Ω/□)	$r_c\,(\Omega \cdot cm^2)$	R_{sh} (Ω/□)
1	98	5744	6.74×10^{-4}	Pattern 1: R_{sh}=3136 Pattern 2: R_{sh}=2841 Pattern 3: R_{sh}=3698
2	106	5416	8.38×10^{-4}	
Avg.	102	5580	7.56×10^{-4}	3225
d	4	164	8.2×10^{-5}	355

Table: 5.13: Summary of specific contact resistance and sheet resistance measurement for Al-implanted (0001) 4H-SiC with implant concentration 2×10^{19} cm^{-3}.

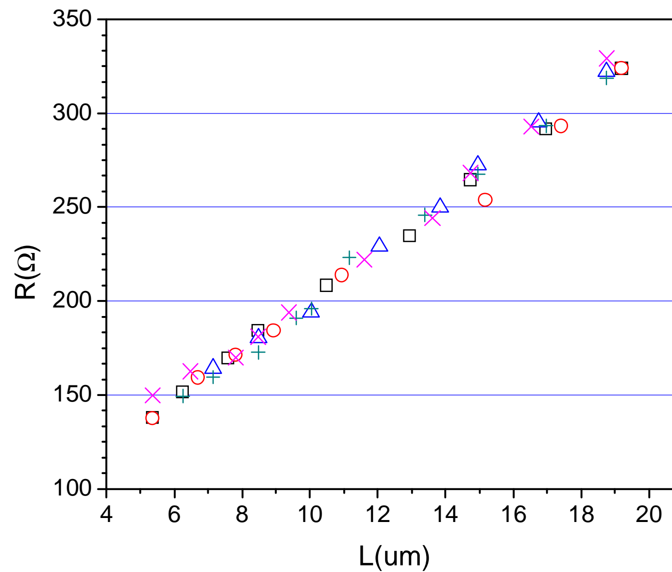

Fig. 5.27: TLM data from one of the two prepared samples with Al implant concentration 8×10^{19} cm^{-3}.

Strip No.	LTLM			Van Der Pauw
	$R_c\,(\Omega)$	$R_{sh}\,(\Omega/\square)$	$r_c\,(\Omega \cdot cm^2)$	$R_{sh}\,(\Omega/\square)$
1	34.4	2639	1.80×10^{-4}	Pattern 1: R_{sh}=2010 Pattern 2: R_{sh}=1819 Pattern 3: R_{sh}=2120 Pattern 4: R_{sh}=1640
2	35.1	2570	1.91×10^{-4}	
3	30.4	2786	1.32×10^{-4}	
4	30.4	2757	1.34×10^{-4}	
5	35.1	2683	1.83×10^{-4}	
6	27.7	2656	$1.15\text{x}10^{-4}$	
7	28.3	2508	$1.28\ \text{x}10^{-4}$	
8	7.27	2909	$7.27\text{x}10^{-6}$	
9	7.09	2837	$7.09\ \text{x}10^{-6}$	
10	7.92	3168	$7.92\ \text{x}10^{-6}$	
Avg.	24.4	2751	1.08×10^{-4}	1897
d	12.0	190	7.4×10^{-5}	212

Table 5.14: Summary of specific contact resistance and sheet resistance measurement for Al-implanted (0001) 4H-SiC with implant concentration 8×10^{19} cm^{-3}.

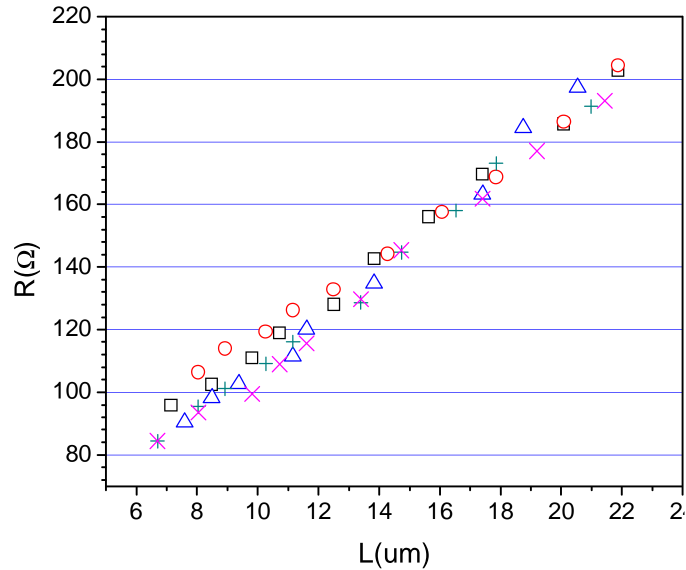

Fig. 5.28: TLM data from one of the two prepared samples with implant concentration 2×10^{20} cm^{-3}.

Strip No.	LTLM			Van Der Pauw
	$R_c\,(\Omega)$	$R_{sh}\,(\Omega/\square)$	$r_c\,(\Omega \cdot cm^2)$	$R_{sh}\,(\Omega/\square)$
1	14.5	2612	3.22×10^{-5}	Pattern 1: R_{sh}=1208 Pattern 2: R_{sh}=1345 Pattern 3: R_{sh}=1682 Pattern 4: R_{sh}=1231 Pattern 5: R_{sh}=1182 Pattern 6: R_{sh}=1125
2	10.3	2475	1.71×10^{-5}	
3	25.42	2236	1.16×10^{-4}	
4	23.42	2019	1.09×10^{-4}	
5	20.1	1469	1.10×10^{-4}	
6	24.8	1366	1.80×10^{-4}	
7	12.3	1653	3.67×10^{-5}	
8	16.1	1525	6.78×10^{-5}	
9	14.8	1523	5.72×10^{-5}	
Avg.	18.4	1875	8.07×10^{-5}	1296
d	5.6	470	5.2×10^{-5}	203

Table: 5.15: Summary of specific contact resistance and sheet resistance measurement for Al-implanted (0001) 4H-SiC with implant concentration 2×10^{20} cm^{-3}.

Table 5.16 shows the summery of TLM and Van der Pauw results for the full set of implant concentrations. The sheet resistance from TLM is in a good agreement with that from Van der Pauw technique for each implant concentration except 2×10^{18} cm^{-3}. The specific contact resistance is in the range 10^{-4} ~10^{-5} Ω.cm^2, which is 10 times larger than that for N-implanted samples, suggesting that it is hard to form a good contact for Al-implanted samples with low implant concentration. In Fig. 5.29, the diamond symbols are the extracted specific contact resistances from p-type epitaxial 6H-SiC [30]. The solid line is a theoretical calculation assuming a single parabolic energy barrier with a barrier height of 0.37eV [30]. The triangle symbols are the measured specific contact resistances

from Al-implanted samples. The experimental data points are far from the theoretical curve for implant concentrations 8×10^{19} and 2×10^{20} cm^{-3}, as was observed in the last section for N-implanted samples. This is further evidence that less implanted atoms are activated at high implantation.

Implant Conc. (cm^{-3})	Strip No.	$r_c^{avg.} \pm \Delta$ ($\Omega.cm^2$) (TLM)		$R_{sh}^{avg.} \pm \Delta$ ($\Omega/\square$) (TLM)		$R_{sh}^{avg.} \pm \Delta$ ($\Omega/\square$) (Van der Pauw)	
2e18	5	2.44×10^{-3}	$\pm 9.65\times10^{-4}$	25200	± 1420	13083	±963
8e18	5	4.24×10^{-4}	$\pm 1.85\times10^{-4}$	8542	± 342	5430	± 580
2e19	2	7.56×10^{-4}	$\pm 8.2\times10^{-5}$	5580	± 164	3225	± 355
8e19	10	1.08×10^{-4}	$\pm 7.4\times10^{-5}$	2751	± 190	1897	± 212
2e20	9	8.07×10^{-5}	$\pm 5.2\times10^{-5}$	1875	± 470	1296	± 203

Table 5.16: Summary of specific contact resistance and sheet resistance measurement for Al-implanted (0001) 4H-SiC.

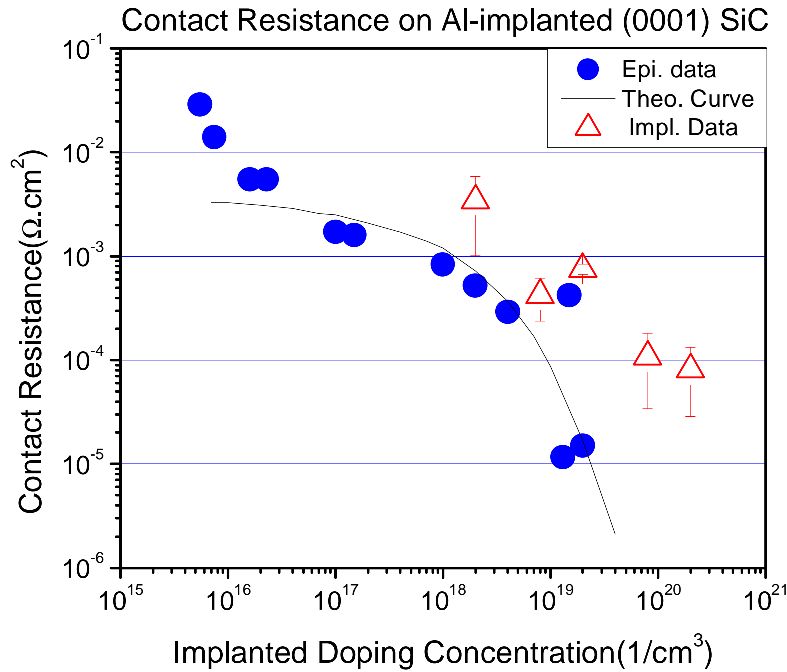

Fig. 5.29: Specific contact resistance vs. implant concentration for Al-implanted 4H-SiC.

5.5 Effect of Activation Temperatures

The sheet resistance of nitrogen, phosphorus, aluminum, and boron implanted SiC as a function of activation temperature has been studied [98]. Herein further study of the effect of activation temperature on specific contact resistance was carried out. Two different implant concentrations 5×10^{18} and 1×10^{20} cm^{-3} were used for both N- and Al-implanted 4H-SiC. N-implanted samples were activated at 1350, 1450, 1550 and 1650 ^{o}C for 30 min with a carbon cap in Ar environment, respectively. Al-implanted samples were activated at 1400, 1500, 1600 and 1700°C for 30 min with a carbon cap in an Ar environment. NiV7% contacts were fabricated to N-implanted samples and annealed at 1100°C /1min/vacuum. Al70Ti30 contacts were used for Al-implanted samples and annealed at 1000°C/1min/vacuum. The specific contact resistances were obtained from TLM analysis.

The specific contact resistance was plotted as a function of activation temperature for each implant type and concentration, as shown in Fig. 5.30. At implant concentration 5×10^{18} cm^{-3}, the specific contact resistance doesn't decrease significantly with the increase of activation temperature for both N- and Al-implantation. However, it does decrease with increasing temperature for the implant concentration 1×10^{20} cm^{-3}. This can be explained as the result of the damage to crystal structure during the implantation process. The higher implant concentration is achieved at a cost of more lattice damage. And a higher activation temperature is needed for damage repair and implant activation for the sample with higher implant concentration.

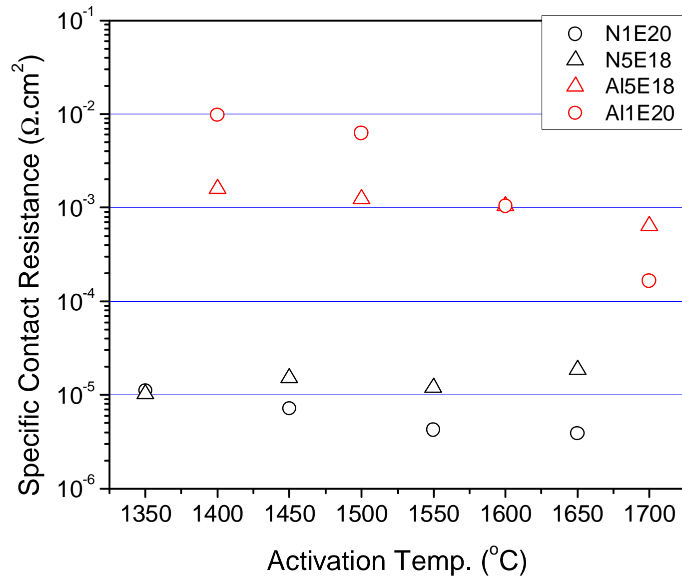

Fig. 5.30: Effect of activation temperature on implanted (0001) 4H-SiC.

5.5.1 TLM Results for N Implant Concentration $5\times10^{18}cm^{-3}$

The TLM data at four activation temperatures for N implant concentration 5×10^{18} cm^{-3} are shown in Fig. 5.31-5.34, and the corresponding TLM and Van der Pauw results are given in Table 5.17-5.20. The sheet resistance from TLM is close to that from Van der Pauw technique for each activation temperature, and TLM data points show a clear linear tendency. The specific contact resistance is stable in the temperature range (1350-1650°C) with the value ~1×10^{-5} $\Omega.cm^2$.

.

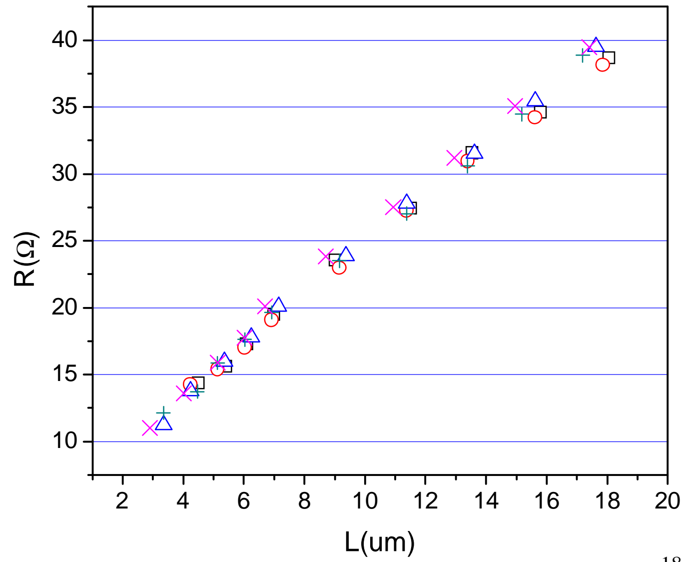

Fig. 5.31: TLM data for N implant concentration $5\times10^{18}cm^{-3}$ activated at $1350^{o}C$/30min/Ar.

Strip No.	TLM			Van Der Pauw
	$R_c\,(\Omega)$	R_{sh} (Ω/□)	$r_c\,(\Omega\cdot cm^2)$	R_{sh} (Ω/□)
1	3.2	361.1	1.16×10^{-5}	Pattern 1: R_{sh}=256 Pattern 2: R_{sh}=227 Pattern 3: R_{sh}=288
2	3.3	357.2	1.21×10^{-5}	
3	2.8	384.9	8.18×10^{-6}	
4	3.0	377.4	9.36×10^{-6}	
5	3.1	388.6	9.63×10^{-6}	
Avg.	3.1	374.8	1.02×10^{-5}	257
d	0.2	14.1	1.6×10^{-6}	30.5

Table: 5.17: Summary of specific contact resistance and sheet resistance measurement for N implant concentration 5×10^{18} cm^{-3} activated at 1350 ^{o}C/30min/Ar.

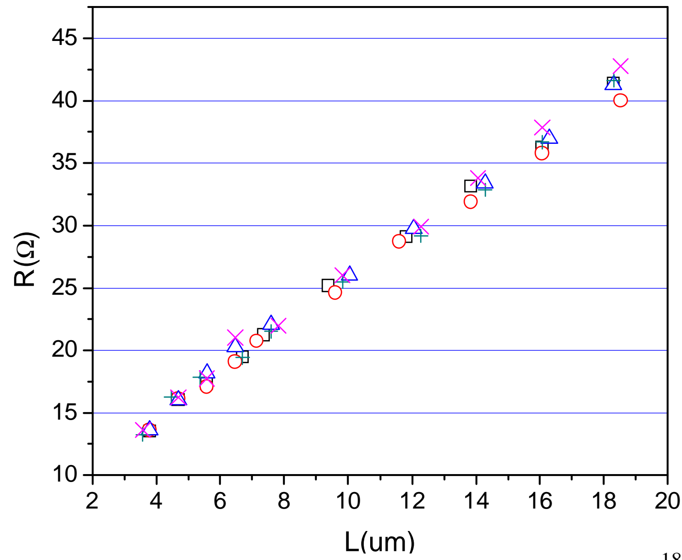

Fig. 5.32: TLM data for N implant concentration $5\times10^{18}cm^{-3}$ activated at $1450^{o}C$/30min/Ar.

Strip No.	TLM			Van Der Pauw
	$R_c\,(\Omega)$	R_{sh} (Ω/□)	$r_c\,(\Omega\cdot cm^2)$	R_{sh} (Ω/□)
1	3.5	373.1	1.34×10^{-5}	Pattern 1: R_{sh}=289 Pattern 2: R_{sh}=241 Pattern 3: R_{sh}=271
2	3.8	352.9	1.63×10^{-5}	
3	3.8	364.4	1.62×10^{-5}	
4	3.7	365.0	1.52×10^{-5}	
5	3.7	379.0	1.43×10^{-5}	
Avg.	3.7	366.9	1.51×10^{-5}	267
d	0.1	9.9	1.2×10^{-6}	24

Table: 5.18: Summary of specific contact resistance and sheet resistance measurement for N implant concentration 5×10^{18} cm^{-3} activated at 1450 ^{o}C/30min/Ar.

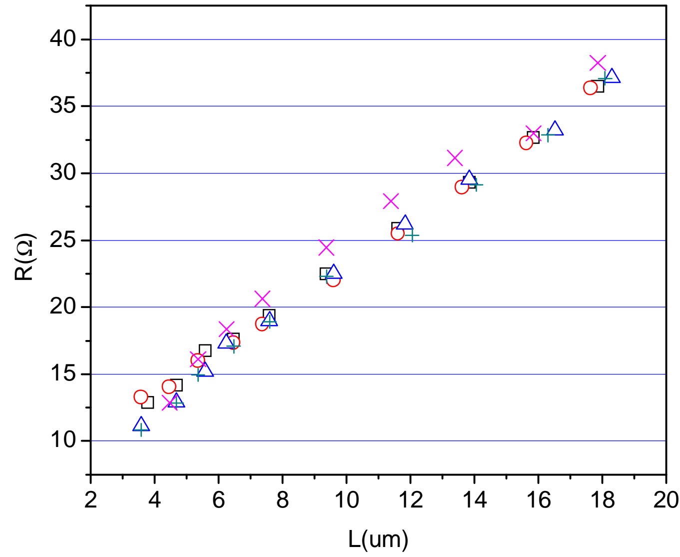

Fig. 5.33: TLM data for N implant concentration $5\times10^{18}cm^{-3}$ activated at $1550^{o}C$/30min/Ar.

Strip No.	TLM			Van Der Pauw
	$R_c\,(\Omega)$	R_{sh} (Ω/□)	$r_c\,(\Omega\cdot cm^2)$	R_{sh} (Ω/□)
1	3.4	328.0	1.45×10^{-5}	Pattern 1: R_{sh}=313 Pattern 2: R_{sh}=236 Pattern 3: R_{sh}=282
2	3.4	326.5	1.45×10^{-5}	
3	2.8	343.9	9.09×10^{-6}	
4	2.7	344.3	8.28×10^{-6}	
5	3.5	351.6	1.36×10^{-5}	
Avg.	3.2	338.9	1.20×10^{-5}	277
d	0.4	11.0	3.1×10^{-6}	39

Table: 5.19: Summary of specific contact resistance and sheet resistance measurement for N implant concentration 5×10^{18} cm^{-3} activated at 1550 ^{o}C/30min/Ar.

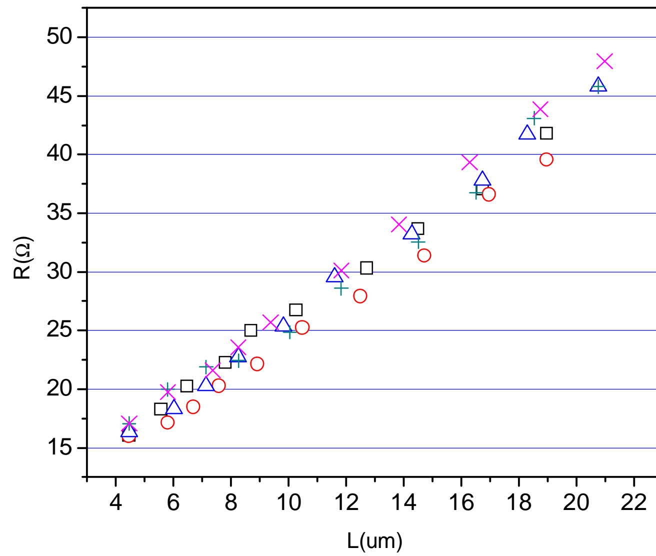

Fig. 5.34: TLM data for N implant concentration 5×10^{18}cm^{-3} activated at 1650°C/30min/Ar.

Strip No.	TLM			Van Der Pauw
	$R_c\,(\Omega)$	R_{sh} (Ω/□)	$r_c\,(\Omega\cdot cm^2)$	R_{sh} (Ω/□)
1	4.3	346.3	2.16×10^{-5}	Pattern 1: R_{sh}=278 Pattern 2: R_{sh}=236 Pattern 3: R_{sh}=261
2	3.8	333.3	1.74×10^{-5}	
3	3.8	367.7	1.54×10^{-5}	
4	4.3	352.2	2.08×10^{-5}	
5	4.1	378.5	1.76×10^{-5}	
Avg.	4.1	355.6	1.86×10^{-5}	258
d	0.3	17.8	2.4×10^{-6}	21

Table: 5.20: Summary of specific contact resistance and sheet resistance measurement for N implant concentration 5×10^{18} cm^{-3} activated at 1650°C/30min/Ar.

5.5.2 TLM Results for N Implant Concentration 1×10^{20} cm^{-3}

The TLM data for four activation temperatures for N implant concentration $1\times10^{20}cm^{-3}$ are shown in Fig. 5.35-5.38, and the corresponding TLM and Van der Pauw results are give in Table 5.21-5.24. The sheet resistance from TLM is close to that from Van der Pauw technique for each activation temperature and TLM data points show a clear linear tendency. The specific contact resistance changes from 10^{-5} to $10^{-6}\Omega.cm^2$ in the temperature range (1350-1650°C), which suggests that higher activation temperature does help the recovery of crystal structure and increase the activation ratio.

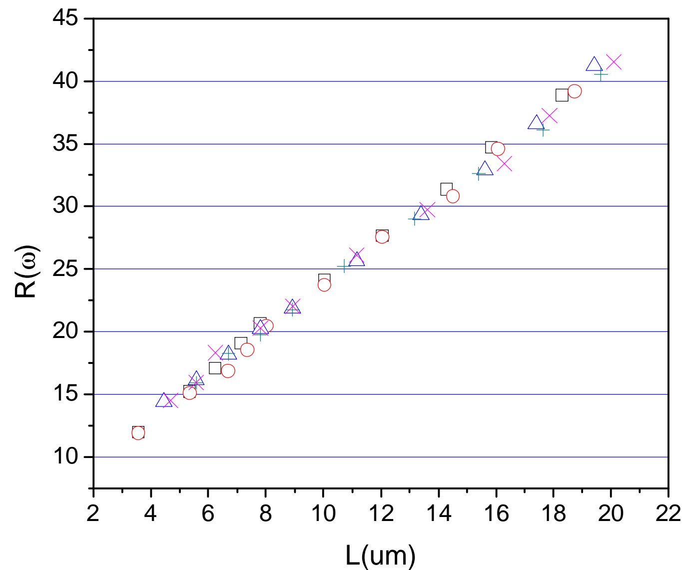

Fig. 5.35: TLM data for N implant concentration $1\times10^{20}cm^{-3}$ activated at 1350°C/30min/Ar.

Strip No.	TLM			Van Der Pauw
	$R_c\,(\Omega)$	R_{sh} (Ω/□)	$r_c\,(\Omega \cdot cm^2)$	R_{sh} (Ω/□)
1	2.9	362.9	9.25×10^{-6}	Pattern 1: R_{sh}=289 Pattern 2: R_{sh}=239 Pattern 3: R_{sh}=283
2	2.7	360.2	8.10×10^{-6}	
3	3.2	349.0	1.16×10^{-5}	
4	3.3	341.2	1.26×10^{-5}	
5	3.5	338.8	1.41×10^{-5}	
Avg.	3.1	350.4	1.11×10^{-5}	270
d	0.3	10.9	2.4×10^{-6}	27

Table: 5.21: Summary of specific contact resistance and sheet resistance measurement for N implant concentration 1×10^{20} cm^{-3} activated at 1350°C/30min/Ar.

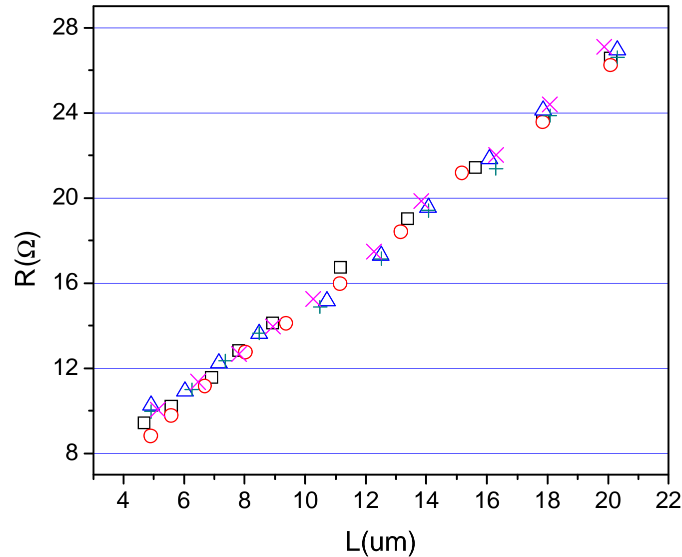

Fig. 5.36: TLM data for N implant concentration 1×10^{20}cm^{-3} activated at 1450°C/30min/Ar.

Strip No.	TLM			Van Der Pauw
	R_c (Ω)	R_{sh} (Ω/□)	$r_c\ (\Omega \cdot cm^2)$	R_{sh} (Ω/□)
1	2.0	222.5	7.54×10^{-6}	Pattern 1: R_{sh}=198 Pattern 2: R_{sh}=160 Pattern 3: R_{sh}=178
2	1.7	227.9	5.11×10^{-6}	
3	2.1	219.1	8.26×10^{-6}	
4	2.1	214.6	8.56×10^{-6}	
5	1.9	228.7	6.35×10^{-6}	
Avg.	2.0	222.6	7.16×10^{-6}	179
d	0.2	5.9	1.4×10^{-6}	19

Table: 5.22: Summary of specific contact resistance and sheet resistance measurement for N implant concentration 1×10^{20} cm^{-3} activated at 1450°C/30min/Ar.

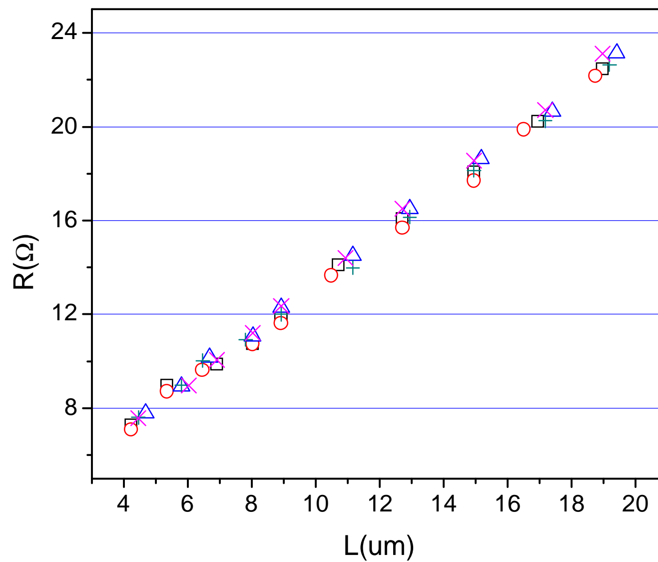

Fig. 5.37: TLM data for N implant concentration 1×10^{20}cm^{-3} activated at 1550°C/30min/Ar.

Strip No.	TLM			Van Der Pauw
	$R_c\,(\Omega)$	$R_{sh}\,(\Omega/\square)$	$r_c\,(\Omega\cdot cm^2)$	$R_{sh}\,(\Omega/\square)$
1	1.5	203.8	4.34×10^{-6}	Pattern 1: $R_{sh}=178$ Pattern 2: $R_{sh}=147$ Pattern 3: $R_{sh}=151$
2	1.4	203.7	3.94×10^{-6}	
3	1.5	205.5	4.48×10^{-6}	
4	1.6	200.4	4.97×10^{-6}	
5	1.4	213.0	3.48×10^{-6}	
Avg.	1.48	205.3	4.24×10^{-6}	159
d	0.08	4.7	5.6×10^{-7}	17

Table: 5.23: Summary of specific contact resistance and sheet resistance measurement for N implant concentration 1×10^{20} cm^{-3} activated at 1550°C/30min/Ar.

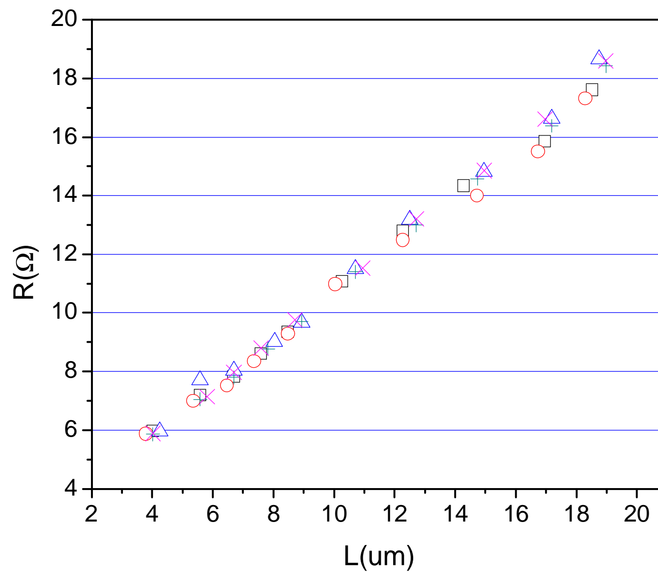

Fig. 5.38: TLM data for N implant concentration 1×10^{20}cm^{-3} activated at 1650°C/30min/Ar.

Strip No.	TLM			Van Der Pauw
	R_c (Ω)	R_{sh} (Ω/□)	r_c $(\Omega \cdot cm^2)$	R_{sh} (Ω/□)
1	1.3	160.3	4.43×10^{-6}	Pattern 1: R_{sh}=141 Pattern 2: R_{sh}=111 Pattern 3: R_{sh}=126
2	1.4	155.9	4.86×10^{-6}	
3	1.2	168.2	3.62×10^{-6}	
4	1.2	166.5	3.34×10^{-6}	
5	1.2	169.4	3.24×10^{-6}	
Avg.	1.26	164.1	3.90×10^{-6}	126
d	0.09	5.8	7.1×10^{-7}	15

Table: 5.24: Summary of specific contact resistance and sheet resistance measurement for N implant concentration 1×10^{20} cm^{-3} activated at 1650°C/30min/Ar.

5.5.3 TLM Results for Al Implant Concentration 5×10^{18}cm^{-3}

The TLM data for four activation temperatures for Al implant concentration 5×10^{18} cm^{-3} are shown in Fig. 5.39-5.42, and the corresponding TLM and Van der Pauw results are given in Table 5.25-5.28. The sheet resistance from TLM is almost twice as that from Van der Pauw technique for all the activation temperatures, which is likely due to the high contact resistance for Al-implanted material. The specific contact resistance is stable over the temperature range (1400-1700°C). The value of specific contact resistance is ~1×10^{-3} Ω.cm^{2}, which is 100 times higher than that for N-implanted samples with the same implant concentration.

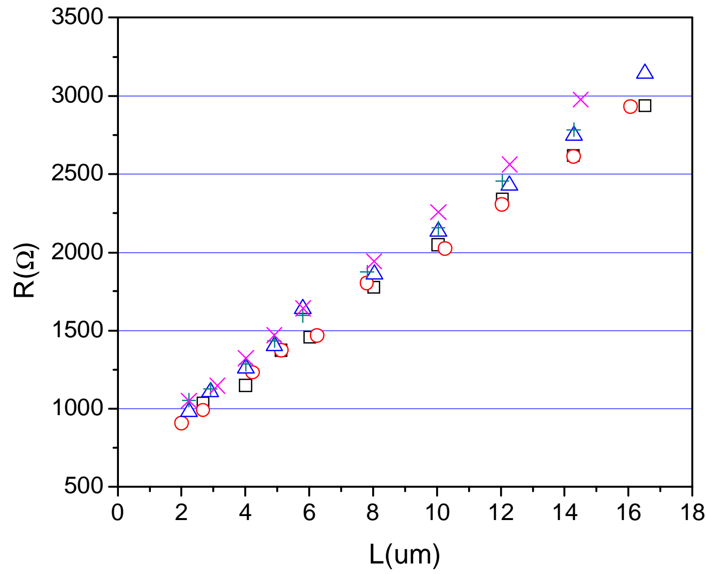

Fig. 5.39: TLM data for Al implant concentration $5\times10^{18}cm^{-3}$ activated at 1400^oC/30min/Ar.

Strip No.	TLM			Van Der Pauw
	$R_c\,(\Omega)$	R_{sh} (Ω/□)	$r_c\,(\Omega\cdot cm^2)$	R_{sh} (Ω/□)
1	316.9	27948	1.44×10^{-3}	Pattern 1: R_{sh}=14487 Pattern 2: R_{sh}=13529 Pattern 3: R_{sh}=13144
2	312.5	28166	1.39×10^{-3}	
3	343.1	29200	1.61×10^{-3}	
4	363.4	28768	1.84×10^{-3}	
5	355.5	30554	1.65×10^{-3}	
Avg.	338	28927	1.59×10^{-3}	13720
d	23	1035	1.8×10^{-4}	692

Table: 5.25: Summary of specific contact resistance and sheet resistance measurement for Al implant concentration 5×10^{18} cm^{-3} activated at 1400^oC/30min/Ar.

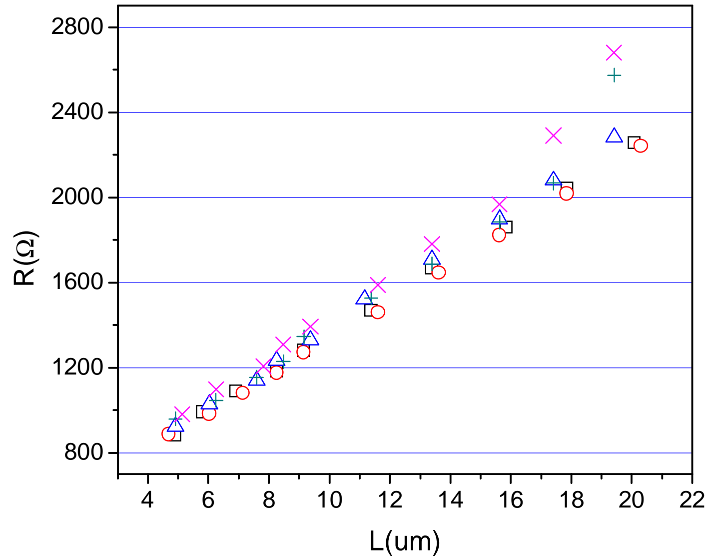

Fig. 5.40: TLM data for Al implant concentration 5×10^{18}cm^{-3} activated at 1500°C/30min/Ar.

Strip No.	TLM			Van Der Pauw
	$R_c\,(\Omega)$	R_{sh} (Ω/□)	$r_c\,(\Omega\cdot cm^2)$	R_{sh} (Ω/□)
1	231.2	17780	1.20×10^{-3}	Pattern 1: R_{sh}=11712 Pattern 2: R_{sh}=10489 Pattern 3: R_{sh}=10026
2	231.3	17421	1.23×10^{-3}	
3	229.3	18657	1.13×10^{-3}	
4	248.5	17895	1.38×10^{-3}	
5	248.4	18930	1.30×10^{-3}	
Avg.	238	18137	1.25×10^{-3}	10742
d	10	632	9.6×10^{-5}	871

Table: 5.26: Summary of specific contact resistance and sheet resistance measurement for Al implant concentration 5×10^{18} cm^{-3} activated at 1500°C/30min/Ar.

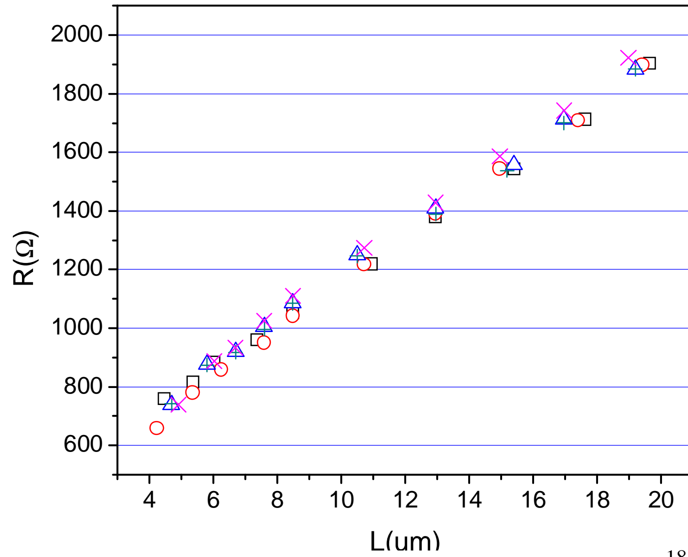

Fig. 5.41: TLM data for Al implant concentration 5×10^{18}cm^{-3} activated at 1600°C/30min/Ar.

Strip No.	TLM			Van Der Pauw
	$R_c\,(\Omega)$	R_{sh} (Ω/□)	$r_c\,(\Omega\cdot cm^2)$	R_{sh} (Ω/□)
1	210.5	14795	1.20×10^{-3}	Pattern 1: R_{sh}=8382 Pattern 2: R_{sh}=9097
2	175.3	15903	7.73×10^{-4}	
3	210.1	15209	1.16×10^{-3}	
4	209.4	15150	1.16×10^{-3}	
5	197.8	16059	9.75×10^{-4}	
Avg.	201	15423	1.05×10^{-3}	8740
d	15	536	1.8×10^{-4}	506

Table: 5.27: Summary of specific contact resistance and sheet resistance measurement for Al implant concentration 5×10^{18} cm^{-3} activated at 1600°C/30min/Ar.

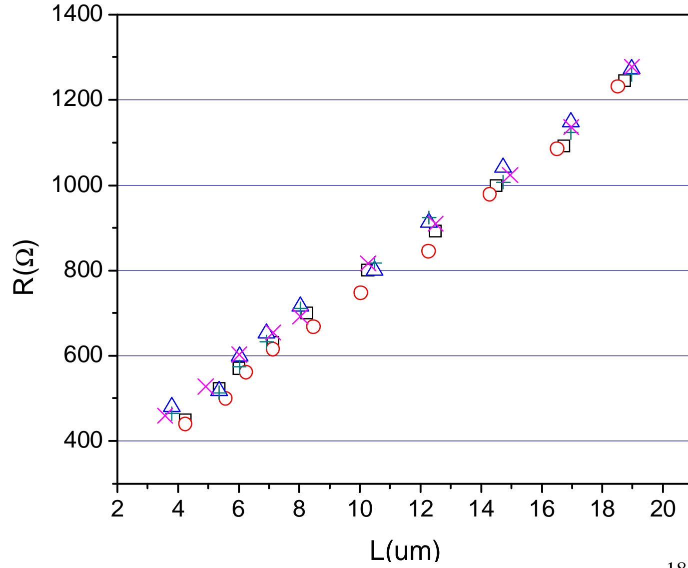

Fig. 5.42: TLM data for Al implant concentration 5×10^{18}cm^{-3} activated at 1700°C/30min/Ar.

<table>
<tr><th rowspan="2">Strip No.</th><th colspan="3">TLM</th><th>Van Der Pauw</th></tr>
<tr><th>$R_c\,(\Omega)$</th><th>R_{sh} (Ω/□)</th><th>$r_c\,(\Omega\cdot cm^2)$</th><th>R_{sh} (Ω/□)</th></tr>
<tr><td>1</td><td>124.9</td><td>10405</td><td>6.00×10^{-4}</td><td rowspan="5">Pattern 1:
R_{sh}=6439
Pattern 2:
R_{sh}=5480</td></tr>
<tr><td>2</td><td>105.8</td><td>10743</td><td>4.17×10^{-4}</td></tr>
<tr><td>3</td><td>137.7</td><td>10396</td><td>7.30×10^{-4}</td></tr>
<tr><td>4</td><td>133.6</td><td>10336</td><td>6.91×10^{-4}</td></tr>
<tr><td>5</td><td>141.3</td><td>10215</td><td>7.82×10^{-4}</td></tr>
<tr><td>*Avg.*</td><td>129</td><td>10419</td><td>6.44×10^{-4}</td><td>5960</td></tr>
<tr><td>***d***</td><td>14</td><td>196</td><td>1.4×10^{-4}</td><td>678</td></tr>
</table>

Table: 5.28: Summary of specific contact resistance and sheet resistance measurement for Al implant concentration 5×10^{18} cm^{-3} activated at 1700°C/30min/Ar.

5.5.4 TLM Results for Al Implant Concentration 1×10^{20} cm^{-3}

TLM data for four activation temperatures for Al implant concentration 1×10^{20}cm^{-3} are shown in Fig. 5.43-5.46, and the corresponding TLM and Van der Pauw results are given in Table 5.29-5.32. The sheet resistance from TLM is about twice that the value as from Van der Pauw technique, which has also been observed for Al implant concentration 5×10^{18} cm^{-3} (section **5.5.3**). The specific contact resistance changes from10^{-3} to 10^{-4} Ω.cm^2 over the temperature range (1400-1700°C), which suggests that higher activation temperature helps the recovery of crystal structure for Al-implanted material.

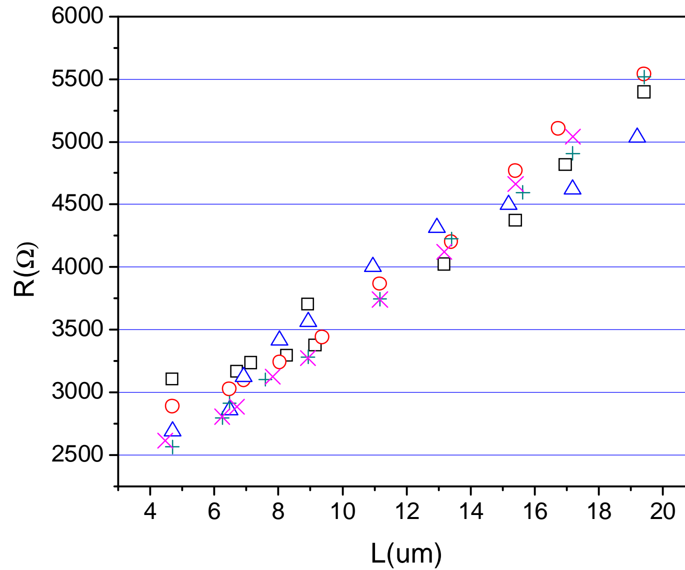

Fig. 5.43: TLM data for Al implant concentration 1×10^{20}cm^{-3} activated at 1400°C/30min/Ar.

Strip No.	TLM			Van Der Pauw
	$R_c\,(\Omega)$	R_{sh} (Ω/□)	$r_c\,(\Omega\cdot cm^2)$	R_{sh} (Ω/□)
1	1067	31228	1.46×10^{-2}	Pattern 1: R_{sh}=15908 Pattern 2: R_{sh}=13240 Pattern 3: R_{sh}=11101
2	890	38290	8.27×10^{-3}	
3	1019	32108	1.29×10^{-2}	
4	798	39208	6.49×10^{-3}	
5	801	39224	6.53×10^{-3}	
Avg.	915	36012	9.76×10^{-3}	13416
d	124	3995	3.8×10^{-3}	2408

Table: 5.29: Summary of specific contact resistance and sheet resistance measurement for Al implant concentration 1×10^{20} cm^{-3} activated at 1400°C/30min/Ar.

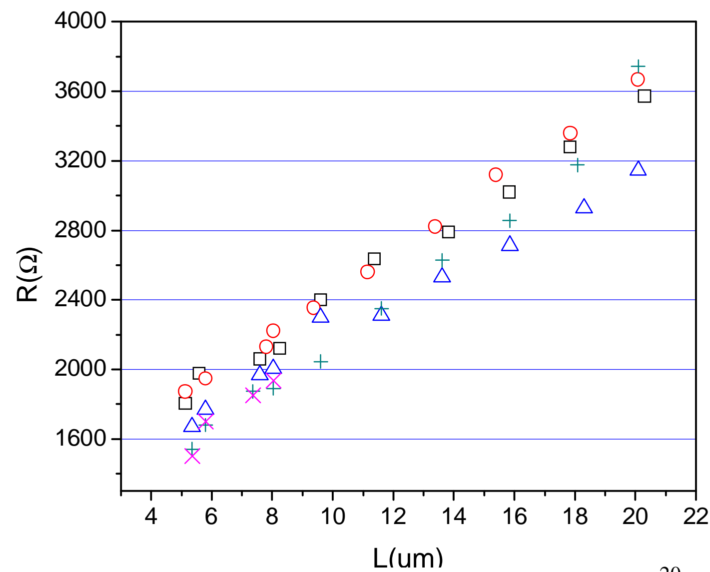

Fig. 5.44: TLM data for Al implant concentration 1×10^{20}cm^{-3} activated at 1500°C/30min/Ar.

Strip No.	TLM			Van Der Pauw
	R_c (Ω)	R_{sh} (Ω/□)	r_c ($\Omega \cdot cm^2$)	R_{sh} (Ω/□)
1	631	22582	7.05×10^{-3}	Pattern 1: R_{sh}=9412 Pattern 2: R_{sh}=9753 Pattern 3: R_{sh}=12317
2	617	24030	6.34×10^{-3}	
3	622	18823	8.21×10^{-3}	
4	456	24844	3.34×10^{-3}	
Avg.	582	22570	6.24×10^{-3}	10494
d	84	2667	2.08×10^{-3}	1588

Table: 5.30: Summary of specific contact resistance and sheet resistance measurement for Al implant concentration 1×10^{20} cm^{-3} activated at 1500°C/30min/Ar.

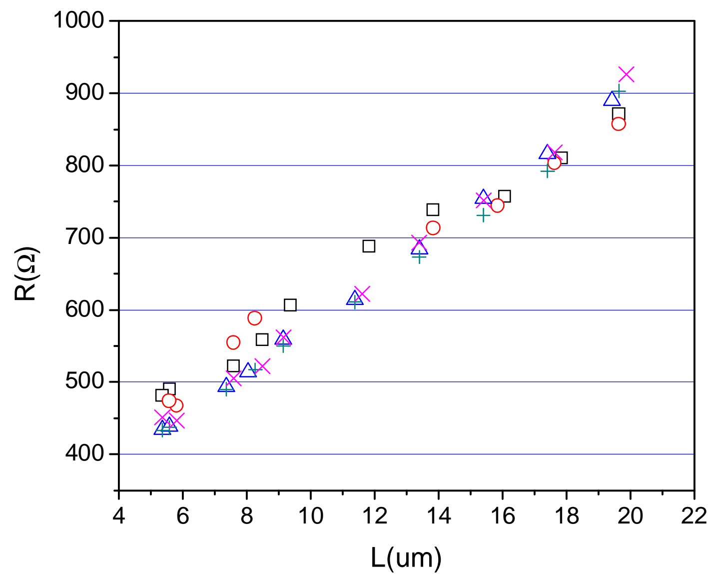

Fig. 5.45: TLM data for Al implant concentration 1×10^{20}cm^{-3} activated at 1600°C/30min/Ar.

Strip No.	TLM			Van Der Pauw
	$R_c\,(\Omega)$	R_{sh} (Ω/□)	$r_c\,(\Omega\cdot cm^2)$	R_{sh} (Ω/□)
1	129.7	6482	1.04×10^{-3}	Pattern 1: R_{sh}=2983 Pattern 2: R_{sh}=2725
2	128.5	6447	1.02×10^{-3}	
3	128.8	6305	1.05×10^{-3}	
Avg.	129	6411	1.04×10^{-3}	2854
d	0.6	94	1.5×10^{-5}	182

Table: 5.31: Summary of specific contact resistance and sheet resistance measurement for Al implant concentration 1×10^{20} cm^{-3} activated at 1600°C/30min/Ar.

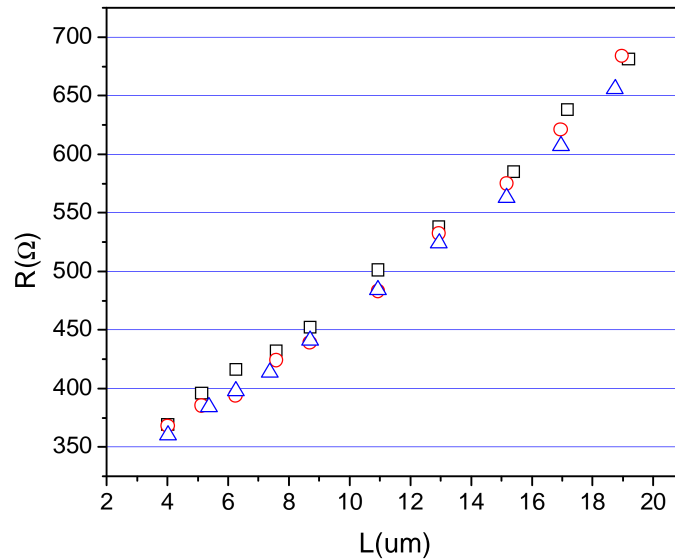

Fig. 5.46: TLM data for Al implant concentration 1×10^{20}cm^{-3} activated at 1700°C/30min/Ar.

Strip No.	Small Gap			Van Der Pauw
	$R_c\,(\Omega)$	R_{sh} (Ω/□)	$r_c\,(\Omega \cdot cm^2)$	R_{sh} (Ω/□)
1	38.3	4169.8	1.41×10^{-4}	Pattern 1: R_{sh} =1789 Pattern 2: R_{sh} =1618 Pattern 3: R_{sh} =2061
2	37.3	4176.8	1.33×10^{-4}	
3	43.2	3859.2	1.94×10^{-4}	
4	42.1	3819.8	1.86×10^{-4}	
5	42.3	3993	1.79×10^{-4}	
Avg.	40.6	4003.7	1.66×10^{-4}	1823
d	2.6	167.6	2.77×10^{-5}	223

Table: 5.32: Summary of specific contact resistance and sheet resistance measurement for Al implant concentration 1×10^{20} cm^{-3} activated at 1700°C/30min/Ar.

5.6 Hall Measurement Results

The samples for the first round of Hall measurements were fabricated on epitaxial material with an implanted layer 550 nm thick. Due to the nonsymmetrical contact resistance of the ohmic contacts at four corners, especially for Al-implanted samples, only one reliable result was obtained for the nitrogen implant concentration 1×10^{20} cm^{-3} as shown in Fig. The Hall measurements were taken in a temperature range 300 to 780K. As can be seen, the maximum measured carrier density was 2.2×10^{19} cm^{-3}, and the corresponding activation ratio is ~23% as shown in Fig. 5.47.

Hall samples were re-fabricated for the second round of Hall measurements. N-implantation were performed on semi-insulating 4H-SiC with implant concentrations 1×10^{18}, 4×10^{18}, 1×10^{19}, 4×10^{19} and 1×10^{20} cm^{-3}. The contact areas were heavily implanted (1×10^{20} cm^{-3}) for all the Hall samples. The activation ratio (Hall carrier

concentration/Implant concentration × 100) for the full set of implant concentrations is shown in Fig. 5.48. It should be noted that the Hall result is compatible with that of the original measurement for N-implant concentration 1×10^{20} cm^{-3}.

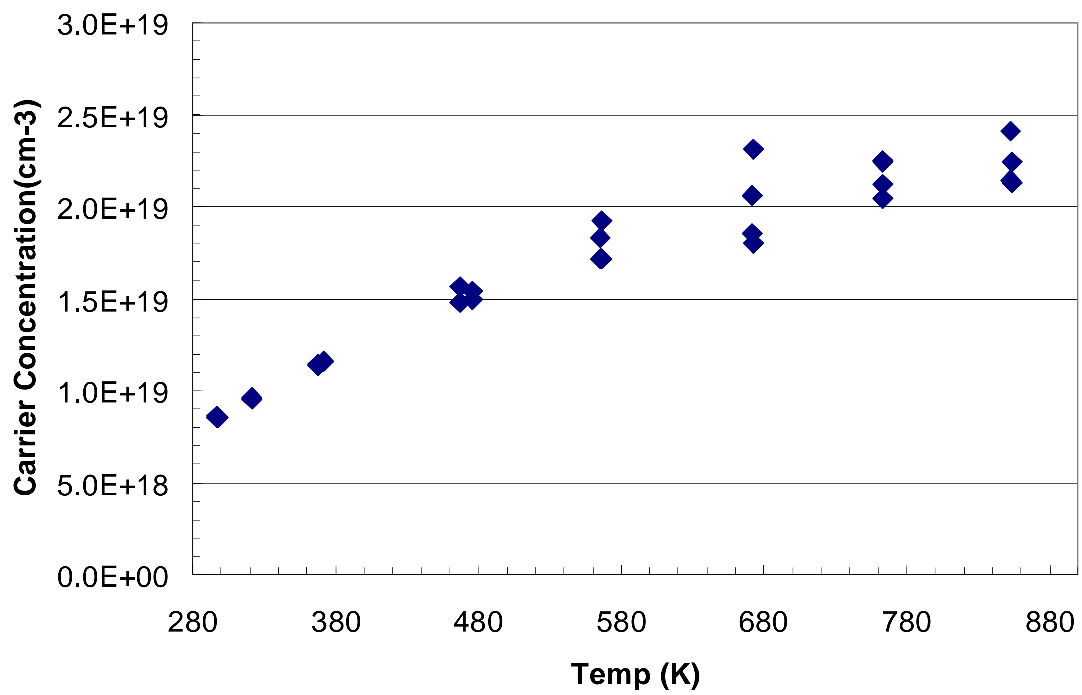

Fig. 5.47: Hall results for N-implant concentration 1×10^{20} cm^{-3} (epitaxial material).

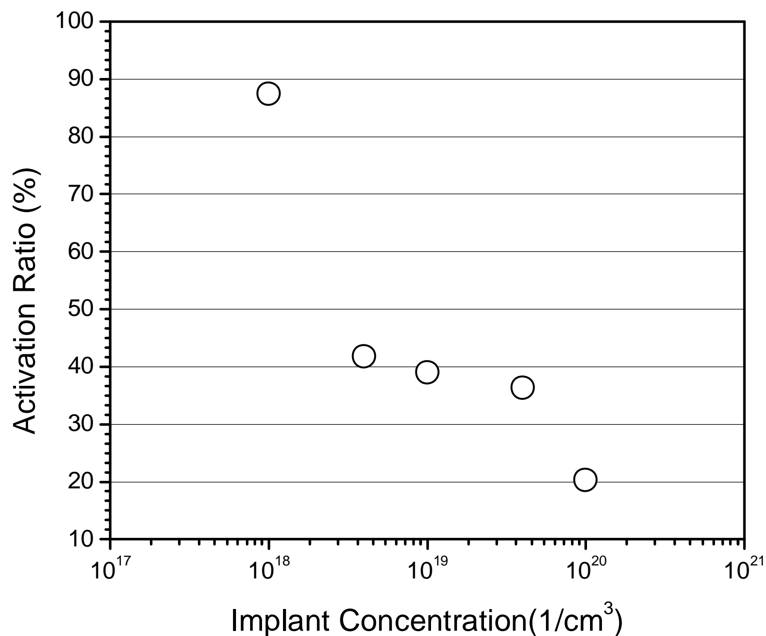

Fig. 5.48: The activation ratio for N-implantation samples based on Hall carrier concentration measured at RT (semi-insulating material).

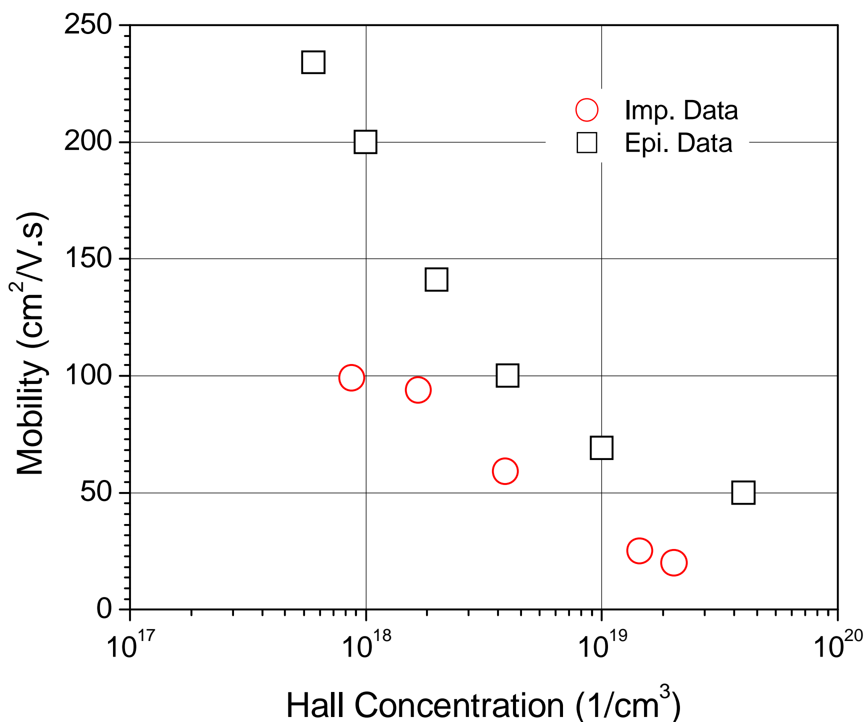

Fig. 5.49: Hall mobility as a function of Hall carrier concentration. Circles - data for implanted samples. Squares - data for epitaxial samples [99]. The implanted samples were activated at 1550°C/30min/Ar. (semi-insulating material).

Fig. 5.49 shows the Hall mobility for both epitaxial and implanted materials. The damage to the crystal structure increases for higher implant concentration. The high temperature activation anneal recovers the damage to the crystalline and activates the implanted atoms. If the residual damage was the main mechanism for lowering the carrier mobility, we should expect a larger offset between epitaxial and implanted data at higher implant concentration. Whereas, our mobility values are lower than the epitaxial values, and are kind of parallel to the epitaxial data. A possible explanation for this is the following: The activation anneal can recover all the damage to the crystalline due to the implantation process [100]. Meanwhile, some other kind of defects are created by the activation anneal itself to the implanted samples. Due to the same activation anneal condition, the same amount of defects are expected for all the samples with different implant concentrations, which brings down the mobility values for implanted material and leads to a parallel trend to the epitaxial data points.

In Fig. 5.50, the open diamonds are the experimental data plotted as a function of Hall concentration. The two data points at implant concentrations 4×10^{19} and 1×10^{20} cm^{-3} are now in better agreement with the theoretical curve. However, the contact resistances for the two lowest concentrations are significantly lower than those predicted by theory.

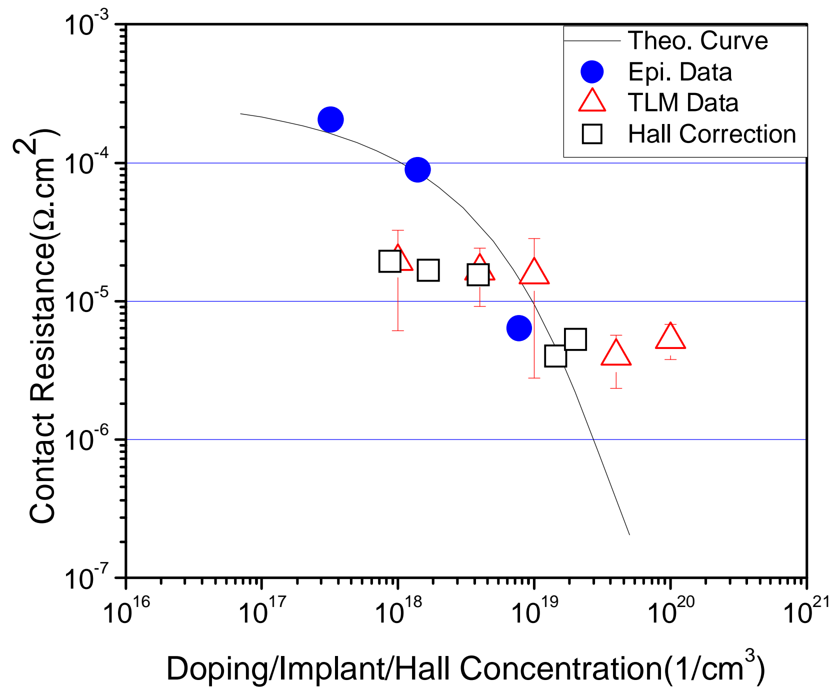

Fig. 5.50: Specific contact resistance for N-implanted (0001) 4H-SiC. The solid circles are the published data for Ni contacts to epitaxial 6H-SiC, and the solid line is a numerical calculation for the epi data. Triangles with error bars are the data for implanted 4H samples plotted as a function of implant concentration, and the squares are the same data plotted as a function of Hall carrier concentration.

CHAPTER 6

SUMMARY, CONCOLUSIONS AND SUGGESTIONS FOR FUTURE WORK

Summary

In this study, AFM results show that the surface roughness of virgin samples is about 0.4 nm and that of the implanted samples is in the range 0.3-0.8 nm for both N and Al implanted samples with the highest implant concentration 2×10^{20} cm^{-3}.

Contact anneal was optimized for both NiV7% and Ni70Cr30 contacts at 1000°C in vacuum. The resulted specific contact resistance become stable after 3 min anneal for NiV7% contact, and reaches ~10^{-4} Ω.cm^{2} for implant concentration 1×10^{19} cm^{-3}; whereas, TLM analysis couldn't be performed for the Ni70Cr30 contact until it was annealed for 6 min, after which the specific contact resistance was ~10^{-5} Ω.cm^{2} for implant concentration 1×10^{18} cm^{-3}.

NiV7% contacts to the full set of N-implanted samples were annealed at 1000°C/2min/vacuum and 1100°C/1min/vacuum, respectively. The extracted specific contact resistance at 1100°C/1min/vacuum was plotted as a function of implant concentrations 1×10^{18}, 4×10^{18}, 1×10^{19}, 4×10^{19} and 1×10^{20} cm^{-3}. Al70Ti30 contacts to Al implanted samples were annealed at 1000°C/1min/vacuum, and the extracted specific contact resistance was also plotted as a function of implant concentrations 2×10^{18}, 8×10^{18}, 2×10^{19}, 8×10^{19} and 2×10^{20} cm^{-3}.

In addition, TLM data for samples activated at different temperatures are presented. The specific contact resistance was plotted as a function activation temperature for implant concentration 5×10^{18} and 1×10^{20} cm^{-3} for both N and Al implanted samples.

Hall measurements were successfully performed for the full set of N-implanted samples at RT with implant concentrations 1×10^{18}, 4×10^{18}, 1×10^{19}, 4×10^{19} and 1×10^{20} cm^{-3}. The activation ratio and the corresponding Hall mobility of N-implanted samples are given. The specific contact resistance as a function of implant/Hall concentrations is also presented.

Conclusions

In many cases, contacts are made to implanted regions due to the difficulty of doping SiC by diffusion. In this work, linear transmission line measurements were performed to investigate the specific contact resistance for both N- and Al-implanted samples. Carbon caps were used for all samples during the post-implant thermal activation annealing process. The N- and Al-implanted samples were activated at 1550°C/30min/Ar and 1650°C/30min/Ar, respectively.

The surface roughness is a very important factor which can affect the electronic properties of SiC devices. For instance, the channel mobility of carriers in MOSFET is closely related to semiconductor surface roughness. Therefore, AFM was taken on the samples before and after implantation. The AFM results show that the surface roughness of the implanted samples is similar to that of virgin samples (~0.4 nm) in a range of 0.3 nm-0.8 nm for both types. As a conclusion, the damage to the sample surface from implantation is small.

The contact anneal optimization was performed for both NiV7% and Ni80%Cr20% contacts to N-implanted samples at 1000°C in vacuum. For NiV7% contacts, the resulted specific contact resistance become stable after 3 min anneal, and reaches ~10^{-4} Ω.cm^2 for implant concentration 1×10^{19} cm^{-3}; whereas, TLM analysis couldn't be performed for Ni70%Cr30% contact until it was annealed for 6 min and the resulted specific contact resistance is ~10^{-5} Ω.cm^2 for implant concentration 1×10^{18} cm^{-3}. This suggests that Ni70%Cr30% is more suitable to make ohmic contact at low implant concentration (<1×10^{19} cm^{-3}) at 1000°C.

The higher anneal temperature and longer anneal time can induce more damage to the real devices. For example, high temperature can degrade the gate oxide quality of MOSFET, which causes the failure of device operation. Therefore, NiV7% contacts were initially annealed at 1000°C for 2 min to the full set of N-implanted samples. The obtained specific contact resistance is in the regime of 10^{-4} Ω.cm^2 for implant concentration larger than 1×10^{19} cm^{-3}.

In order to investigate the relationships between specific contact resistance and implanted doping concentration, NiV7% contacts to N-implanted samples were annealed at 1100°C/1min/vacuum for implant concentrations 1×10^{18}, 4×10^{18}, 1×10^{19}, 4×10^{19} and 1×10^{20} cm^{-3}, and Al70%Ti30% contacts to Al-implanted samples were annealed at 1100°C/1min/vacuum for implant concentrations 2×10^{18}, 8×10^{18}, 2×10^{19}, 8×10^{19} and 2×10^{20} cm^{-3}. The measured specific contact resistances are as low as 10^{-6} and 10^{-5} Ω.cm^2 for N- and Al-implanted samples, respectively. Compared with that to epitaxial material, the specific contact resistance is higher than predicted for epitaxial material at high implant concentrations (> 4×10^{19} cm^{-3}) in both cases. This is probably due to the damage

to the crystal structure from high dose implantation, which might decrease the activation ratio of the implanted ions. Therefore, a higher activation temperature might be needed to help the recovery of the damaged crystal structure.

Further study on the effect of activation temperature to specific contact resistance was also carried out in this research. Two different implant concentrations 5×10^{18} and 1×10^{20} cm^{-3} were achieved for both N- and Al-implanted samples. N-implanted samples were activated at 1350, 1450, 1550 and 1650°C for 30 min with carbon cap in an Ar ambient, respectively. Al-implanted samples were activated at 1400, 1500, 1600 and 1700°C for 30 min with carbon cap in an Ar ambient. NiV7% contacts were fabricated to N-implanted samples and annealed at 1100°C /1min/vacuum. Al70%Ti30% contacts were used for Al-implanted samples and annealed at 1000°C/1min/vacuum. The specific contact resistances were obtained from TLM analysis. At implant concentration 5×10^{18} cm^{-3}, the specific contact resistance doesn't decrease significantly with the increase of activation temperature for both N- and Al-implantation. However, it does drop down as the increase of temperature at implant concentration 1×10^{20} cm^{-3}. This is a further indication of damage to crystal structure during the implantation process. Therefore, higher activation temperature is needed for the samples with higher implant concentration.

The post-implant activation anneal brings the implanted nitrogen atoms to carbon sublattice sites in the crystal structure, where the atoms become electrically active donors [101]. Since only a portion of the implanted atoms can be activated, it is important to know the free carrier concentration for a given implant concentration. Therefore, Hall measurements were performed to the full set of N-implanted samples with implant concentration 1×10^{18}, 4×10^{18}, 1×10^{19}, 4×10^{19} and 1×10^{20} cm^{-3}, which were activated at

1550^oC/30min/Ar. The results show the activation ratio drops down from ~90% to ~20% as the implant concentration increases from 1×10^{18} to 1×10^{20} cm^{-3}. Correspondingly, Hall mobility decreases to 20 $cm^2/V{\cdot}S$ from nearly 100 cm^2/V-S. The measured Hall mobility from implanted samples is lower than, and kind of parallel to the epitaxial data. This might suggest that some kind of defects are created due to the high temperature activation anneal itself, which has the same amount to all the samples.

The specific contact resistance as a function of Hall concentration was plotted for N-implanted samples in Fig. 5.50. At implant concentrations 4×10^{19} and 1×10^{20} cm^{-3}, the measured data points now in a good agreement with the theoretical values. However, the contact resistances for the two lowest concentrations (1×10^{18} and 4×10^{18} cm^{-3}) are significantly lower than those predicted by theory. This is due to the effects of implantation on the ohmic contact barrier height. It is less noticeable at high implant concentrations where carrier tunneling through the barrier is the primary transport mechanism. At lower implant concentrations, reduced barrier height leads to better contact performance than predicted by simple theoretical calculations.

Future Work

Hall measurements should also be extended to Al-implanted samples. The dopant energy level of Al (~190 meV) is much higher than that of nitrogen (~60 meV), so that, in order to avoid carrier freeze-out high temperature (~800K) will be needed for these measurements. It can be seen in Fig. 4.4, the dimension of contact area is 1/30 of the entire Hall pattern. This small contact area might cause the unsymmetrical contact resistance at the four corners. In order to have smaller contact resistance, especially for

the samples with low doping concentration, the Hall mask will be modified, with much larger contact areas sitting outside the Hall pattern as shown in Fig. 6.1.

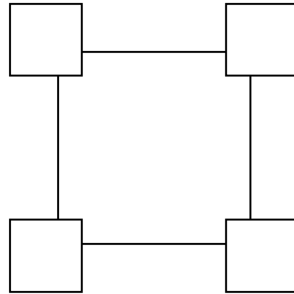

Fig. 6.1: Hall pattern on the new designed Hall mask.

REFERENCES

[1] R. W. Brander and R. P. Sutton, *J. Phys*. **D 2**, 309 (1969)

[2] J. A. Edmond, H. S. Kong, and C. H. Carter, Jr., *Physica* **B 185**, 453 (1993)

[3] H. Amano, M. Kito, K. Hiramatsu and I. Akasaki, *Jpn*, *J. Appl. Phys*. **28**, L2112 (1989)

[4] H. Morkoç, S. Strite, G. B. Gao, M. E. Lin, B. Sverdlov, and M. Burns, *J. Appl. Phys.* **76**, 1363 (1994)

[5] M. Ghezzo, D. M. Brown, E. Downey, J. Kretchmer, W. Hennessy, D. L. Polla and H. Bakhn, *IEEE Electron Device Lett*. **EDG 13**, 639 (1992)

[6] S. Nakamura, Y. Harada and M. Seno, *Appl. Phys. Lett.* **58**, 2021 (1991)

[7] V. V. Zhirnov, G. J. Wojak, W. B. Choi, J. J. Cuomo and J. J. Hren, *J. Vac. Sci. Technol.* **15** (3), 1733 (1997)

[8] G. L. Harris (ed.), EMIS Data Reviews Series, **No 13**, (Short Run Press, Exeter, England, 1995)

[9] J. W. Palmour, H. S. Kong, and R. F. Davis, *Appl. Phys. Lett*. **51**, 2028 (1987)

[10] J. W. Palmour, H. S. Kong, and R. F. Davis, *J. Appl. Phys*. **64**, 2168 (1988)

[11] R. W. Brander and R. P. Sutton, *J. Phys*. **D 2**, 309 (1969)

[12] L. Hoffman, G. Ziegler, D. Theis, and C. Weyrich, *J. Appl. Phys*. **53**, 6962 (1982);

[13] J. A. Edmond, H. S. Kong and C. H. Carter, Jr., *Physica* **B 185**, 453 (1993)

[14] J. W. Hong, N. E Shin, T. S. Jen, S. L. Ning and C. Y. Chang, *IEEE Electron Device*

Lett, **EDL-13**, 375 (1992)

[15] J. R. Williams and R. W. Johnson, *Contact Metallization and Packaging Technolgy Development for SiC Bipolar Junction Transistors*, *PiN Diodes and Schottky Diodes Designed for Long-term Operation at 350^oC* (Proposal submitted to Wright-Patterson Air Force Base, AFRL, 2001)

[16] W. F. Knippenberg, *Philips Research Reports*, **18**, No. 3, 161-274, (1963)

[17] http://www.ifm.liu.se/matephys/new_page/research/sic/Chapter2.html

[18] J. A. Powell, D. J. Larkin, L. G. Matus, W. J. Choyke, J. L. Bradshaw, L. Henderson, M. Yoganathan, J. Yang and P. Pirouz, *Appl. Phys. Lett*. **56** (14), 1353, (1990)

[19] J. A. Powell, J. B. Petit, J. H. Edgar, I. G. Jenkins, L. G. Matus, W. J. Choyke, L. Clemen, M. Yoganathan, J. W. Yang and P. Pirouz, *Appl. Phys. Lett*. **59** (2), 183 (1991)

[20] J. A. Powell, J. B. Petit, J. H. Edgar, I.G. Jenkins, L. G. Matus, J. Yang, P. Pirouz, W. Choyke, L. Clemen and M. Yoganathan, *Appl. Phys. Lett.* **59** (3), 333 (1991)

[21] D. J. Larkin, P. G. Neudeck, J. A. Powell and L. G. Matus, "*5th Int. Conf. on SiC and related Matls*" (Washington, DC, USA, 1993); *Inst. Phys. Conf. Ser*. **No 137**, 51 (1994)

[22] V. I. Lcvin, Y. M. 'Ihirov, M. G. Travazhdyan, F. Tsvetkov, and M. A. Chernov, *Sov. Phys. Izv*. **14**, 830 (1978)

[23] Y. M. Tairov and R. Psverkov, *J. Cryst. Growth* **52**, 146 (1981)

[24] M. Ikeda, T. Hayakawa, Z. Yamagiva, H. Matsunami and T. Tanaka, *J. Appl. Phys.* **50**, 8215 (1979)

[25] W. Muench and W. Kurzinger, *Solid-State Electron*. **21**, 1129 (1978)

[26] V. A. Dmitriev, P. A. Ivanov, I. Korkin, Y. Morozenko, I. Popov, T. A. Sidorova, A. M. Strslchuk and E. Chelnokov, *Sov. Phys. Technol. Lett.* **11**, 98 (1985)

[27] T. Uemoto, Jpn, *J. Appl. Phys.* **34,** L7 (1995)

[28] J. Crofton, P. G. McMullin, J. R. Williams and M. J. Bozack, *J. Appl. Phys.* 77 **(*3*)** 1317 (1995)

[29] S. Liu, K. Reinhardt, J. Scofield and C. Severt, Workshop on High Temperature Power Electronics for Vehicles (1995)

[30] J. Crofton, L. M. Porter and J. R. Williams, *Phys. Stat. Sol.* (b) **202**, 581 (1997)

[31] T. Nakata, K. koga, Y. Matsushita, Y. Ueda and T. Niina, *Amorphous and Crystalline SiC II* (Springer Verlag, Berlin, **26**, 1989)

[32] A. Suzuki, Y. Fujii, H. Saito, Y. Tajima and K. Furukawa, *J. Cryst. Growth* **115**, 623 (1991)

[33] J. Crofton, L. Beyer, J. R. Williams, E. D. Luckowski, S. E. Mohney and J. W. DeLucca, *Solid-State Electron.* **41** (11), 1725 (1997)

[34] N. Braslau, *J. Vac. Sci. Technol.* **19,** 803 (1981)

[35] J. Croton, S. E. Mohney, J. R. Williams and T. Isaacs-Smith, *Solid-State Electron.* **46,** 109 (2002)

[36] M. Ghezzo, D. M. B rown, E. Downey, J. Kretchmer, W. Hennessy, D. L. Polla and H. Bakhn I, *IEEE Electron. Device Lett.* **EDL-13**, 639 (1992)

[37] M. Bhatnagar, P. McLarty, and B. J. Baliga, *IEEE Electron. Device Lett.* **EDL-13**, 501 (1992)

[38] P. G. Neudeck, D. J. Larkin, J. E. Starr, J. A. Powell, C. S. Zalupo, and L. G. Matus, *IEEE Electron. Device Lett.* **EDL-14**, 136 (1993)

[39] R. F. Davis, G. Kelner, M. Shur, J. W. Palmour, and J. A. Edmond, *Proc. IEEE* **79**, 677 (1991)

[40] R. W. Brander and R. P. Sutton, *J. Phys.* **D 2**, 309 (1969)

[42] W. Muench, P. Hoeck, and E. Pettenpaul, *Tech. IEEE Digest IEDM*, 337 (1977)

[43] J. W. Palmour, J. A. Edmond, H. S. Kong, and C. H. Carter, Jr., *Physica **B*** **185**,461 (1993)

[44] F. Yan, J. H. Zhao and G. H. Olsen, *Solid-State Electron.*, **44** (2) 341 (2000)

[45] D.M. Brown, E.T. Downey, M. Ghezzo, J.W. Kretchmer, R.J. Saia, Y.S. Liu *et al.*. *IEEE Trans.* **ED 40** (2), 325 (1993)

[46] J. W. Palmour, J. A. Edmond, H. S. Kong, and C. H. Carter, Jr., *Physica* **B 185**,461 (1993)

[47] http://www.cree.com/products/pdf/CPWR-AN01.A.pdf

[48] http://www.srim.org/#SRIM

[49] A. Tesfaye, *SiC Semiconductor Devices Technology, Modeling, and Simulation*, Dissertation, Universität Wien Fakultät für Elektrotechnik and Informationstechnik (2004)

[50] M. J. Bozack, *Phys. stat. sol. (b)* **202**(1), 549 (1997)

[51] A. Itoh, O. Takemura, T. Kimoto, and H. Matsunami, *Inst. Phys. Conf. Ser.* **142**, 685 (1996)

[52] D. Defives, O. Durand, F. Wyczisk, O. Noblanc, C. Brylinski, and F. Meyer, *Microelectronic Engineering* **55**, **No** 1-4, 369 (2001)

[53] D. Schroeder, *Modeling of Interface Carrier Transport for Device Simulation*, Springer (1994)

[54] C. Fischer, *Bauelementsimulation in einer computergestützten Entwurfsumgebung*, Dissertation, TU Vienna (1994)

[55] R. C. Glass, L. M. Spellman, and R. F. Davis, *Appl. Phys. Lett.* **59**, 2868 (1991)

[56] R. C. Glass, L. M. Spellman, S. Tanaka and R. F. Davis, *J. Vac. Sci. Technol*, **A 10**, 1625 (1992)

[57] J. Crofton, J. M. Ferrero, P. A. Barnes, J. R. Williams, M. J. Bozack, C. C. Tin, C. D. Ellis, J. A. Spitznagel, and P. G. McMullin, *Amorphous Crystalline Silicon Carbide IV*, C. Y. Yang, M. M. Rahman, and G. L. Harris (eds) (Springer-Verlag, Berlin, p.176, 1992)

[58] A. V. Adedeji, *Composite Contact Metallization on SiC for High Temperature Applications in Air*, Dissertation (2005)

[59] G. Kelner, S. Binari, M. Shur, and J. W. Palmmour, *Electronic Lett*. **27**, 1038 (1991)

[60] L. M. Porter and R. F. Davis, *Mat. Sci. and Eng*. **B34**, 83 (1995)

[61] J. Crofton, E. D. Lukowski, J. R. Williams, T. Isaacs-Smith, M. J. Bozack, and R. Siergiej, (in: Silicon Carbide and Related Materials VI-Kyoto 1995) *Inst. of Phys. Conf. Ser.* **142**, 569 (1996)

[62] C. Arnodo, S. Tyc, F. Wyczisk, and C. Brylinski, (in: Silicon Carbide and Related Materials VI- Kyoto 1995) *Inst. of Phys. Conf. Ser.* **142**, 577 (1996)

[63] D. Alok, B. J. Baliga, and P. K. Mclarty, *IEDM* 691 (1993)

[64] M. M. Anikin, M. G. Rastegaeva, A. L. Syrkin, and I. V. Chuiko, *Amorphous Crystalline Silicon Carbide III-Springer-Verlag, Berlin*, F. L. Jarris, M. G. Spencer, and C. Y. Yang (eds) **56** 183-189 (1992)

[65] J. B. Petit, P. G. Neudeck, C. S. Salupo, D. J. Larkin, and J. A. Powell, *Inst. of Phys.*

Conf. Ser. **137**, 679 (1994)

[66] S. Liu, K. Reinhardt, C. Svert and J. Scofield (in: S Silicon Carbide and Related Materials VI- Kyoto 1995) *Inst. of Phys. Conf. Ser.* **142**, 589-592 (1996)

[67] A. K. Chaddha, J. D. Parsons, and G. B. Kruaval, *Appl. Phys. Lett*. **66**, 760 (1995)

[68] N. Lundberg and M. Ostling, *Solid State Electron.* **39**, 1559 (1992)

[69] J. B. Petit, P. G. Neudeck, C. S. Salupo, D. J. Larkin and J. A. Powell, (presented at the Silicon Carbide and Related Materials Conf., Washington DC, 1993) M. G. Spencer, R. P. Devaty, J. A. Edmond, M. A. Khan, R. Kaplan and M. Rahman (eds), *Inst. of Phys. Conf. Ser*. **137**, 679-682 (1993)

[70] J. Crofton, P. A. Barnes, and J. R. Williams, *Appl. Phys. Lett*. **62**, 384-386 (1993)

[71] L. Spiess, O. Nennewitz, and J. Petzoldt, *Inst. of Phys. Conf. Ser.* **142**, 585 (1996)

[72] N. Nordell S. Savage, and A. Schönder, *Inst. of Phys. Conf. Ser.* **142**, 573 (1996)

[73] R. N. Hall, *J. Appl. Phys*. **29**, 914 (1958).

[74] H. Daimon, M. Yamanaka, E. Sakuma, S. Misawa, and S. Yoshida, *J. Appl. Phys*. **25**, L592-L594 (1986)

[75] J. A. Edmond, J. Ryu, J. T. Glass, and R. F. Davis, *J. Electrochem. Soc*. **135**, 359-362 (1988)

[76] A. J. Steckl and J. N. Su, *IEDM* 695-698 (1993).

[77] H. J. Cho, C. S. Hwang, W. Bang, and J. J. Kim, (presented at the Silicon Carbide and Related Materials Conf., Washington DC, 1993)

[78] M. G. Spencer, R. P. Devaty, J. A. Edmond, M. A. Khan, R. Kaplan, and M. Rahman (eds), *Inst. of Phys. Conf. Ser*. **137**, 663 (1993).

[79] J. S. Shor, R. A. Weber, L. G. Provost, D. Goldstein and A. D. Kurtz, *J.*

Electronchem. Soc. **141**, 579-581 (1994)

[80] M. I. Chaudhry, W. B. Berry and M. V. Zeller, *Int. J. Electronics* **71**, 439-444 (1991).

[81] J. S. Chen, A. Bachli, M. A. Nicolet, L. Baud, C. Jaussaud and R. Madar, *Mat. Sci. Eng.* **B29**, 185-189 (1995).

[82] http://en.wikipedia.org/wiki/Atomic_force_microscope

[83] D.K. Schroder, *Semiconductor Material and Device Characterization*, (John Wiley and Sons, Inc.1990).

[84] http://www.ecse.rpi.edu/~schubert/Course-Teaching-modules/A38-Four-point-TLM-measurement.pdf

[85] L. J. van der Pauw, *A method of measuring specific resistivity and Hall effect of discs of arbitrary shape*, *Philips Research Reports* **13**: 1–9 (1958).

[86] http://www.eeel.nist.gov/812/hall.html

[87] L.J. van der Pauw, *A method of measuring the resistivity and Hall coefficient on lamellae of arbitrary shape*, *Philips Technical Review* **20**, 220–224 (1958)

[88] http://en.wikipedia.org/wiki/Image:

[89] S. M. Sze, *Semiconductor Devices: Physics and Technology*. New York: Wiley, pp53 (2001)

[90] G. K. Reeves and H. B. Harrison, *IEEE Electron Device Letters*, **EDL 3** (5) 111 (1982)

[91] http://ecee.colorado.edu/~bart/book/book/chapter3/ch3_5.htm

[92] H. B. Harrison, *Proc. IREE Aust.,* **41,** 95 (1980)

[93] J. Crofton, P. A. Barnes and M. J. Bozack, *Amer. J. Phys*. **69**, 7660 (1991)

[94] J. Crofton and P. A. Barnes, *J. Appl. Phys*. **60**, 499 (1992)

[95] http://www.physics.csbsju.edu/stats/anova.html

[96] http://en.wikipedia.org/wiki/Analysis_of_variance

[97] http://changingminds.org/explanations/research/analysis/t-test_table.htm

[98] http://www.ecn.purdue.edu/WBG/Basic_Measurements/Ion_Implantation/Index. Html

[99] J. Pernot, S. Contreras, J. Camassel, J. L. Robert, W. Zawadzki, E. Neyret, and L. D Cioccio, *Appl. Phys. Lett*. **77**, 4359 (2000)

[100] J. M. Bluet, J. Pernot, J. CAmassel, S. Contreras, J. L. Robert, J. F. Michaud and T. Billon, *J. appl. Phys*. **88,** 1971 (2000)

[101] H. H. Woodbury and G. W. Ludwig, *Phys. Rev*. **124**, 1083 (1961)

APPENDIX

ANOVA: Results for N-implanted Data

The results of a ANOVA statistical test performed at 11:45 on 12-NOV-2009

Source of Variation	Sum of Squares	d.f.	Mean Squares	F
between	2.2475E-09	4	5.6187E-10	7.421
error	3.7858E-09	50	7.5716E-11	
total	6.0333E-09	54		

The probability of this result, assuming the null hypothesis, is 0.000

Group A: Number of items= 12
5.040E-06 6.550E-06 8.640E-06 1.470E-05 1.560E-05 1.630E-05 1.690E-05 1.710E-05 1.790E-05 2.480E-05 3.820E-05 5.130E-05

Mean = 1.942E-05
95% confidence interval for Mean: 1.4374E-05 thru 2.4465E-05
Standard Deviation = 1.330E-05
Hi = 5.130E-05 Low = 5.040E-06
Median = 1.660E-05
Average Absolute Deviation from Median = 8.281E-06

Group B: Number of items= 9
2.880E-06 4.270E-06 5.380E-06 5.810E-06 6.740E-06 2.260E-05 3.020E-05 3.060E-05 3.090E-05

Mean = 1.549E-05
95% confidence interval for Mean: 9.6608E-06 thru 2.1313E-05
Standard Deviation = 1.270E-05
Hi = 3.090E-05 Low = 2.880E-06
Median = 6.740E-06
Average Absolute Deviation from Median = 1.066E-05

Group C: Number of items= 10
7.850E-06 8.740E-06 8.830E-06 1.210E-05 1.250E-05 1.970E-05 2.020E-05 2.340E-05 2.560E-05 2.700E-05

Mean = 1.659E-05
95% confidence interval for Mean: 1.1065E-05 thru 2.2119E-05
Standard Deviation = 7.407E-06
Hi = 2.700E-05 Low = 7.850E-06
Median = 1.610E-05
Average Absolute Deviation from Median = 6.588E-06

Group D: Number of items= 10
2.350E-06 2.400E-06 2.570E-06 3.060E-06 3.130E-06 3.760E-06 4.230E-06 5.760E-06 6.040E-06 6.900E-06

Mean = 4.020E-06
95% confidence interval for Mean: -1.5069E-06 thru 9.5469E-06
Standard Deviation = 1.658E-06
Hi = 6.900E-06 Low = 2.350E-06
Median = 3.445E-06
Average Absolute Deviation from Median = 1.318E-06

Group E: Number of items= 14
3.480E-06 3.570E-06 3.940E-06 4.340E-06 4.390E-06 4.480E-06 4.900E-06 4.970E-06 4.970E-06 5.710E-06 5.930E-06 7.700E-06 7.770E-06 7.870E-06

Mean = 5.287E-06
95% confidence interval for Mean: 6.1602E-07 thru 9.9583E-06
Standard Deviation = 1.519E-06
Hi = 7.870E-06 Low = 3.480E-06
Median = 4.935E-06
Average Absolute Deviation from Median = 1.130E-06